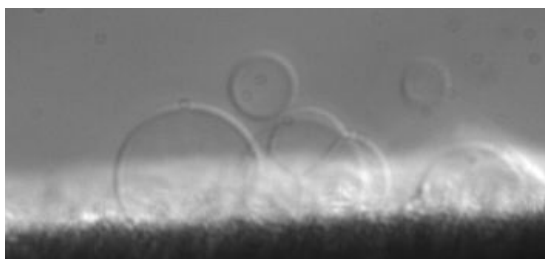


# Amphiphilic Diblock Copolymers for Molecular Recognition



Inauguraldissertation

zur Erlangung der Würde eines Doktors der Philosophie  
vorgelegt der  
Philosophisch-Naturwissenschaftlichen Fakultät  
der Universität Basel

von

**Rainer Nehring**

aus Deutschland  
Basel, 2009



Genehmigt von der Philosophisch-Naturwissenschaftlichen Fakultät

auf Antrag von

Prof. Dr. Wolfgang Meier (Universität Basel)

und

Dr. Jean-Francois Lutz (Universität Potsdam & Fraunhofer IAP Golm)

Basel, den 17. Februar 2009

Prof. Dr. Eberhard Parlow  
(Dekan)

---

**Wir lernten neu zu fühlen, neu zu sehen, denken.  
Die Vision des Chemikers ward zur Expression  
und wollt nach Formen die Gestaltungskraft ihn lenken.  
Dann fand er im Nanoismus seinen Lohn.  
Und das Lebendige, Beweglich-behändige halten wir fest auf beweglichste Art.  
Hier sieht der Verständige, das scheinbar Unbändige,  
das polymerisch geschaffen ward.<sup>1</sup>**

<sup>1</sup>In Anlehnung an Elsa Axmann, 1920

---

## Abstract

In this thesis the design, synthesis and characterization of new, metal-functionalized amphiphilic diblock copolymers for molecular recognition are described. Poly(butadiene)-block-poly(ethylene oxide) copolymers were synthesized using living anionic polymerization. End groups were functionalized with nitrilo triacetic acid (NTA) and tris(nitrilo triacetic acid), and their further complexation with nickel (II) and copper (II) led to selective ligands for oligohistidine complexation, often present at proteins chain end. The polymers were characterized by <sup>1</sup>H-NMR spectroscopy, size exclusion chromatography, electron paramagnetic resonance and UV-VIS spectroscopy. Mixtures of non-functionalized and functionalized polymers self-assemble in aqueous solution into vesicular structures with a controlled density of metal complex end groups on their surface. These polymer mixtures also form monolayer on water, as shown by Langmuir isotherms experiments. Optical Microscopy, Transmission Electron Microscopy and Brewster Angle Microscopy were used to image the functionalized amphiphilic diblock copolymers self assembly motives. Vesicles were characterized by dynamic light scattering, static light scattering, small angle X-ray scattering and zeta potential. The binding sites accessibility was tested using model systems: maltose binding protein carrying a terminal decahistidine moiety, His-tagged enhanced green fluorescent protein and His-tagged enhanced yellow fluorescent protein. Fluorescence Microscopy was used to visualize the binding of the fluorescent proteins to the functionalized vesicles. Fluorescence correlation spectroscopy clearly showed a significant and selective binding of these proteins to the vesicle surface. Furthermore, atomic force microscopy clearly demonstrated that the Ni-NTA functionalized polymer adsorbs in an oriented manner on highly oriented pyrolytic graphite surfaces and is able to induce a 2D protein crystallization.

---

## Acknowledgements

I thank my supervisor, Prof. Dr. Wolfgang Meier, for the generous facilities and the freedom of research that he provided. I am thankful to him for his patience (especially for his patience), support and humor, which, altogether, let me find my way in the field of research and gave me the opportunity to develop my emphatic skills.

I thank Dr. Cornelia Palivan for her great contribution, cooperation, knowledge and her special force to push a project. Her clear mind as well as her humor helped me to overcome scientific (and not only scientific) problems and to find a solution.

I thank Dr. Susana Moreno-Flores for her contribution, structure and her time during my PhD study. Also I am thankful for the discussions we had - inside and outside of the university.

I thank Dr. Violetta Malinova for her careful proof reading, her corrections on my thesis and her strong advises to increase my impact.

I thank Dr. Alexandre Manton for his collaboration, his ideas and comments on my work. Additionally I am thankful to him for his great discussions about the guidelines for a perfect espresso.

I thank my former mentor and co-referee Dr. Jean-Francois Lutz for his interest to my research work.

Very much I thank Sven Kasper for his laboratory skills and his technical impact of my thesis.

Also, I would like to thank Grischa Martin of the workshop for his mechanical task forces and his ability to find a solution – always.

Many thanks go to the whole Meier group as all members accepted me as I am and supported me with their knowledge, energy and their patience.

Special thanks go to all laboratory members (left chem. lab) for their great contribution and passion for cleaning.

Special thanks go to “my” master student Pascal Tanner who continues our project and helped me writing and formatting my thesis.

Also, special thanks go to Lucy Kind, as she is as she is.

---

This work would not have been completed without people who helped me with measurements and techniques. Many thanks are addressed to my collaborators:

Prof. Dr. José Luis Toca-Herrera (biosurfaces unit, CIC biomaGUNE, San Sebastian, Spain)

Dr. rer. nat. habil. Helmut Schlaad (Max Planck Institute of Colloids and Interfaces, Amphiphilic Block Copolymers, Potsdam-Golm, Germany)

Marlies Gräwert for GPC measurements

Ines Below for her professional introduction to anionic polymerization techniques

Dr. habil. Andreas F. Thünemann (Direktor und Professor, Bundesanstalt für Materialforschung (BAM), Berlin, Germany)

Prof. Dr. Robert Tampé (Johann Wolfgang Goethe-Universität Frankfurt am Main Institute of Biochemistry, Biocenter, Frankfurt, Germany)

the unknown chemist for the NTAs and TrisNTAs

Ao.Univ.Prof. Dipl.-Ing. Dr.techn. Dietmar Pum (Zentrum für Nanobiotechnologie, Universität für Bodenkultur Wien (BOKU), Wien, Österreich)

Dr. Daniel Häussinger for the NMR support (Department of Chemistry, University of Basel, Basel, Switzerland)

Dr. Markus Dürrenberger (Microscopy center, Pharmazentrum, University of Basel, Basel, Switzerland)

Gianni Morson for his good mood and the TEM and Cryo-TEM (!) images

Vesna Olivieri for the introduction in sample preparation

Additionally I would like to thank my friends at • • and • •, who are: Peter, Rüdiger, Rudolf, Torsten, Helga, Edgar, Diego, Rita, Michèle, Fabian, Andrea, Jean-Yves, André, Hans and many others – without them, I never would have succeeded.

Warm thanks go to Anika for the nice meetings in Basel and on Rüti, for the good conversations we had.

Also I would like to thank my mother for her support in many affairs.

Last but not least I would like to thank my son Johannes, just for being here.

*BioPolySurf–Marie Curie Research Training Network (BPS–Marie Curie RTN), the National Centre of Competence in Research (NCCR) of Nanoscale Science and the Swiss National Science Foundation (SNCF) are acknowledged for financial support.*

---

## Content

1. Introduction.....	1
1.1 Characterization of membrane proteins: a motivation .....	1
1.2 Lipid monolayers: a simplified model of biomembranes for 2D crystallization of proteins .....	2
1.3 Amphiphilic Diblock Copolymer Membranes: a challenging alternative.....	6
1.4 Approach.....	9
1.5 Scope of the thesis .....	10
1.5.1 Polymer choice: poly(butadiene)-block-poly(ethylene oxide) (PB-PEO).....	10
1.5.2 Polymerization technique: Anionic Polymerization .....	11
1.5.3 One Pot Procedure.....	12
1.5.4 Functionalization with Lys-NTA-Ni <sup>2+</sup> groups .....	13
1.5.5 Characterization of diblock copolymers self-assembly and functionality: specific targeting of proteins.....	14
2. Experimental Part.....	15
2.1 Chemicals .....	15
2.2 Synthesis .....	16
2.2.1 Concept of Reaction .....	16
2.2.2 The Anionic Polymerization Set up.....	20
2.2.3 Synthesis of the polymers and basic analysis .....	22
2.2.3.1 Polymer Synthesis and Characterization of the NTA diblock copolymer (PB <sub>60</sub> -PEO <sub>34</sub> -SA-NTA.d-Ni <sup>2+</sup> ).....	22
2.2.3.2 Polymer Synthesis and Characterization of the TrisNTA diblock copolymer (PB <sub>39</sub> -PEO <sub>36</sub> -SA-Tris.NTA.d-Ni <sup>2+</sup> ) .....	28
2.3 Polymer Characterization Methods .....	32
2.4 Vesicle Formation .....	34
2.4.1 Electroformation .....	34
2.4.2 Rehydration .....	36
2.4.3 Extrusion.....	37
2.5 Vesicle Characterization Methods .....	37
2.5.1 Optical Microscopy (OM).....	37
2.5.2 Transmission Electron Microscopy (TEM).....	37
2.5.3 Cryo-Transmission Electron Microscopy .....	37
2.5.4 Light Scattering.....	38
2.5.5 Small Angle X-ray Scattering.....	42

---

2.5.6 Inductively Coupled Plasma Atomic Emission Spectroscopy (ICP-AES)	43
2.5.7 Zeta-Potential ( $\xi$ -potential)	43
2.5.8 Atomic force (scanning) microscopy (AFM)	44
2.5.9 Quartz Crystal Microbalance (QCM)	45
2.5.10 Fluorescence Correlation Spectroscopy (FCS)	46
2.6 Formation of Monolayers	47
2.6.1 Langmuir Isotherms	47
2.6.2 Langmuir-Schaeffer films on graphite (HOPG)	48
2.7 Characterization Methods of Monolayers	49
2.7.1 Langmuir Isotherms & Brewster Angle Microscopy (BAM)	49
2.7.2 AFM of monolayer and of monolayer + protein, both on HOPG	49
3. Results	51
3.1 polymers	51
3.1.1 List of mixtures of functionalized diblock polymers	54
3.1.2 Characterization of Metal-functionalized diblock copolymers	55
3.1.2.1 UV/ VIS: Cu, Ni	55
3.1.2.2 EPR: Cu	56
3.2 Vesicles	58
3.2.1 Giant vesicles and vesicular structures	58
3.2.1.1 Optical microscopy imaging	59
3.2.1.2 TEM	65
3.2.1.3 Cryo-TEM	66
3.2.2 Vesicles morphology	66
3.2.2.1 Dynamic Light Scattering (DLS) and Temperature Dependence	67
3.2.2.2 Dynamic Light Scattering	67
3.2.2.3 Static Light Scattering (SLS)	68
3.2.2.3 Small Angle X-ray Scattering (SAXS)	70
3.2.3 Metal doped vesicles surface functionality	74
3.2.3.1 Vesicle zeta potential	74
3.2.3.2 Metal content as determined by Inductive Coupled Plasma Atom Emission Spectroscopy (ICP-AES)	75
3.2.4 Vesicle Adsorption on Surfaces	76
3.2.4.1 QCM: graphs	76
3.2.4.2 AFM imaging	79
3.2.5 Protein binding to functionalized vesicles	80
3.2.5.1 Fluorescence microscopy: "rings" in solution	80

---

---

3.2.5.2 Fluorescence Correlation Spectroscopy (FCS): His-tag protein binding to the surface of the copolymer vesicles.....	82
3.2.5.3 Quarz Crystal Microbalance (QCM): Protein binding to the vesicles .....	85
3.3 Monolayers .....	88
3.3.1 Langmuir compression: isotherms; Brewster Angle Microscopy: images	88
3.3.2 AFM imaging of monolayer on highly oriented pyrolytic graphite (HOPG)	90
3.3.3 AFM: proof of the functionality of the monolayer by protein binding.....	92
4. Conclusions and Outlook .....	95
5. References .....	97

---

## Abbreviations

2D	two dimensional
AFM	atomic force microscopy
BAM	Brewster Angle Microscopy
CCD	charge-coupled device
CLIA	Chelating Ligand Internalization Assays
Da	dalton
DCC	dicyclohexylcarbodiimide
DLS	Dynamic Light Scattering
DMAP	4-(dimethylamino)pyridine
DMF	Dimethylformamide
DPPH	diphenylpicrylhydrazyl
EDTA	ethylenediaminetetraacetic acid
EGFP	enhanced green fluorescent protein
EO	ethylene oxide
EPR	Electron Paramagnetic Resonance
EYFP	enhanced yellow fluorescent protein
FCS	Fluorescence correlation spectroscopy
FITC	Fluorescein isothiocyanate
GFP	green fluorescent protein
GPC	Gel permeation chromatography
GUV	Giant unilamellar vesicles
His	histidine
HMBC	Heteronuclear multiple bond correlation
HMP	high melting point
HOPG	Highly Oriented Pyrolytic Graphite
HPLC	High pressure liquid chromatography
ICP-AES	Inductively Coupled Plasma Atomic Emission Spectroscopy
IDA	iminodiacetic acid
IFT	inverse function theorem
IMAC	meta ion affinity chromatography
Lys	lysine
MBP	maltose binding protein
MW	molecular weight
NHS	N-hydroxysuccinimide
NMM	n-methylmorpholin
NMR	nuclear magnetic resonance
NTA	nitrilo triacetic acid
OM	Optical Microscopy
PB-PEO	poly(butadiene)-block-poly(ethylene oxide).
PBS	Phosphate buffered saline

---

PC	Polycarbonates
PD	polydispersity
PDI	polydispersity index
PEG	poly(ethylene glycol)
PEI	poly(ethylene imine)
PS-b-PAA	poly(styrene)-block-poly(acrylic acid)
PSD	position-sensitive detector
QCM	quartz crystal microbalance
RT	room temperature
SA	succinic anhydride
SAXS	Small Angle X-ray Scattering
SEC	Size Exclusion Chromatography
SLS	Static Light Scattering
SUV	small unilamellar vesicle
t-BuP4	1- <i>tert</i> -butyl-4,4,4-tris(dimethylamino)-2,2-bis-[tris(dimethylamino)-phosphoranylidenamino]-2 <i>i</i> 5,4 <i>i</i> 5-catenadi(phosphazene)]
TEM	Transmission Electron Microscopy
TFA	trifluoroacetic acid
THF	tetrahydrofuran
Tris	Tris(Hydroxymethyl) aminomethane
TrisNTA	tris(nitrilo triacetic acid)
UV-VIS	ultraviolet-visible

---

# 1. Introduction

## 1.1 Characterization of membrane proteins: a motivation

Form follows function. This applies to designer chairs as well as to proteins. As basic modules of life<sup>1</sup>, proteins have very diverse, but precise functionalities as cargos, molecular machines or membrane channel controllers.

The chair we can sense with our eyes or hands and hence we can assign a function to it. But we cannot determine by eye the intimate spatial organization of proteins. Amino acids position mapping is required to describe these marvelous objects, and to find a structure/activity relation. X-Ray diffraction, since the 1950s, is the most important method to investigate protein structure. Already in 1912 Max von Laue recognized the potential use of single crystal diffraction as analytical technique when he irradiated with x-rays a zinc sulfate single crystal and indeed recorded the first regularly 2D placed black dots on a photo plate, today usually called Laue pattern.<sup>2</sup> These points are the result of x-rays diffraction at the crystal's regularly ordered atomic structure. The requirement of a highly organized structure excluded big protein molecules from diffraction investigations as they are notoriously difficult to crystallize. Instead of crystallizing, proteins and exceptional *membrane proteins* tend to precipitate during concentration and thus lose their functional form.<sup>3</sup> The first protein which was crystallized was the enzyme urease in 1926.<sup>4</sup> Meanwhile x-ray investigation of proteins gained a significant interest and also profit from high-flux sources like synchrotron and computational methods to efficiently solve structures.

Membrane proteins represent 20 to 30% of the existing proteins<sup>5</sup> and are essential for life, as they control and moderate cells interaction with their environment. For instance aquaporines play an important role in the water balance of cells.<sup>6,7</sup> Additionally, most membrane proteins are receptors for various drugs and pharmaceutically active substances, which make their structural elucidation crucial for health and industrial applications. The lack of structural information, in contrast to other protein classes, makes them poorly understood. Structural information of membrane proteins is difficult to obtain because of<sup>8</sup>: (1) Overexpression is difficult and thus only limited amounts are available for subsequent characterization, (2) their aggregative tendency makes them difficult to purify. Common purification methods are more based on laboratory practice rather than on a well established purification method. Moreover, detergents are required to prevent their aggregation and subsequent precipitation.

---

Anyway, functional and structural studies often require the oriented and functional immobilization of proteins. Physisorption of a protein to a surface by van de Waals or electrostatic interactions are highly sensitive towards ionic strength, pH, or temperature. This can lead to a loss of orientation and hence activity of the protein. Covalent binding of a protein via surface-accessible amino acids moieties to a reactive surface often lacks regioselectivity of the immobilized protein. Additionally, the reactive site of a protein can also be blocked by the immobilization procedure, which reduces the activity of the protein.<sup>9</sup> Protein binding by its natural ligand<sup>10, 11</sup> is only an option if the ligand can be bound to the surface and if the process of ligand binding is not the process desired to study. The affine binding of biotin to streptavidin can also be used for protein immobilization.<sup>10</sup> But this method requires an unspecific chemical biotinylation of the protein.

Immobilized metal ion affinity chromatography (IMAC)<sup>12, 13</sup> is a versatile and powerful tool for protein purification and characterization. Here proteins are expressed with a short affinity sequence of histidines (histidine-tag) that bind to metal ion complexes such as nickel(II)-nitrilotriacetic acid (Ni<sup>2+</sup>-NTA) or copper(II)-iminodiacetic acid (Cu<sup>2+</sup>-IDA) whereas the functionality of the protein is preserved. Additionally, the binding is reversible and dissociation can be induced at lower pH or by addition of a competitor for the protein (histidine, imidazole) and the metal ion (EDTA).<sup>14</sup>

## **1.2 Lipid monolayers: a simplified model of biomembranes for 2D crystallization of proteins**

Unfortunately the main membrane component – the lipid – seems simple and less attractive compared to the more appealing proteins and nucleic acids. This view is completely incorrect, because the prosaic lipid acts differently compared to proteins in general. Membrane lipids are molecules with amphiphilic characteristics: a hydrophilic head and a hydrophobic alkyl chain tail. In an aqueous system, the polar heads of lipids orientate towards the polar, aqueous environment, while the hydrophobic tails minimize their contact with water. The lipid lipophilic tails tend to cluster together, forming in water a lipid bilayer (i.e. vesicle) or micelles.<sup>10, 15</sup> For example the formation of lipid bilayers is an entropically-preferred process when the phospholipids are dispersed in an aqueous environment. Suddenly, lipids are not as trivial as thought. They are the ideal structural element for every known cell in nature. Lipid vesicles can undergo fusion, endocytosis and exocytosis, and they can incorporate proteins that form active or passive channels for the transfer of ions. Due to their amphiphilic characteristics, natural lipids form monolayers at the air/water

---

interface, which is one approach to mimic certain features of the cell membrane. Lipid monolayers or bilayers can be deposited on different surfaces (e.g. gold, silica, HOPG) by various techniques<sup>16, 17</sup> providing the membrane with biocompatibility and lateral mobility. Functional units of biomembranes such as channels or transporters can be reconstituted into vesicles and immobilized at the surface by vesicle fusion.<sup>18-20</sup> Due to their dynamic properties, lipids can be organized in two dimensions by phase segregation,<sup>21</sup> electrical fields,<sup>22, 23</sup> and microfabricated barriers,<sup>22</sup> allowing a generation of structured biofunctional interfaces.

Molecular recognition at surfaces plays a key role in many processes in nature.<sup>24</sup> Therefore appropriately designed surface structures containing biological recognition elements offer considerable potential as model systems to investigate such events in more details or to create new materials that undergo controlled interactions with biological systems.<sup>25, 26</sup> In particular, the selective binding of biologically relevant molecules via metal coordination using, for example, complexes with nitrilo triacetic acid (NTA) ligands can be exploited for their functional and oriented immobilization.<sup>27</sup> Combining such metal-based recognition sites with molecules that are inherently able to self-assemble into well-defined supramolecular structures opens the possibility to induce a high ordered self assembly.<sup>28, 29</sup> Functionalized synthetic lipids with chelating NTA-Ni<sup>2+</sup> groups have been used to design surfaces that can serve as templates for 2D protein crystallization,<sup>30-38</sup> and to create metal-affinity-tethered membranes for investigating the complex network of recognition, transport and signaling processes at membranes.<sup>39</sup> Metal-NTA lipids/liposomes are used in so-called 'Chelating Ligand Internalization Assays' (CLIA) to screen antibodies for their ability to confer target-specific toxicity in tumor treatment<sup>40</sup>, as specific inhibitors in integral metalloenzyme activity tests<sup>41</sup>, or in the therapeutic domain as vaccines or modulators of intracellular signaling pathways by attaching His-Tag peptides and proteins to the metal region of the system.<sup>14, 42</sup> Nevertheless, in any cases an aqueous environment (i.e. buffers) is mandatory for the investigations of lipid mono- and bilayers.

When the system, a lipid film, is prepared on the air/water interface, and subsequently a membrane protein is added to the subphase, specific interactions take place between the solute and the monolayer. Perfect interaction between the various species (protein, lipid, detergent and solvent) is one of the prerequisites for a successful 2D crystallization. Moreover, many other parameters have to be taken into account like temperature, buffer composition, concentration and pH value, making the process relatively difficult. Taking into account the weak features of natural lipid membranes such as sensitivity, permeability, poor mechanical stability and fluidity, the development of a synthetic equivalent, where these

---

disadvantages could be minimized or eliminated is a challenge of natural science. To some extent, this has been partially achieved by producing simple synthetic lipid membranes even so stability and permeability issues were not addressed.<sup>8, 43</sup>

A number of reviews describe different methods to produce and analyze the 2D protein crystals and to understand the physico-chemical interactions involved in the crystallization process.<sup>10, 44-48</sup> Depending on the technique, various supramolecular structures have been used as model membrane systems to prepare 2D crystals of membrane proteins: liposomes (i.e. vesicles), lipid bilayers, supported lipid bilayers and monolayers. In the case of lipids, protein crystallization has been described to proceed in three steps:<sup>8, 44</sup> (1) Molecular recognition between soluble proteins and specific lipid ligands, (2) Diffusion of lipid-protein complexes in the plane of the film and (3) Self-organization of the proteins into a 2D crystalline structure, see Figure 1.

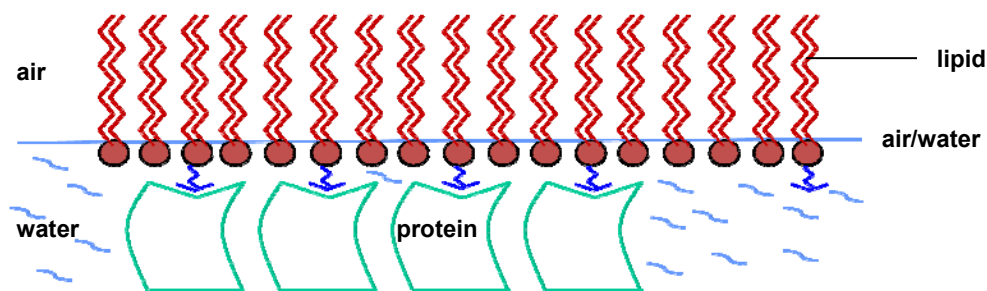


**Figure 1:** 2D protein crystals beneath a lipid layer

The last step is simplified by the hydrophilic lipid head group functionalized with a specific recognition side for the protein such as  $\text{Ni}^{2+}$ -NTA (nitriloacetic acid)<sup>30-33, 35, 37, 38</sup>,  $\text{Cu}^{2+}$ -IDA (iminodiacetate)<sup>49</sup> or biotin. Genetically engineered proteins contain terminal histidine units enabling coordination with synthetic lipids functionalized with  $\text{Ni}^{2+}$ -NTA groups.<sup>43</sup> The group of Tampé<sup>14</sup> reported the synthesis of fluorescent chelator lipids which served as spectroscopic probes to follow the binding process. Molecular recognition was followed at lipid monolayers at the air-water interface and at lipid bilayers in vesicle solution. Additionally, specific binding of single histidine-tagged molecules to NTA containing lipid vesicles were demonstrated by fluorescence correlation spectroscopy (FCS).<sup>14</sup> Due to their intrinsically different diffusion times through a confocal volume, the ratio of free and lipid vesicle bound molecules was analyzed by the autocorrelation function of the time dependent fluorescence signal, see Figure 2.<sup>14</sup>

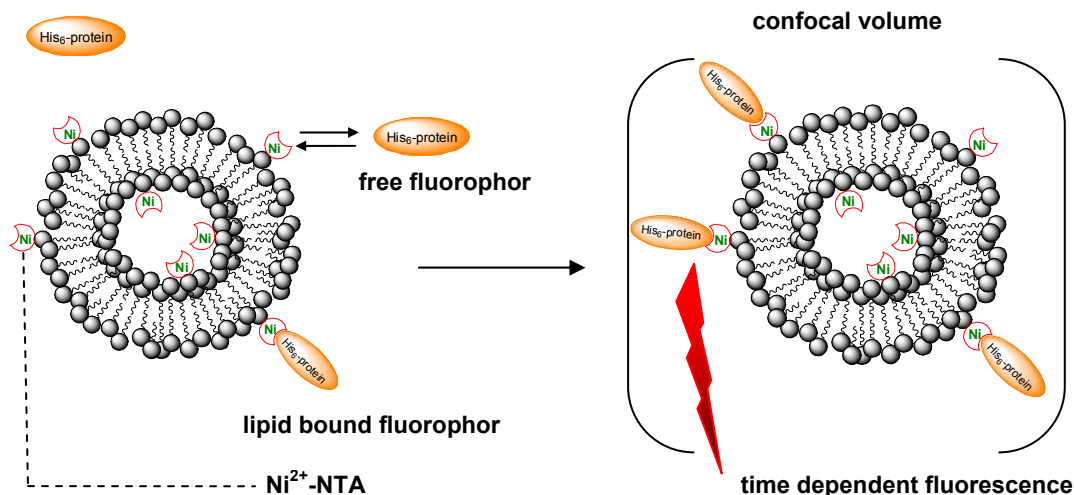


**Figure 2:** Scheme of the Fluorescence correlation spectroscopy of surface active lipid vesicles. The time dependent fluorescence signal of fluorophore labeled histidine tagged proteins was analyzed regarding to their different diffusion times in the free or lipid bound state.

2D protein crystallization using functionalized lipids at the air/water interface is already a well established method but lacks robustness as lipids are intrinsically sensitive to residual surfactants and other environmental conditions, such as buffer composition and temperature.<sup>50-52</sup> Tuning their interaction with other molecules, polymerizing them and in general controlling their chemistry is not always possible. Moreover, their physical properties as, for example, their naturally limited size are hindering more advanced applications.

On the other hand, amphiphilic diblock copolymer membranes can be an improvement to the lipid's matrix, also functionalized and hence able to bind membrane proteins, but characterized by a higher stability and lower permeability.<sup>34, 51, 52</sup> It is possible to create flexible but extremely stable membranes by crosslinking the vinyl moieties of the hydrophobic part of an amphiphilic polymer. The hydrophilic strands of the diblock copolymers can be tailored in a way (e.g. length, side chains) that they protect proteins from popping up to surfaces.<sup>53, 54</sup> These amphiphilic diblock copolymers can be synthesized with a very low polydispersity, and a high yield by several techniques such as the anionic polymerization<sup>55</sup> or controlled radical polymerization. Additionally their length and their hydrophobic to hydrophilic ratio can be easily determined by the amount of the inserted initiator and monomer.<sup>55</sup> Moreover, polymer active chain ends can be functionalized individually by adding the corresponding functional group to the polymerization mixture.<sup>56</sup> Therefore it is possible to tailor the desired properties of an amphiphilic diblock copolymer and its favored functionality at a laboratory as well as at industrial scale.

---

### 1.3 Amphiphilic Diblock Copolymer Membranes: a challenging alternative

Similarly to lipids, amphiphilic diblock copolymers can self-assemble in aqueous media into membrane structures and produce vesicular structures in solution.<sup>57</sup> Even though the stability of lipid and polymer vesicles vary due to their different chemical composition, the principle of their formation is the same: both are held together solely by non covalent interactions.<sup>58-60</sup> Block copolymers composed of two chemically different blocks can separate into a variety of morphologies.<sup>61-63</sup> This self-assembly process<sup>64</sup> is driven by an unfavorable mixing enthalpy and a small mixing entropy, while covalent bonds between the blocks prevent macro phase separation.<sup>65</sup> Depending on the polymers used and their volume fractions, various morphologies of self assemblies are formed such as spheres, lamellae, inverse spheres and more complex shapes.<sup>66</sup>

In aqueous (polar) media and at certain conditions, the block copolymer macromolecules merge by their non-polar parts to form micelles or vesicles. Oriented amphiphilic molecules in vesicle membranes are able to move freely in the tangential direction along the boundary between the polar and non-polar regions of a membrane. The movements of the amphiphilic molecules are only restricted along the normal.<sup>65</sup> Therefore, vesicles can be viewed as two-dimensional liquids and one-dimensional solid bodies. Owing to their two-dimensional fluidity many non spherical shapes such as wormlike micelles, oblate objects and nanotubes can be observed.<sup>65</sup> Additionally, their 2-dimensional fluidity allows bigger vesicles to pass through membranes with smaller pore sizes than their diameters.<sup>65</sup>

The first approach to understand the thermodynamics of vesiculation in a diblock copolymer system was given by Wang.<sup>67</sup> This study focused on the stability of a bilayer membrane upon spherical deformations, in particular whether and why a curved bilayer would be favored over a flat one. The calculations of free energy per diblock copolymer molecule for a general deformation lead to the conclusion that whenever the composition of the diblocks is sufficiently asymmetric with longer hydrophobic blocks, the constituent monolayers will have a strong tendency to curve away from the aqueous phase. In conclusion vesicles become favored over the flat bilayers. The lower free energy of vesicles as compared to flat bilayers is explained as follows: when each monolayer has a tendency to curve away from the solvent, this new geometry decreases the free energy of the outer layer, whereas the free energy of the inner membrane increases. When - for the inner leaflet - the number of molecules per unit area decreases, the increase of the inner membrane free energy can be partly diminished. Moreover, since there are more molecules in the outer monolayer, the free energy decrease in the outer shell will compensate the free

---

energy increase in the inner layer.<sup>65, 67</sup> For example, stability of vesicles was experimentally verified for poly(styrene)-b-poly(acrylic acid) (PS-b-PAA) in a dioxane-THF-water mixture or a DMF-THF-water mixture.<sup>67, 68</sup>

The self-assembly process in block copolymer systems leading to vesicle formation has been concisely reviewed by Antonietti and Förster<sup>58</sup> who consider vesiculation in terms of a bilayer formation, which will next close to form a vesicle. Classically, the shape of self-assembled structures is determined by the size of the hydrophobic blocks (at a constant hydrophilic block length provided), which further influences the curvature of the hydrophilic-hydrophobic interface. The interface is described by two parameters<sup>58, 69</sup>, the mean curvature  $H$  and the Gaussian curvature,  $K_G$ , defined by the two radii of curvature,  $R_1$  and  $R_2$ :

$$H = \frac{1}{2} \left( \frac{1}{R_1} + \frac{1}{R_2} \right) \quad (\text{eq. 1})$$

$$K_G = \frac{1}{R_1 R_2} \quad (\text{eq. 2})$$

According to<sup>70</sup>, the interfacial curvature is related to the surfactant packing parameter as follows:

$$\frac{v}{al} = 1 - Hl + \frac{K_G l^2}{3} \quad (\text{eq. 3})$$

where  $v$  is the hydrophobic volume of the amphiphile,  $a$  is the interfacial area of the hydrophobic volume and  $l$  is the chain length of the hydrophobic segment.<sup>71</sup>

The packing parameter  $v/al$  determines the geometry of the aggregates. Hence, when  $v/al < 1/3$ , spherical micelles are formed, and when  $1/3 < v/al < 1/2$ , cylindrical micelles are observed, whereas  $1/2 < v/al < 1$  corresponds to vesicles.<sup>59</sup> If  $v/al = 1$ , planar bilayers are formed, and finally for  $v/al > 1$ , inverted structures are expected. These trends are well established for small surfactants and lipids and are generally valid also for amphiphilic block copolymers. In diblock copolymer systems the packing parameter will only give an estimate of the morphologies present in the system, as the actual situation depends on the complex balance among a large number of forces.<sup>72</sup> Anyway, it is more convenient to use the volume or weight fraction  $f$  of the hydrophobic block ( $0 < f < 1$ ) to describe the shape of amphiphilic diblock copolymers. In fact, decreasing the lengths of the hydrophilic blocks at constant hydrophobic block lengths causes a transition from spherical to wormlike micelles and finally to vesicular structures.<sup>73, 74</sup> It is suggested that a starting point for generating polymersomes in water is a ratio of hydrophilic to hydrophobic block to total mass:  $f = 35\% \pm$

---

10%.<sup>75</sup> Molecules with  $f > 45\%$  can be expected to form micelles, whereas molecules with  $f < 25\%$  can be expected to form inverted structures. Copolymers with average MWs ranging from 2,000 to 20,000 Da following the rule showed the ability to form vesicles.

The possible morphologies found in the experiment are much more than the theoretical predictions, and additional energy contributions as well as solvent concentrations seem to enable a fascinating variety of aggregates that form spontaneously. Many other fascinating shapes have been described.<sup>58, 65, 76</sup>

Nevertheless amphiphilic diblock copolymers are unique and versatile building blocks in supramolecular polymer chemistry, both for the generation of highly organized, self-assembled structures and for the structural control of material interfaces.<sup>77</sup> Precise control of the created architecture is exerted by careful choice of the block's molecular structure. Each block has a different polarity, structure, and chemical functionalities.

During the last decades, numerous studies have focused on combining the unique functional properties and structural characteristics of proteins with those of synthetic macromolecules. The aim of such multidisciplinary studies is to improve the properties of the natural component, to combine them with those of the synthetic, and to create novel biomaterials in the nanometer scale. The specific coupling of polymers with proteins has proved to be one of the most straightforward and applicable approaches in this sense.<sup>78</sup> Theoretically, the properties of the protein-polymer hybrids should simply be a synergistic combinatorial function of amphiphilic block copolymers and proteins and should ideally lead to overcome some of their intrinsic limitations. This idea has been pursued in the area of pharmaceuticals where one of the "holy grails" is still the stabilization and enhancement of the action of therapeutics (proteins and drugs) without comprising their stability.<sup>79-81</sup> Furthermore, assemblies incorporating biological components are particularly attractive as supramolecular biomaterials, lab-on-a-chip components and as building blocks in microfluidics and bioprocessing applications.<sup>82-86</sup>

Moreover, it has been shown that block copolymer membranes can be modified with specific recognition sites by attaching, for example, biotin groups to the hydrophilic ends of the polymers,<sup>87-89</sup> or by insertion of integral membrane protein receptors.<sup>90</sup> Likewise, it could be expected that block copolymers could be functionalized with metal chelating moieties without affecting their ability to self-assemble into well-defined membrane structures. Such entities could serve as a model to study the binding of proteins to artificial membranes mimicking biological properties.

Hence, the block copolymer membranes attract a considerable attention due to the variety of their physical, chemical and biological properties. Their chemical constitution (e.g.

---

nature of the repeat units), the relative length and the structure of the different blocks, or even the architecture of the whole polymer can be designed with respect to the desired application.<sup>77, 91, 92</sup> Generally block copolymer membranes are considerably thicker and both chemically and mechanically more stable than the conventional lipid bilayers.<sup>93</sup>

## 1.4 Approach

Model amphiphilic block copolymers with narrow molecular weight distributions, controllable block lengths, and high purity are required for mimicking bio membranes.

These requirements are met by poly(butadiene)-block-poly(ethylene oxide) diblock copolymers. The hydrophobic blocks (PB) are crosslinkable under UV light. The diblock copolymer PB-PEO is synthesized by a modified conventional anionic polymerization.<sup>94</sup>

The copolymer PB-PEO forms monolayers at the air/water interface with an excellent stability as their lateral diffusion is hindered due to their size.<sup>55</sup> Moreover, the polymer is characterized by a high flexibility and a high lateral compressibility.<sup>65, 95</sup> The diblock copolymers can be condensed by Langmuir monolayer compression and hence configure the surface-matrix for a 2D crystallization. Therefore we assume that the crystallization process can be solely controlled by the pressure imposed to the surface. The hydrophilic block can serve as a flexible spacer for immobilization of the coordination site. In contrast to lipids the diblock copolymers have a low sensitivity to experimental conditions such as temperature and pH value. Furthermore, within one polymer molecule, various properties can be combined, such as coordination sites, functional groups and other sites providing different interaction possibilities.<sup>73</sup>

Due to their length and hydrophobicity, poly(butadiene) chains are suitable to attach predominately to hydrophobic surfaces such as highly oriented pyrolytic graphite (HOPG).<sup>96</sup> Thus poly(butadiene) could serve as adhered supporting layer for surface measurements of crystallized proteins using atomic force microscopy (AFM) or quartz crystal microbalance (QCM).

Relying on the valuable properties of polymers, our main goal was to investigate the possibilities to use amphiphilic diblock copolymers as templates for controlled immobilization. Due to the specific functionality and stability of polymers, they might constitute a very promising system for 2D-protein crystallization of proteins, see Figure 3.

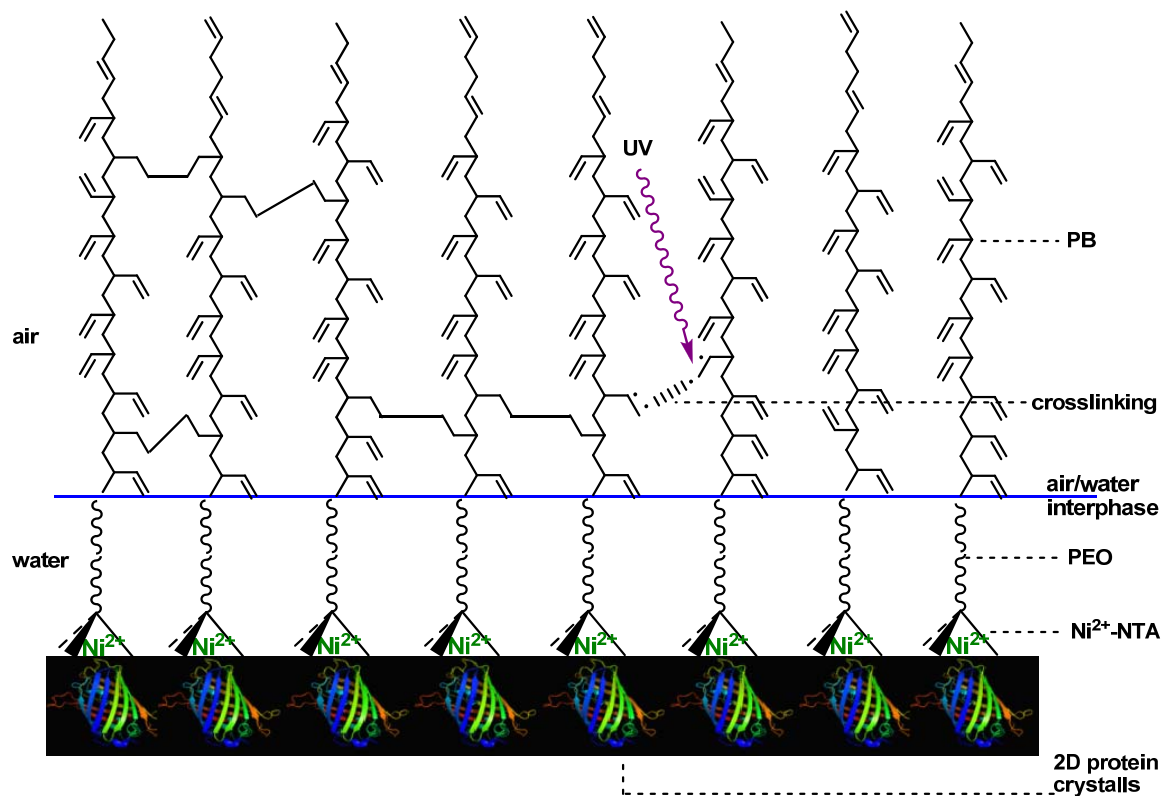


**Figure 3:** Model scheme: 2D protein crystals beneath a PB-PEO-NTA-Ni<sup>2+</sup> monolayer

## 1.5 Scope of the thesis

The strategy of this thesis implies the synthesis of amphiphilic diblock copolymers with terminal NTA-Ni<sup>2+</sup> complexes at the hydrophilic block ends as well as the description of the self assembly behavior and the analysis of the specific binding of the NTA-Ni<sup>2+</sup>-copolymers to His-tagged proteins.

Here, the choice of the diblock copolymer, the polymer synthesis and further functionalization with lysine-NTA-Ni<sup>2+</sup> complexes at the hydrophilic block end are discussed. Analytical methods are mentioned at the end of the section.

### 1.5.1 Polymer choice: poly(butadiene)-block-poly(ethylene oxide) (PB-PEO)

Functionalized poly(butadiene)-block-poly(ethylene oxide) polymers were synthesized and used as model systems to study their binding abilities to histidine tagged proteins. The self assembling behavior of these polymers and their derivatives in aqueous media has been carefully characterized.<sup>95-98</sup> In addition, the pendant poly(butadiene) block double bonds within the vesicular membranes can be covalently crosslinked within the self-

---

assembled superstructures,<sup>99</sup> leading to further structural stabilization by introducing a rubber-elastic character to the structures.<sup>95</sup>

Lithium-salt catalyzed poly(butadiene) (PB) synthesis results in a poorly stereo controlled polymer.<sup>100</sup> The alkyllithium system produces a polymer of 90% 1,4-poly(butadiene) with about 40% *cis*, 50% *trans* and of 10% 1,2-poly(butadiene) with vinyl groups when no special polar modifiers are used in the process.<sup>101</sup> Vinyl groups increase poly(butadiene)'s  $T_g$  by creating a stiffer chain structure. In vinyl units the double bonds are pendant to the main chain, giving rise to the special properties of high vinyl (50-70% 1,2-units) polymers. Vinyl groups also tend to crosslink and therefore the vinyl rich polymers are thermally unstable. Anyway poly(butadiene) is a highly resilient synthetic rubber.<sup>101</sup>

But the properties of the polymer can be better controlled by anionic polymerization. Here, the polymer can be synthesized with a high yield, with a very low polydispersity and a high grade of purity which characterizes the polymer as a perfect hydrophobic moiety of a synthetic membrane.

Poly(ethylene oxide) (PEO) has a low toxicity<sup>102</sup> and is used in a variety of products ranging from ingredients in cosmetics (e.g. skin creams) to pharmaceuticals as drug delivery systems.<sup>103</sup> The use of poly(ethylene oxide) as hydrophilic block derives from its favorable macromolecular properties as narrow MW distribution and end functionalization as well as from its high hydrophilicity and biocompatibility. Poly(ethylene oxide) is a flexible and water-soluble polymer which is unlikely to have specific interactions with biological molecules. As PEO is protein repellent, interaction with a protein must be based on functional groups present at the chain end. Additionally poly(ethylene oxide) is as a protective spacer preserving the proteins. PEO hinders the proteins to diffuse into the monolayer because of its dense alignment in the monolayer and its hydrophilic and therefore protein repellent environment. Since PEO prevents proteins (e.g. membrane proteins as aquaporins) from popping up onto the surface (contact with air), proteins retain their active structure.

### **1.5.2 Polymerization technique: Anionic Polymerization**

The beauty of anionic polymerization lies in the lack of termination reactions when carried out under appropriate conditions, i.e. we observe a living polymerization. This means that the propagating species (i.e. carbanion) remain unchanged at the chain end when the monomer is extensively consumed, so subsequent chemical reactions, such as functionalization, termination or further polymerization can be carried out. Under the appropriate polymerization conditions, termination reactions do not occur which requires an

---

additional quenching using a compound such as water or alcohol to terminate the process. The new anionic species are too weak to reinitiate.

The alkyllithium process is probably the most versatile, because the growing chain end contains a “living” anion which can be further reacted with coupling agents or functional groups to make a variety of modified polymers, here: poly(butadienes). Anionic polymerization also produces gel-free poly(butadienes) making it ideal for modification.<sup>54</sup> The vinyl unit amount in poly(butadiene) can be increased with lithium-based anionic polymerization through the use of nitrogen or oxygen-containing polar modifiers.<sup>55, 101</sup> The modifiers direct the attack of the propagating anion on the “living” chain end to give a 1,2 addition to the butadiene monomer. Around 10% of the polymer is a mixture of cis- and trans-1,4-Poly(butadiene). This polymer has a higher glass temperature  $T_g$ , but is still rubber-elastic and flexible at RT and very easy to crosslink.

If the chain ends remain reactive when the monomer is consumed, another monomer can be added leading to the propagation of a new chain covalently bound to the previous one (block copolymers). Living polymerization is required for successful synthesis of block copolymers as no side chain reactions take place. The anionic polymerization mechanism can be described as follows:

- Chains are initiated all at once (fast initiation).
- Little or no termination (except purposeful) occurs.
- Little or no depolymerization takes place.
- All chains grow under identical conditions.

The MW distribution in living anionic polymerization is:

- narrow (polydispersity PD is typically 1.05 - 1.20)
- predictable

For monofunctional initiators, the chain length is simply  $x = [\text{monomer}] / [\text{initiator}]$ . For difunctional initiators, the chain length is twice as large.

### 1.5.3 One Pot Procedure

The main disadvantage of anionic polymerization is its sensitivity toward water, alcohols, molecular oxygen and carbon dioxide. Indeed, all of them react very quickly with the chain ends carbanion, terminating the propagation.<sup>104</sup> Therefore extensive drying and deoxygenation of the polymerization reagents are required to insure a true living system. To overcome these problems, an anionic polymerization setup was especially designed and

---

installed. This set up provides the possibility for a one pot procedure under oxygen- and moisture-free conditions. Several flasks are connected to the vacuum line and the reaction flask can be provided with dried and redistilled monomers at any time. The solvent is separately dried and deoxygenated in a solvent flask and can be directed to desired reaction flasks upon distillation. The set up enables the synthesis of an amphiphilic block copolymer and its end-capping with a functional group in a one pot procedure. The set up is shown in Figure 13 and Figure 14.

The one pot procedure considerably simplifies the anionic polymerization, providing the required inert conditions and thus appears to be an elegant technique due to its higher efficiency. Additionally this approach minimizes impurities and a higher yield is obtained as only one set up is used and purification is performed as last step.

#### **1.5.4 Functionalization with Lys-NTA-Ni<sup>2+</sup> groups**

At the end of the hydrophilic part (PEO), the diblock copolymer still presents an active group, which can be further functionalized with Lys-NTA groups. Lys-NTA groups are soluble in water only upon a slight heating. To overcome the problem of solubility in organic solvents, Lys-NTA groups with hydrophobic protecting *tert*-butyl groups were used for polymer functionalization. The protected Lys-NTAs are soluble in common organic solvents as chloroform or tetrahydrofuran, and are thus ideal for synthesis. Moreover, only the metal complexing moieties of the NTA groups are protected and the free amino group of the Lys-NTA.p remains free for further reaction with the polymer hydrophilic side. The diblock copolymers functionalized with Lys-NTA groups require final deprotection before further use. The advantage of this procedure lies in the full protection of the complexing moieties until the end of the synthesis.

Poly(butadiene)-block-poly(ethylene oxide) copolymers functionalized with nitrilo triacetic acid (Lys-NTA) and tris(nitrilo triacetic acid) (TrisNTA) were complexed with nickel (II) and copper (II), known to selectively bind to oligohistidine residues of proteins. Mixtures of functionalized and the corresponding non-functionalized block copolymers self assemble in aqueous solution into vesicular structures, with a controlled density of the metal complex end-groups on their surface.

---

### **1.5.5 Characterization of diblock copolymers self-assembly and functionality: specific targeting of proteins**

The structure and molecular mass of the polymers were confirmed by  $^1\text{H-NMR}$  spectroscopy and Size Exclusion Chromatography, while the metal functionalization was established by Electron Paramagnetic Resonance and UV-VIS spectroscopy.

In order to demonstrate, image and quantify the self-assembling structures the following characterization tools were applied: Optical Microscopy, Transmission Electron Microscopy and Brewster Angle Microscopy. Further investigations and characterizations on vesicle structures were conducted with Dynamic Light Scattering, Static Light Scattering, Small Angle X-ray Scattering and Zeta potential measurement. Moreover Quartz Crystal Microbalance measurements and Atomic Force Microscopy were performed to determine the binding affinities of vesicles on surfaces. Monolayer behavior was quantified with Langmuir isotherms.

In order to check and quantify the diblock copolymers functionality, the fluorescent His-tag proteins targeting technique was adopted. Fluorescence correlation spectroscopy investigations were used to quantify the binding of His-tagged proteins to the metal sites at the surface of the metal-NTA functionalized diblock copolymer vesicles. Fluorescent Microscopy was used to visualize the fluorescent proteins binding to the functionalized vesicles. The AFM method was used to demonstrate the binding affinity of proteins on polymer coated surfaces as well as the 2D crystallization process.

---

## 2. Experimental Part

### 2.1 Chemicals

All reagents and solvents were purchased from Aldrich or Fluka with the highest purity grade and used as received unless otherwise noticed.

1,3-Butadiene (99+%, Aldrich) was cooled to  $-78^{\circ}\text{C}$  and successively distilled from  $\text{CaH}_2$  and *n*-BuLi. Ethylene oxide (EO) was also cooled to  $-78^{\circ}\text{C}$  and successively distilled from  $\text{CaH}_2$ , sodium mirror and *n*-BuLi to remove traces of water.

The phosphazene base *t*-BuP<sub>4</sub> (1-*tert*-Butyl-4,4,4-tris(dimethylamino)-2,2-bis[tris(dimethylamino)phosphoranylideneamino]-2 $\Lambda^5$ ,4 $\Lambda^5$ -atenadi(phosphazene)) (Fluka,  $1.00 \pm 0.02$  M in hexane) and N-Methylmorpholin (NMM) were used as received.

N,N-Bis [(*tert*-butyloxycarbonyl)methyl]-L-lysine *tert*-Butylester (Lys-NTA.p) and TrisNTA-OtBu (TrisNTA.p) as well as the His-tagged maltose binding protein conjugated to fluorescein (His<sub>10</sub>-MBP-FITC) were a gift from the group of Prof. Robert Tampé, Institute of Biochemistry, Biocenter, Goethe Universität, Frankfurt Marie Curie Strasse 9, D-60439 Frankfurt/ Main. They were used as received.

Tetrahydrofurane was refluxed over Na/K-alloy and stirred with until a purple color (with benzophenone) occurred; for synthesis the dried THF is distilled directly into the reactor prior synthesis.

Absolute ethanol (Scharlau), acetone (Sigma-Aldrich,  $\geq 99.9\%$ ) and chloroform (Sigma-Aldrich, 99.9%) were of HPLC grade and used without further purification. The polyelectrolyte used was the cationic poly(ethylene imine) (PEI, Sigma, 50 % w/w in water) at a concentration of 0.01 M with 0.5 M NaCl (Sigma,  $>99.5\%$ ). Milli-Q water (Nanopure diamond, Barnstead) with 18.2 M $\Omega$ -cm resistivity was used to prepare the polymer dispersions and the polyelectrolyte solutions.

The recombinant His<sub>6</sub>-EGFP (Abcam, Cambridge, UK) was used without further purification. For fluorescent measurements the His<sub>6</sub>-EGFP was diluted in phosphate buffer pH 7.4. The PBS buffer was made of 10 mM  $\text{HPO}_4^{2-}$ , 1.76 mM  $\text{H}_2\text{PO}_4^-$ , 157 mM  $\text{Na}^+$ , 4.46 mM  $\text{K}^+$ , 139.7 mM  $\text{Cl}^-$  and was adjusted to pH 7.4 with 1 M HCl solution. The TRIS buffer was made of 50mM TRIS and 100 mM NaCl and was adjusted to pH 8.0 with 1 M NaOH solution.

---

## 2.2 Synthesis

### 2.2.1 Concept of Reaction

Poly(butadiene)-block-poly(ethylene oxide) (PB-PEO) diblock copolymers were synthesized by living anionic polymerization. This technique offers the possibility to synthesize polymers with a narrow polydispersity and defined chain ends.<sup>105</sup> Anionic polymerizations are chain growth reactions in which a Lewis-base is used as initiator. In comparison to free radical polymerization it is possible to prevent termination reactions and keep reactive, living chain ends until they are quenched with desired end groups. As anionic polymerization is very sensitive to oxygen and moisture, water-free and air-free conditions are required.

A living anionic polymerization of 1,3-butadiene (**2**) with *s*-butyllithium (**1**) as initiator led to the formation of poly(butadiene) (PB, **3**). The ratio of 1,2- to 1,4-addition was 10:1. The first reaction step was the addition of the initiator **1** to the monomer 1, 3-butadiene (**2**) to form the anion. Due to resonance-stabilization of the anion, chain growth proceeds in two ways: 1,2- and 1,4-addition (Figure 4) with ratio 1,2-poly(butadiene)/1,4-poly(butadiene) 10:1.<sup>55</sup>

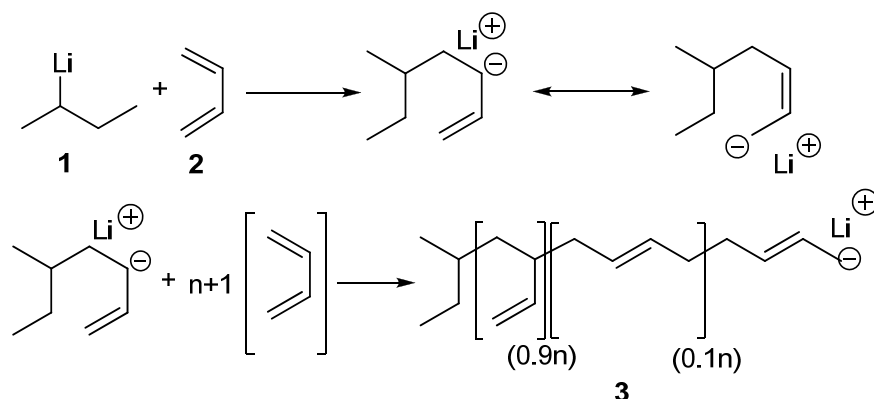


**Figure 4:** Mechanism of the synthesis of 1,2-poly(butadiene) (90%) and 1,4-poly(butadiene) (10%).

Addition of ethylene oxide (**5**) to the living end of poly(butadiene) (**3**) leads to the formation of poly(butadiene)-block-poly(ethylene oxide) (**6**, PB-PEO), still bearing a living end, Figure 5.

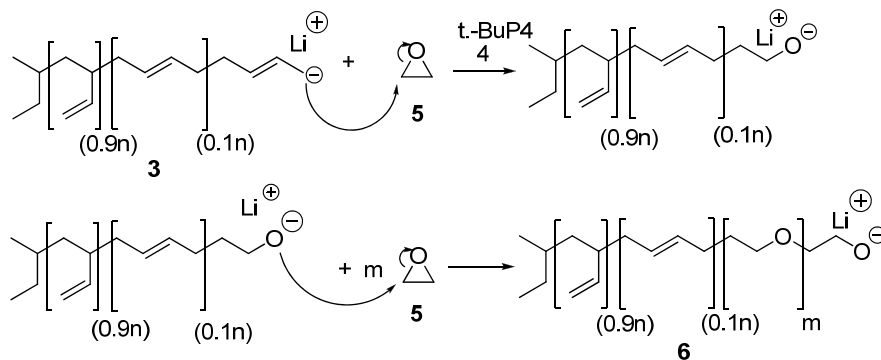


**Figure 5:** Mechanism of the synthesis of poly(butadiene)-block-poly(ethylene oxide).

The reaction was performed in the presence of the strong phosphazene base *t*-BuP<sub>4</sub> (4, Figure 6) to reduce the Li<sup>+</sup> association to the anionic end of the polymer chain. A strong ion pair formation would block the addition of ethylene oxide (5) to the living chain end of the poly(butadiene) (3) and no further polymerization would proceed [2].

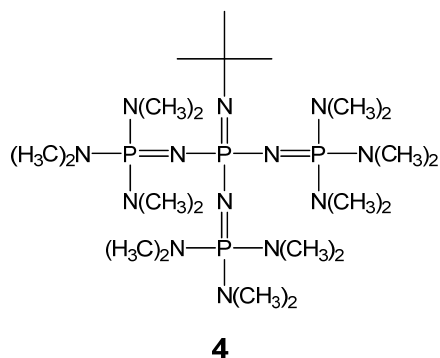


**Figure 6:** The phosphazene base *t*-BuP<sub>4</sub>.

The negatively charged chain ends were quenched by succinic anhydride (7) and the resulting salt was protonated with acetic acid. The product of the addition-elimination-mechanism was PB-PEO-SA-OH (8) as shown in Figure 7.

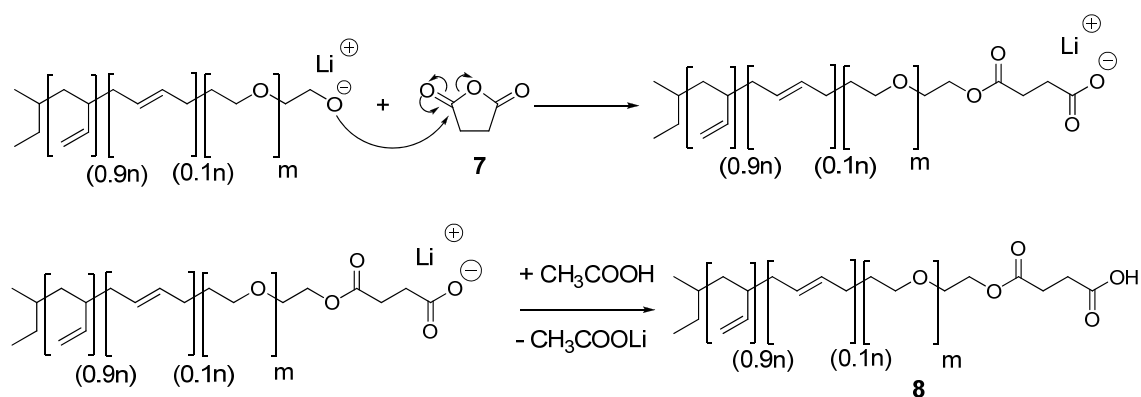


**Figure 7:** The addition-elimination-mechanism: PB-PEO-SA-OH.

---

The PB-PEO-SA-OH (**8**) was functionalized with two different protected nitrilotriacetate (NTA) groups, shown in Figure 8. After deprotection the nitrilotriacetate groups were able to form metal complexes via the carboxylic acid moieties with  $\text{Ni}^{2+}$  or  $\text{Cu}^{2+}$ .<sup>55</sup>

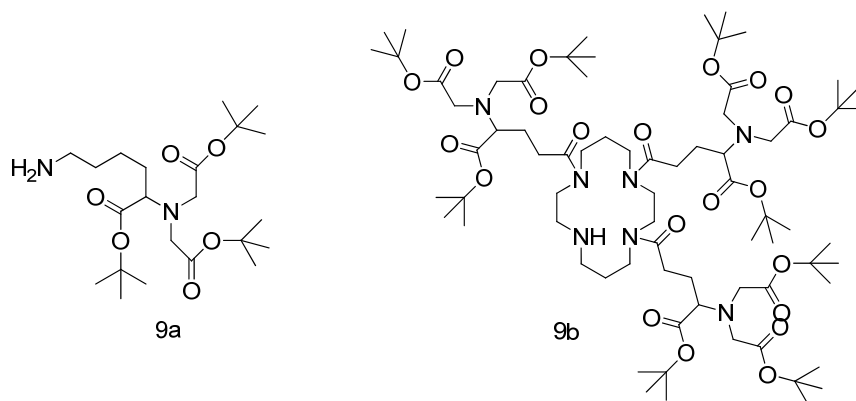


**Figure 8:** (**9a**) *N,N*-Bis[(*tert*-butyloxycarbonyl)methyl]-L-lysine *tert*-Butylester (NTA.p) and (**9b**) TrisNTA.p.; p = protected.

The amide bond between the functionalized copolymer (**8**) and the free amino group of the NTA (**9a**) and TrisNTA (**9b**) was formed by standard reagents<sup>14</sup>: dicyclohexylcarbodiimide (DCC), N-hydroxysuccinimide (NHS), 4-(dimethylamino)pyridine (DMAP) and triethylamine. The carboxylic end group of the copolymer (**8**) was deprotonated by the base 4-(dimethylamino) pyridine. Afterwards the polymer attacked dicyclohexylcarbodiimide (DCC) and formed dicyclohexylurea precipitate with N-hydroxysuccinimide (NHS), (Figure 9). The N-hydroxysuccinimide-polymer ester was attacked by either the primary amino group of NTA.p or the secondary amino group of TrisNTA.p to give the desired polymer PB-PEO-SA-NTA.p (**10a**) or PB-PEO-SA-TrisNTA.p (**10b**), respectively (Figure 10).

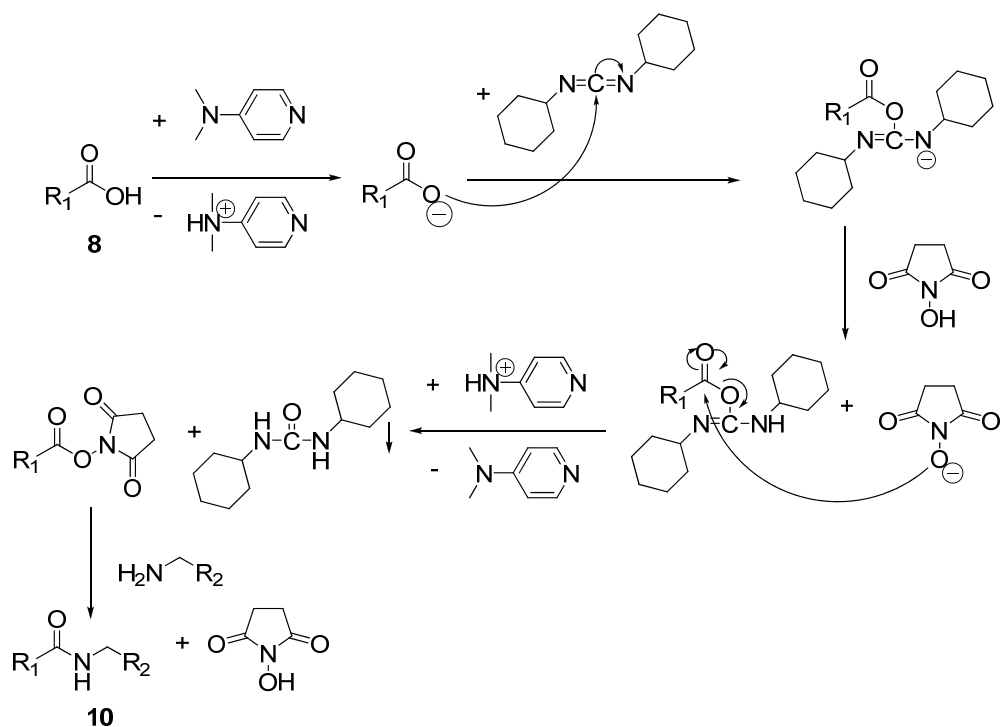


**Figure 9:** Mechanism of the amide coupling.

Schematically, the addition of NTA.p (**9a**) to the copolymer PB-PEO-SA-OH (**8**) is given in Figure 10. In the same manner the coupling of TrisNTA.p (**9b**) was performed.

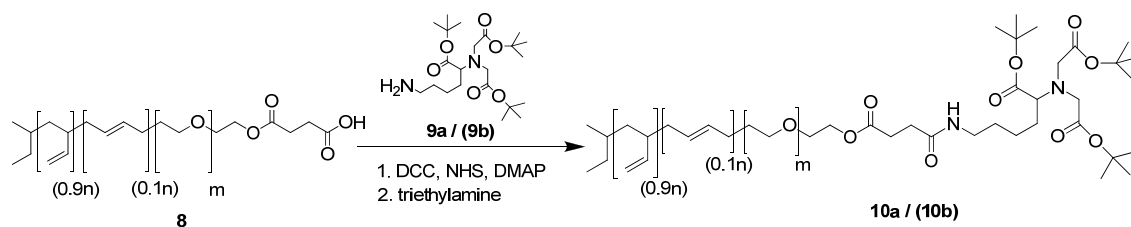


**Figure 10:** Synthesis of PB-PEO-SA-NTA.p via amide bond formation.

Deprotection of the carboxylic groups was performed by cleavage of the *tert*-butyl ester groups with trifluoroacetic acid (TFA) (isobutene was formed as result from elimination reaction).<sup>14</sup> The deprotection step of the NTA-group of copolymer **10a** is shown in Figure 11.

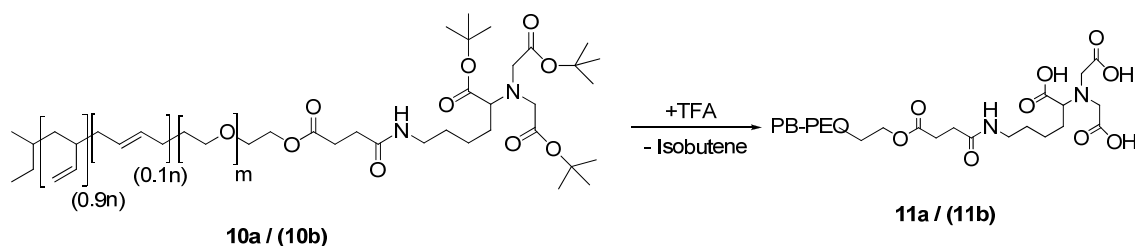


**Figure 11:** Deprotection off the NTA-tert.-butyl group with TFA.

The formation of metal-polymer complexes of  $\text{Ni}^{2+}$  and  $\text{Cu}^{2+}$  was performed by extraction of a copolymer solution containing N-methylmorpholine (NMM) with a  $\text{Ni}^{2+}$  or  $\text{Cu}^{2+}$  aqueous solution, see Figure 12.

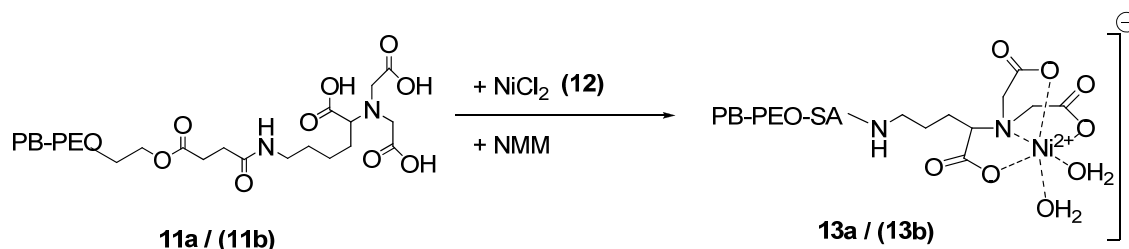


**Figure 12:** Formation of the metal-polymer complex.

## 2.2.2 The Anionic Polymerization Set up

As the anionic polymerization produces living ends that are very sensitive to air, a home made setup was developed to provide an inert atmosphere for all synthetic steps. The set up was made of HMP (high melting point) glass enabling a flame drying. As shown in Figure 13, the apparatus consists of two horizontal lines which provide the bulbs with argon or vacuum. The bulbs consist of fused upside-down, round bottomed HMP flasks which are connected to both the argon and the vacuum line via valves. Their openings (standard ground joint NS29) allow an easy connection of reaction flasks to the setup and simplifies distillation due to the wider surfaces of the NS29 grindings. The manometers  $p_1$  and  $p_2$  allow a control of argon or vacuum flow in the system. As every bulb is connected to the argon- and vacuum line with two separate valves the pressure (or vacuum) can be separately controlled for every reaction flask or ampule.

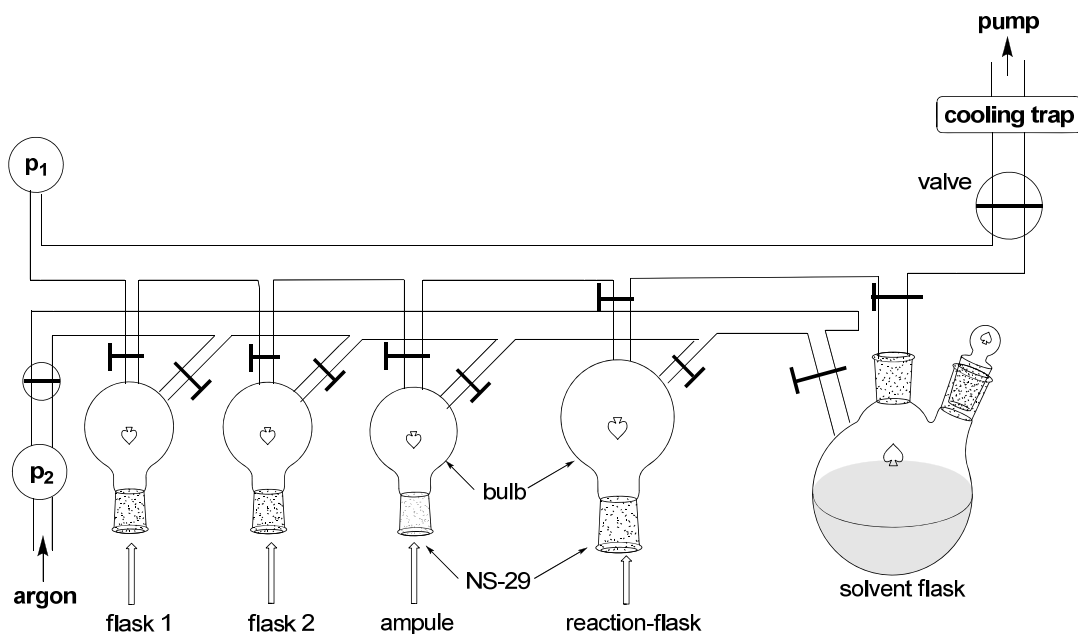


**Figure 13:** Scheme of the HMP glass home made anionic polymerization set up.

Figure 14 shows an image of the anionic polymerization set up as it is mounted in the hood. Beside the hood the pump unit is installed (Figure 14b); it consists of a 2021 SD rotary vane pump (Alcatel, France; **A**) connected to a ATP 150 turbo molecular pump (Alcatel, France; **B**) which is linked with the set up. The control unit for the turbo molecular pump is an ACT 600T Controller (Alcatel, France; **C**). In order to minimize leakage all connecting pieces were made as short as possible. The rotary vane pump provides the whole system with a vacuum of  $10^{-2}$  -  $10^{-3}$  mbar which is convenient for flame drying or solvent distillation. The turbo molecular pump generates a vacuum up to  $10^{-6}$  mbar which empowers the set up to handle extreme air- and moisture- sensitive chemicals.



**Figure 14:** a) The anionic polymerization setup;

b) the pump unit; **A** rotary pump, **B** turbo molecular pump, **C** controller

At the right end of the set up the solvent flask is connected; it contains the solvent. The deep purple color (benzophenon +Na/K) indicates that the solvent THF is moisture- and oxygen- free and it can be kept under these conditions for months.

### 2.2.3 Synthesis of the polymers and basic analysis

**Polymer Synthesis (general procedure).** All polymerization reactions were performed in flame-dried glassware in argon atmosphere using the home made polymerization setup described above.

#### 2.2.3.1 Polymer Synthesis and Characterization of the NTA diblock copolymer ( $\text{PB}_{60}\text{-PEO}_{34}\text{-SA-NTA.d-Ni}^{2+}$ ).

**Synthesis of poly(butadiene) ( $\text{PB}_{60}\text{-H}$ ) 3.** All glassware was flame dried. 17.4 mL of a 1.0 M solution of the phosphazene base *t*-BuP<sub>4</sub> (**4**, 17.4 mmol, 1.05 eq.) in hexane was introduced into the reactor (1 l) under a stream of argon. The hexane was distilled off, and the solid base was dried under vacuum for 30 minutes. 500 mL of dry THF were condensed into the reaction flask, stirred and then cooled down to -75°C. A 1.4 M solution of *s*-BuLi (**1**, 11.9 mL, 16.6 mmol, 1.0 eq.) in hexane was added via syringe. A yellow color appeared. Dry 1,3-Butadiene (**2**, 47.7 mL, 35.0 g, 0.647 mol, 39.0 eq.) was added to the reactor while keeping the temperature constant at -75°C. The reaction mixture was stirred for 12 hours at -78°C, a precursor was drawn from the reactor for analysis. The crude product was used *in situ* for the next step of the synthesis without any purification. GPC:  $M_n = 3256$  g/mol,  $M_w/M_n = 1.118$ .

$^1\text{H-NMR}$  (400 MHz,  $\text{CDCl}_3$ ,  $\delta/\text{ppm}$ ): 5.57 – 5.28 (m, 3H, 3, 6, 7), 4.97 – 4.85 (m, 2H, 4), 2.12 – 1.85 (m, 5H, 2, 5, 8), 1.25 – 1.06 (m, 2H, 1), Figure 15.  $^{13}\text{C-NMR}$  (100 MHz,  $\text{CDCl}_3$ ,  $\delta/\text{ppm}$ ): 143.6 (s, Ct, 3), 128.5 (s, Cs, 6 & 7), 114.3 (s, Cs, 4), 38.7 (s, Cs, 1), 38.5 (s, Ct, 2), 34.4 (s, Cs, 5).

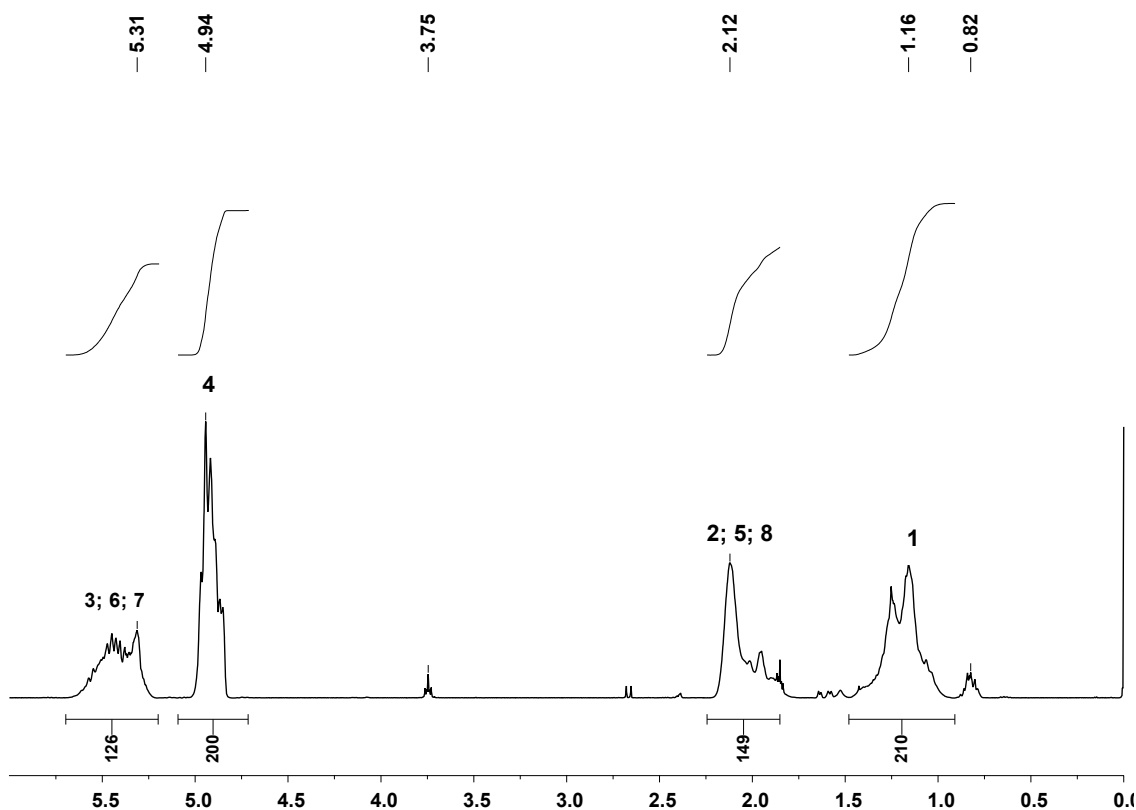


**Figure 15:**  $^1\text{H-NMR}$  of  $\text{PB}_{60}\text{-OH}$  (3)

**Synthesis of poly(butadiene)block-poly(ethylene oxide) ( $\text{PB}_{60}\text{-PEO}_{34}$ ) 6.** Ethylene oxide (**5**, 12.5 mL, 14.9 g, 0.34 mol, 20.3 eq.) was purified successively by distillation from  $\text{CaH}_2$ , sodium mirror and *n*-BuLi (2 mL) and then added to the reaction mixture containing the living poly(butadiene) carbanion at  $-60^\circ\text{C}$ . The color changed from yellow to colorless. After 1 hour at  $-60^\circ\text{C}$ , the solution was heated to  $40^\circ\text{C}$  and stirred for 4 days at this temperature. After one day, the solution turned into a deep blue. The product  $\text{PB}_{60}\text{-PEO}_{34}\text{-O}^-$  (**6**) was used in situ for the next step.

**Succinic Anhydride Functionalization of poly(butadiene)-block-poly (ethylene oxide) ( $\text{PB}_{60}\text{-PEO}_{34}\text{-SA-OH}$ ) 8.** The polymerization was quenched with a 1.0 M solution of succinic anhydride (**7**, 20 mL, 20.0 mmol, 1.42 eq.) in dry THF and afterwards 3 mL of

acetic acid were added. Two spatula tips of ion exchange resin Dowex 50WX4-100 were added and the solution was stirred for two hours. Afterwards the ion exchange resin was filtered off and most of the solvent was evaporated under reduced pressure until the reaction mixture became viscous. After precipitation in 3.0 l of cold ( $T = -94^{\circ}\text{C}$ ) acetone and drying under vacuum to constant weight, the polymer (**8**, 27.5 g, yield: 55 %) was obtained as a yellowish solid. GPC:  $M_n = 3898$  g/mol,  $M_w/M_n = 1.078$ .  $^1\text{H-NMR}$  (400 MHz,  $\text{CDCl}_3$ ,  $\delta/\text{ppm}$ ): 5.57 – 5.28 (m, 3H, 3, 6, 7), 4.97 – 4.85 (m, 2H, 4), 4.25 (t,  $^3J_{\text{HH}} = 4.6$  Hz, 2H, 12), 3.82 (t,  $^3J_{\text{HH}} = 4.5$  Hz, 2H, 11), 3.74 – 3.64 (m, 2H, 9, 10), 2.64 (m, 4H, 13, 14), 2.12 – 1.85 (m, 5H, 2, 5, 8), 1.25 – 1.06 (m, 2H, 1), Figure 17.

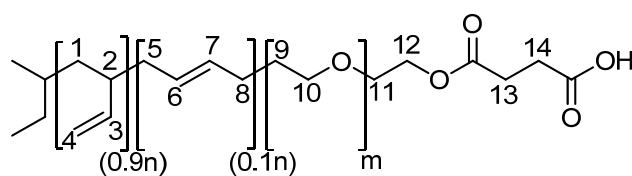


**Figure 16:**  $\text{PB}_{60}\text{-PEO}_{34}\text{-SA-OH}$  (**8**)

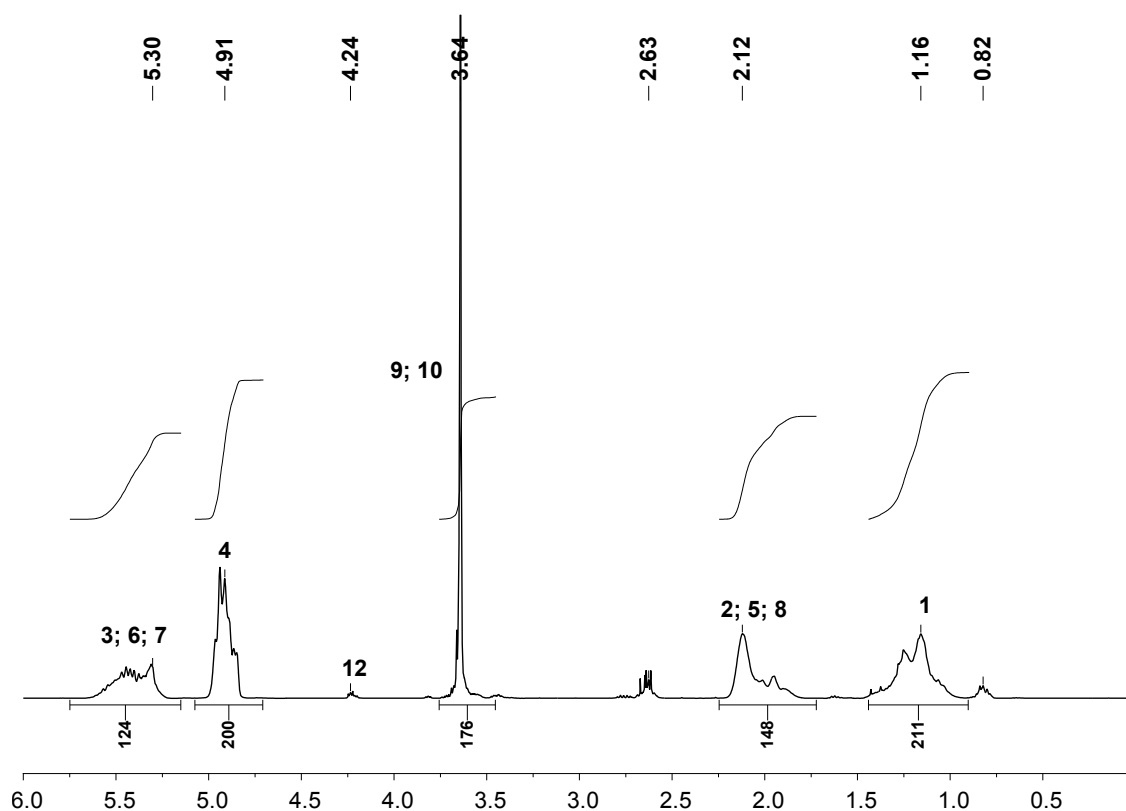


**Figure 17:**  $^1\text{H-NMR}$  of  $\text{PB}_{60}\text{-PEO}_{34}\text{-SA-OH}$  (**8**)

**NTA-functionalization PB<sub>60</sub>-PEO<sub>34</sub>-SA-NTA.p 10a.** PB<sub>60</sub>-PEO<sub>34</sub>-SA-OH (**8**, 8.99 g, 2.09 mmol, 1.0 eq.) was added into a 500 mL round-bottomed flask. The polymer was dissolved in 100 mL dichloromethane. To the polymer solution a solution of dicyclohexylcarbodiimide (431 mg, 2.09 mmol, 1.0 eq.), N-hydroxysuccinimide (241 mg, 2.09 mmol, 1.0 eq) and 4-(dimethylamino)pyridine (29 mg, 0.24 mmol, 0.11 eq.) in 20 mL dichloromethane was added. After 12 hours of stirring at room temperature under dark conditions, the precipitated urea was filtered off and a solution of NTA.p (**9a**, 0.90 g, 2.09 mmol, 1.0 eq.) and triethylamine (800  $\mu$ l) in 20 mL of dichloromethane was added to the polymer solution. The reaction mixture was stirred for 5 hours at room temperature in the dark. Afterwards the solvent was removed under reduced pressure and the polymer was used in the next step without any purification. GPC:  $M_n = 3171$  g/mol,  $M_w/M_n = 1.129$ . <sup>1</sup>H-NMR (400 MHz, CDCl<sub>3</sub>,  $\delta$ /ppm): 5.57 – 5.28 (m, 3H, 3, 6, 7), 4.97 – 4.85 (m, 2H, 4), 4.24 – 4.20 (m, 12), 3.82 (m, 2H, 11), 3.74 – 3.61 (m, 2H, 9, 10), 3.44 (d, <sup>3</sup>J<sub>HH</sub> = 8.0 Hz, 1H, 19), 3.32 – 3.28 (m, 2H, 15), 2.78 - 2.60 (m, 4H, 13, 14), 2.12 – 1.85 (m, 11H, 2, 5, 8, 16, 17, 18), 1.45 (s, 27H, 21), 1.30 – 1.06 (m, 2H, 1), Figure 19. <sup>13</sup>C-NMR (100 MHz, CDCl<sub>3</sub>,  $\delta$ /ppm): 143.2 (s, Ct, 3), 113.8 (s, Cs, 4), 70.6 (s, Cs, 9, 10), 38.6 (s, Cs, 1), 38.5 (s, Ct, 2), 28.1 (NTA.p, *tert*-Bu, 21).

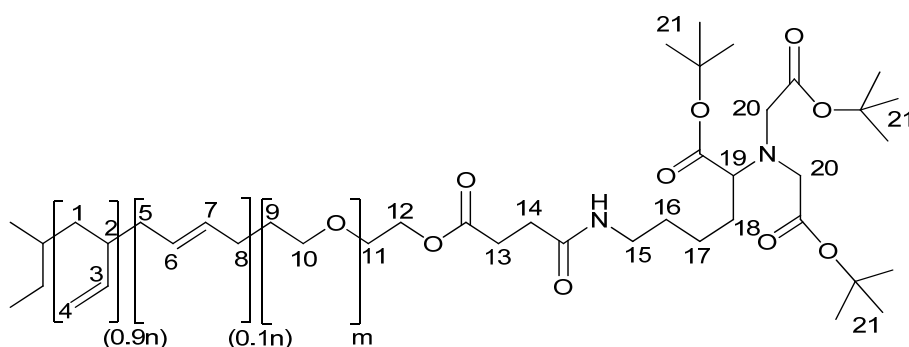


**Figure 18:** PB<sub>60</sub>-PEO<sub>34</sub>-SA-NTA.p (10a)

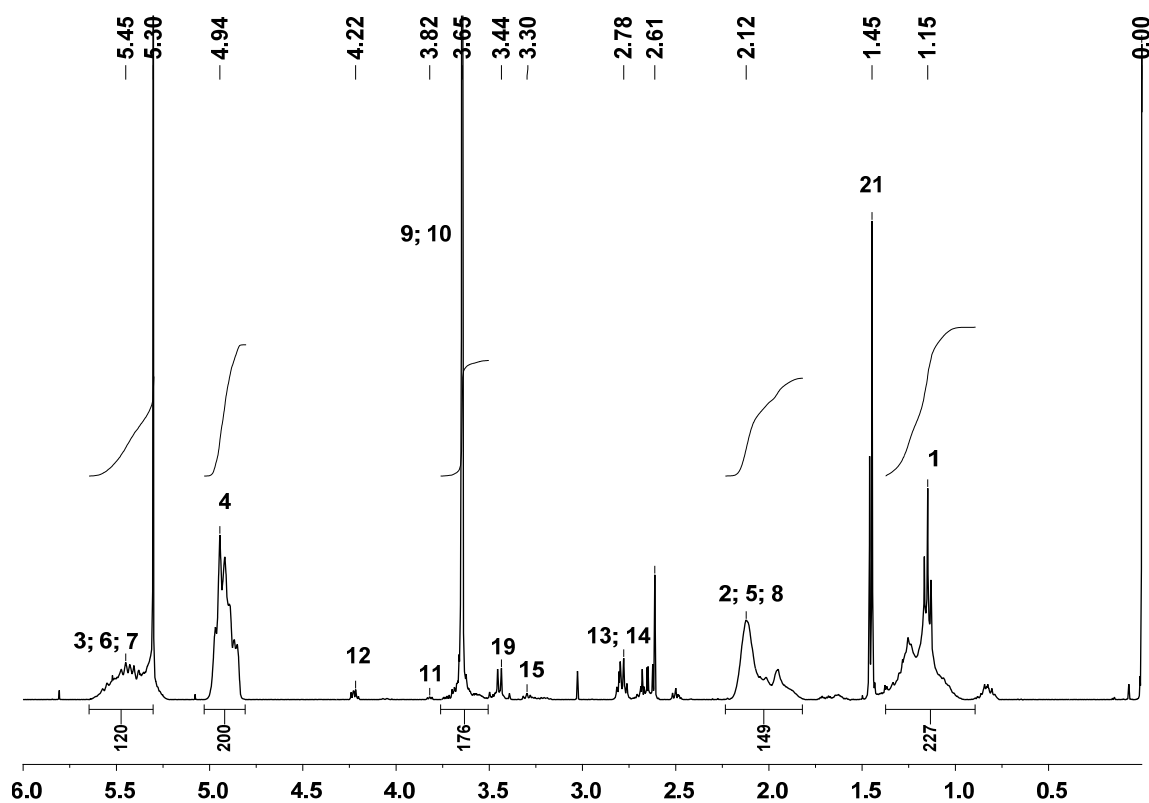


**Figure 19:**  $^1\text{H-NMR}$  of  $\text{PB}_{60}\text{-PEO}_{34}\text{-SA-NTA.p.}$  (10a)

**Deprotection of  $\text{PB}_{60}\text{-PEO}_{34}\text{-SA-NTA.p}$  **11a**.** The functionalized polymer was dissolved in 40 mL chloroform and a mixture of 65 mL chloroform and 15 mL trifluoroacetic acid was added. After stirring for 24 hours in the dark at room temperature, the solvent and most of the trifluoroacetic acid were removed under vacuum. The obtained solid was washed with aqueous sodium hydroxide solution (1 M, 20 mL) and water (20 mL). It was precipitated in cold methanol (50 mL) and filtered. The polymer was dissolved in chloroform (400 mL) and dried over sodium sulphate. After evaporating the solvent and drying under vacuum the desired product **11a** (3.18 g, yield: 33 %) was obtained as a yellow viscous mass. GPC:  $M_n = 3667$  g/mol,  $M_w/M_n = 1.116$ .  $^1\text{H-NMR}$  (400 MHz,  $\text{CDCl}_3$ ,  $\delta/\text{ppm}$ ): 5.57 – 5.28 (m, 3H, 3, 6, 7), 4.97 – 4.85 (m, 2H, 4), 4.26 – 4.23 (m, 12), 3.81 (m, 2H, 11), 3.74 – 3.61 (m, 2H, 9, 10), 3.46 (m, 1H, 19), 3.37 (m, 2H, 15), 2.74 - 2.64 (m, 4H, 13, 14), 2.12 – 1.85 (m, 11H, 2, 5, 8, 16, 17, 18), 1.30 – 1.06 (m, 2H, 1), Figure 21.

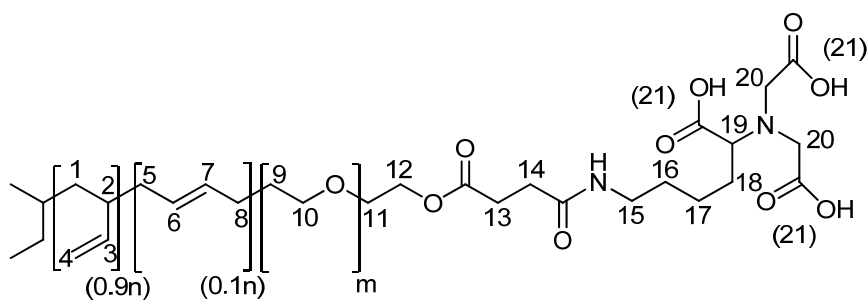


Figure 20: PB<sub>60</sub>-PEO<sub>34</sub>-SA-NTA.d (11a)

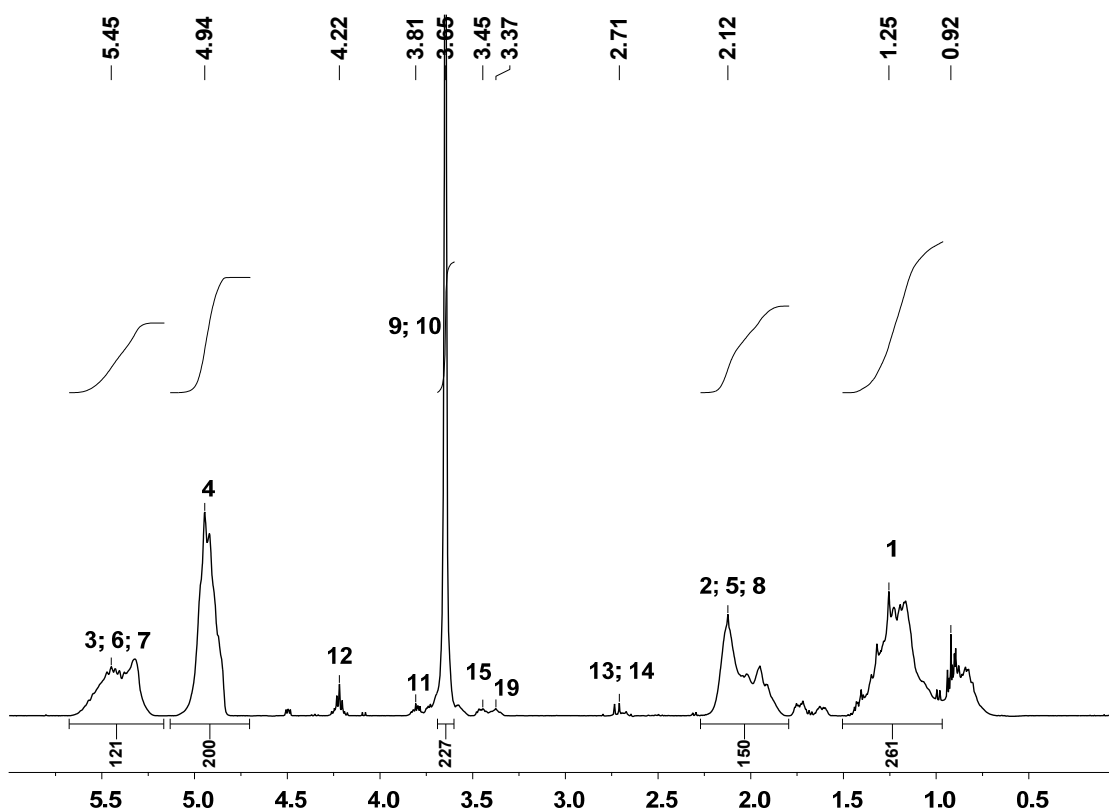


Figure 21: <sup>1</sup>H-NMR of PB<sub>60</sub>-PEO<sub>34</sub>-SA-NTA.d (11a)

**PB<sub>60</sub>-PEO<sub>34</sub>-SA-NTA.d + NiCl<sub>2</sub> / Cu(TFA)<sub>2</sub> 13a.** For complexing Ni<sup>2+</sup> ions/Cu<sup>2+</sup> ions (12) with the block copolymer-NTA.d (11a), 10 mL of a 5 mM solution of polymer in CHCl<sub>3</sub> and 15 mL of 20 mM NiCl<sub>2</sub> or 15 mL of a 10 mM Cu(TFA)<sub>2</sub> (12) in 200 mM TRIS/HCl pH = 8.4 solution were mixed and stirred over night at 25°C. The water phase was removed and the chloroform phase was washed once with the TRIS-buffer. The solvent was removed via rotary evaporator. The greenish polymer (13a) was dried in vacuum over night at room temperature.

---

### 2.2.3.2 Polymer Synthesis and Characterization of the TrisNTA diblock copolymer (PB<sub>39</sub>-PEO<sub>36</sub>-SA-Tris.NTA.d-Ni<sup>2+</sup>)

**Synthesis of poly(butadiene) (PB<sub>39</sub>-H) 3.** All glassware was flame dried. 2.5 mL of a 1.0 M solution of the phosphazene base *t*-BuP<sub>4</sub> (**4**, 2.50 mmol, 0.9 eq.) in hexane was introduced into the reactor (1 l) against argon stream. The hexane was distilled off, and the solid base was dried under vacuum for 30 minutes. 200 mL of dry THF were condensed into the reaction flask and then cooled down to -80 °C. A 1.4 M solution of *s*-BuLi (**1**, 2.00 mL, 2.80 mmol, 1.0 eq.) in hexane was added via syringe. A yellow color appeared. Dry 1,3-Butadiene (**2**, 8.10 mL, 5.94 g, 110 mmol, 39.3 eq.) was added to the reactor while keeping the temperature constant at -80°C. The reaction mixture was stirred for 12 hours at -80°C and a precursor was drawn from the reactor for analysis. The crude product was used *in situ* for the next step of the synthesis without any purification. GPC: M<sub>n</sub> = 2123 g/mol, M<sub>w</sub>/M<sub>n</sub> = 1.083. <sup>1</sup>H-NMR (400 MHz, CDCl<sub>3</sub>, δ/ppm): 5.57 – 5.28 (m, 3H, 3, 6, 7), 4.97 – 4.85 (m, 2H, 4), 2.12 – 1.85 (m, 5H, 2, 5, 8), 1.25 – 1.06 (m, 2H, 1). <sup>13</sup>C-NMR (100 MHz, CDCl<sub>3</sub>, δ/ppm): 143.6 (s, Ct, 3), 128.5 (s, Cs, 6 & 7), 114.3 (s, Cs, 4), 38.7 (s, Cs, 1), 38.5 (s, Ct, 2), 34.4 (s, Cs, 5).

**Synthesis of poly(butadiene)-block-poly(ethylene oxide) (PB<sub>39</sub>-PEO<sub>36</sub>) 6.** Ethylene oxide (**5**, 2.10 mL, 2.07 g, 47 mmol, 16.8 eq.) was purified successively by distillation from CaH<sub>2</sub>, sodium mirror and *n*-BuLi (2 mL) and then added to the reaction mixture containing poly(butadiene) (**3**) at -60°C. The color changed from yellow to colorless. After 1 hour at -60°C, the solution was heated to 40°C and stirred for 4 days at this temperature. After one day, the solution turned into a deep blue. The product PB<sub>39</sub>-PEO<sub>36</sub> (**6**) was used *in situ* for the next step.

**Succinic Anhydride Functionalization of poly(butadiene)-block-poly(ethylene oxide) (PB<sub>39</sub>-PEO<sub>36</sub>-SA-OH) 8.** The polymerization was quenched with a 0.30 M solution of succinic anhydride (**7**, 20 mL, 6.00 mmol, 2.10 eq.) in THF and afterwards 3 mL of acetic acid were added. Two spatula tips of ion exchange resin (Dowex 50WX4-100, USA) were added. The solution was stirred for two hours. Then the ion exchange resin was filtered off and most of the solvent was evaporated under reduced pressure until the reaction mixture became viscous. After precipitation in 1.5 l of cold (T = -94°C) acetone and drying under vacuum to constant weight, the polymer (**8**, 5.63 g, yield: 66 %) was obtained as a yellow solid. GPC: M<sub>n</sub> = 3437 g/mol, M<sub>w</sub>/M<sub>n</sub> = 1.077. <sup>1</sup>H-NMR (400 MHz, CDCl<sub>3</sub>, δ/ppm): 5.57 – 5.28 (m, 3H, 3, 6, 7), 4.97 – 4.85 (m, 2H, 4), 4.25 (t, <sup>3</sup>J<sub>HH</sub> = 4.6 Hz, 2H, 12), 3.82 (t, <sup>3</sup>J<sub>HH</sub> = 4.5 Hz, 2H, 11), 3.74 – 3.64 (m, 2H, 9, 10), 2.64 (m, 4H, 13, 14), 2.12 – 1.85 (m, 5H, 2, 5, 8), 1.25 – 1.06 (m, 2H, 1).

**Synthesis of PB<sub>39</sub>-PEO<sub>36</sub>-SA-TrisNTA.p 10b.** PB<sub>39</sub>-PEO<sub>36</sub>-SA-OH (**8**, 3.53 g, 1.00 mmol, 1.0 eq.) was introduced into a 500 mL round-bottomed flask. The polymer was dissolved in 40 mL dichloromethane. A solution of dicyclohexylcarbodiimide (206 mg, 1.00 mmol, 1.0 eq.), N-hydroxysuccinimide (115 mg, 1.00 mmol, 1.0 eq.) and 4-(dimethylamino)pyridine (15 mg, 0.12 mmol, 0.12 eq.) in 40 mL dichloromethane was added to the polymer solution. After 12 hours of stirring at room temperature in dark, the precipitated urea was filtered off and a solution of TrisNTA.p (**9b**, 0.50 g, 0.347 mmol, 0.35 eq.) and triethylamine (400  $\mu$ l) in 60 mL of dichloromethane was added. The reaction mixture was stirred for 24 hours at room temperature in dark. The polymer solution was concentrated under reduced pressure and precipitated in cold methanol (1 L). The obtained product was dried under vacuum. <sup>1</sup>H-NMR (400 MHz, CDCl<sub>3</sub>,  $\delta$ /ppm): 5.57 – 5.28 (m, 3H, 3, 6, 7), 4.97 – 4.85 (m, 2H, 4), 4.29 (m, TrisNTA.p), 4.28 – 4.25 (m, 2H, 12), 3.82 (m, 2H, 11), 3.74 – 3.64 (m, 2H, 9, 10), 3.42 (m, TrisNTA.p), 3.02 - 2.62 (m, TrisNTA.p), 2.62 (m, 4H, 13, 14), 2.12 – 1.85 (m, 5H, 2, 5, 8), 1.43 – 1.46 (m, *tert*-Bu, 15), 1.25 – 1.06 (m, 2H, 1), Figure 22. <sup>13</sup>C-NMR (100 MHz, CDCl<sub>3</sub>,  $\delta$ /ppm): 143.2 (s, Ct, 3), 114.3 (s, Cs, 4), 70.5 (s, Cs, 9, 10), 38.7 (s, Cs, 1), 38.5 (s, Ct, 2), 28.2 (*tert*-Bu, 15).

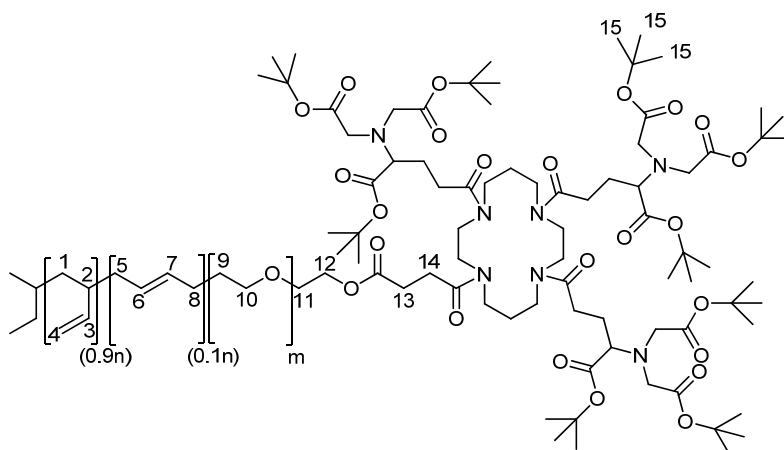


**Figure 22:** PB<sub>39</sub>-PEO<sub>36</sub>-SA-NTA.p (10b)

**Deprotection of PB<sub>39</sub>-PEO<sub>36</sub>-SA-TrisNTA.p 11b.** The functionalized polymer **10b** was dissolved in 40 mL chloroform. To the polymer solution a mixture of 20 mL trifluoroacetic acid and 40 mL chloroform was added. The reaction mixture was stirred for 24 hours at room temperature in the dark. After evaporating of the solvent and the trifluoroacetic acid under vacuum the crude product was washed with a 1M aqueous solution of sodium hydroxide (2 $\times$  10 mL) and water (2 $\times$  10 mL). The last aqueous phase was extracted (4 $\times$  100 mL) with CHCl<sub>3</sub> and the combined organic layers were dried over sodium sulfate. The solvent was evaporated under vacuum. The deprotected diblock copolymer (**11b**, 2.40 g,

yield: 62 %) was obtained as a yellow viscous liquid. GPC:  $M_n = 3171$  g/mol,  $M_w/M_n = 1.129$ .  $^1\text{H-NMR}$  (400 MHz,  $\text{CDCl}_3$ ,  $\delta/\text{ppm}$ ): 5.57 – 5.28 (m, 3H, 3, 6, 7), 4.97 – 4.85 (m, 2H, 4), 4.29 (m, TrisNTA.d), 4.27 – 4.25 (m, 2H, 12), 3.82 (m, 2H, 11), 3.74 – 3.64 (m, 2H, 9, 10), 3.44 (m, TrisNTA.d), 2.65 (m, 4H, 13, 14), 2.12 – 1.85 (m, 5H, 2, 5, 8), 1.43 (s, TrisNTA.p, *tert*-Bu, 15; residual peak), 1.25 – 1.07 (m, 2H, 1), Figure 24.

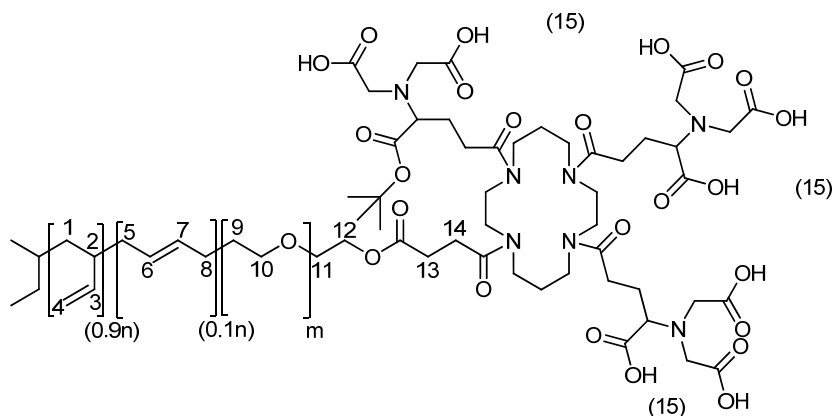


**Figure 23:** PB<sub>39</sub>-PEO<sub>36</sub>-SA-NTA.d (11b)

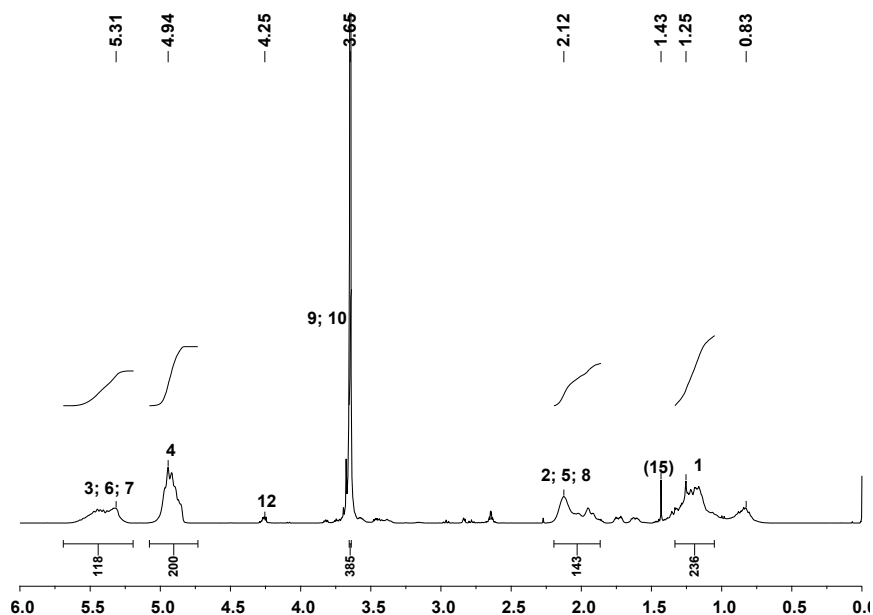


**Figure 24:**  $^1\text{H-NMR}$  of PB<sub>39</sub>-PEO<sub>36</sub>-SA-NTA.d (11b)

**PB<sub>39</sub>-PEO<sub>36</sub>-SA-TrisNTA.d + NiCl<sub>2</sub> / Cu(TFA)<sub>2</sub> 13b.** For complexing Ni<sup>2+</sup> ions/Cu<sup>2+</sup> ions (12) with the block copolymer-NTA.d, a 0.30 mM solution of polymer in  $\text{CHCl}_3/\text{MeOH}$  (10:1) and a 15 mM NiCl<sub>2</sub> or Cu(TFA)<sub>2</sub> (12) in 200 mM TRIS/HCl pH = 8.4 solution were mixed and stirred over night at 25°C. The water phase was removed and the chloroform phase was

washed once with 10 mL of TRIS-buffer. The solvent was removed via rotary evaporator. The greenish polymer (**13b**) was dried in vacuum over night at room temperature.

**List of diblock copolymers.** All synthesized diblock copolymers with their characteristics are shown in Table 1. Size Exclusion Chromatography (SEC) was performed in THF and  $^1\text{H-NMR}$  was performed in  $\text{CDCl}_3$ . The degree of polymerization was calculated from the monomer/initiator ratio ( $N_{\text{calc}}$ ).  $N_n$  of the poly(butadiene)-precursor was determined by SEC in THF and calibrated by narrow ( $M_w/M_n < 1.2$ ) PB-standards (Poly(butadiene-1.2); Polymer Standards Service (PSS), Mainz, Germany).  $N_n$  of the PEO block is calculated based on the PB/PEO ratios in the  $^1\text{H-NMR}$ .  $M_w/M_n$  of the diblock was also performed via SEC in THF.  $M_n$  of the diblock copolymers PB-PEO was calculated from the  $N_n$  values given from SEC (PB) and  $^1\text{H-NMR}$  (PEO) respectively.

**Table 1:** List of all synthesized diblock copolymers

sample-ID	calc.	SEC	SEC	calc.	NMR	SEC	NMR	SEC/ NMR
	$N_n$ (PB)	$N_n$ (PB)	$M_w/M_n$ (PB)	$N_n$ (PEO)	$N_n$ (PEO)	$M_w/M_n$ (block)	ratio PB 1.2/ 1.4	$M_n$ (Block)
<b>PB<sub>84</sub>-PEO<sub>110</sub>-OH</b>	85	84	1,039	68	110	1,083	0.9/ 0.1	9450
<b>PB<sub>200</sub>-PEO<sub>58</sub>-SA-OH</b>	100	200	1,095	45	58	1,122	0.9/ 0.1	9400
<b>PB<sub>200</sub>-PEO<sub>68</sub>-SA-NTA.d.</b>	100	200	1,095	45	68	1,122	0.9/ 0.1	8800
<b>PB<sub>112</sub>-PEO<sub>45</sub>-SA-OH</b>	80	112	1,043	33	45	1,028	0.9/ 0.1	6634
<b>PB<sub>112</sub>-PEO<sub>45</sub>-SA-NTA.d.</b>	80	112	1,043	33	45	1,051	0.9/ 0.1	6634
<b>PB<sub>60</sub>-PEO<sub>24</sub>-SA-OH</b>	46	60	1,118	24	24	1,078	0.9/ 0.1	4313
<b>PB<sub>60</sub>-PEO<sub>34</sub>-SA-NTA.d</b>	46	60	1,118	24	34	1,116	0.9/ 0.1	4754
<b>PB<sub>39</sub>-PEO<sub>32</sub>-SA-OH</b>	46	39	1,083	24	32	1,077	0.9/ 0.1	3532
<b>PB<sub>39</sub>-PEO<sub>36</sub>-SA-Tris-NTA.d</b>	46	39	1,083	24	36	1,129	0.9/ 0.1	3695

---

## 2.3 Polymer Characterization Methods

**Nuclear Magnetic Resonance (NMR).** NMR spectroscopy is one of the principal techniques used to obtain structural information about molecules due to the chemical shift and Zeeman effect on the resonant frequencies of the nuclei. NMR studies the magnetic nuclei by aligning them with an applied constant magnetic field and perturbing them using an alternating orthogonal magnetic field. <sup>1</sup>H-NMR-spectroscopy is the most commonly used technique which gives narrow chemical shifts, but sharp signals.

<sup>1</sup>H-NMR spectra were recorded with a Varian Unity 400 NMR spectrometer in CDCl<sub>3</sub> (99.8% D, 0.1% TMS, Aldrich) at RT. The signals were referenced to that of TMS at  $\delta = 0.00$  ppm. The spectrometer was operated at 400 MHz with a sweep width of 8278.146 Hz and 22° pulse width of 2.96  $\mu$ s.

**Heteronuclear multiple bond correlation (hmbc):** all NMR experiments were performed at 22°C on a Bruker DRX-600 NMR spectrometer in CDCl<sub>3</sub> (99.8% D, 0.1% TMS, Aldrich), equipped with a z-axis pulsed field gradient dual broadband inverse probehead. Chemical shifts were referenced to residual solvent peaks and the temperature was calibrated using a methanol sample. Heteronuclear multiple bond correlation (hmbc) experiments were performed with 1024 time points in F2 and 512 time increments in the indirect dimension F1. The total experimental time was 10.5 hours.

**Size Exclusion Chromatography (SEC).** SEC is a relative analytical and chromatographic method in which particles are separated based on their size. This technique is usually applied to macromolecules such as polymers or proteins. The name gel permeation chromatography GPC is used when an organic solvent is applied as the mobile phase. GPC can be used as a measure of both the size and the polydispersity  $M_w/M_n$  of a polymer. If polymer standards of a known size are eluted through the column, a calibration curve can be created to determine the sizes of the polymer molecules of interest.

Thermo Separation Product set-ups equipped with UV and RI detectors (Agilent 1100 Series) were used. The column set was an Agilent PLgel 10  $\mu$ m Guard, 50\*7.5 mm and two Agilent PLgel 300\*7.5 mm 10  $\mu$ m 100 Å and 5  $\mu$ m 1000 Å. Analyses were performed at 40°C with THF, at a flow rate of 1.0 mL/min. Poly(1,2-butadiene) standards (PSS GmbH, Mainz, Germany) with narrow weight distribution were used for calibration. The poly(butadiene) standards were in the same range of magnitude as the poly(butadiene) precursors.

**Ultraviolet/ Visible Spectroscopy (UV/VIS).** NiCl<sub>2</sub> (Cu(TFA)<sub>2</sub>) dissolves in water with a green (blue) color whereas the functionalized diblock copolymers dissolve in chloroform

---

with a yellowish color. The phases (nickel in water and polymer in chloroform) were mixed and stirred vigorously overnight. The two phases were separated by centrifugation and the polymer phase changed its color from yellowish to green, showing that the hydrophilic Ni<sup>2+</sup> ion was uptaken from the hydrophobic polymer solution. The polymer solution kept its greenish color after drying with sodium sulfate, indicating that a complexation of the NTA.d group with nickel (II) has occurred.

The UV/VIS spectra were recorded with a Perkin Elmer Lambda 35 UV/VIS spectrometer ( $\lambda = 200 - 800$  nm), in silica glass cells, at 25°C. Polymer solutions ( $c = 2 \times 10^{-3}$  mol/l) were prepared in chloroform.

**Electron Paramagnetic Resonance (EPR).** EPR is a powerful method for studying magnetic properties and crystal-field symmetry of species containing unpaired electrons, such as copper (II) complexes. Copper was used as complexing metal, due to its capability to coordinate fast to nearly all kinds of organic ligands. It is an ideal metal to investigate interactions with various ligands, since it can adopt a large variety of geometries (e.g. square-planar, tetrahedral, pyramidal, trigonal bipyramidal), to which its spin Hamiltonian is very sensitive.<sup>106</sup> The basic physical concept of EPR is analogous to NMR, but instead of nuclei spins, unpaired electrons are irradiated with microwave energy. The electron's magnetic moment aligns itself either parallel or antiparallel to an external magnetic field, with a specific energy for each alignment. The energy levels split proportionally to the magnetic field's strength. An unpaired electron can change between the two energy levels by absorbing microwave energy. Due to Maxwell-Boltzmann distribution, there are more electrons in the lower energetic level than in the upper level. Therefore a total net absorption can be detected. EPR spectra are usually presented as first derivative of the absorbance. Due to the charge distribution in the molecular system, the unpaired electron is placed in the magnetic external field and an additional magnetic field due to the nuclei (Zeeman electronic effect). If the unpaired electron is located nearby nuclei with  $I \neq 0$  will interact with the nucleus' magnetic moment. This leads to the splitting of the EPR resonance signal, and is called hyperfine interaction.

Electron paramagnetic resonance (EPR) spectra were recorded at low temperatures (130 K and 77 K) with a CW Bruker ElexSys500 X-band spectrometer, equipped with a Helium temperature control system ER4112HV to which the wave-guide resonant cavity was mounted. 2 mW microwave power was used for all measurements. The modulation frequency was 100 kHz and the modulation amplitude was 0.5 mT; other spectral parameters were adjusted for each spectrum individually. Multiple spectra were acquired to optimize the signal-to-noise ratio, and 3<sup>rd</sup>-order polynomial averaging was used for

---

subsequent noise reduction. The spectral parameters were obtained with the SIMFONIA software package (Bruker Instruments Inc., Manning Park, Billerica, MA), where co-axial g and hyperfine tensors were assumed. Gaussian line shapes were assumed with the line-width adjusted for each spectrum. All spectral simulations assumed natural abundance ratios of Cu isotopes. The g-values were referenced to diphenylpicrylhydrazyl (DPPH) (g = 2.0036) as an external standard.

## 2.4 Vesicle Formation

Vesicles are classified by their size. “SUVs” (small unilamellar vesicles) have diameters in the range of nanometers. Giant unilamellar vesicles (GUVs) vary in diameter from 10 to 200  $\mu\text{m}$ . GUVs are more suitable for microscopy investigations, e.g. the damage and repair of a membrane, as they are easily visualized by optical microscopy.<sup>107</sup> To obtain GUVs, two techniques were used:

- Electroformation
- Film rehydration.

On the other hand only SUVs are suitable for scattering experiments like SAXS-, DLS- & SLS- and FCS- measurements. To obtain a homogeneous solution of small unilamellar vesicles a combination of two techniques was used:

- Film rehydration + Electroformation.

Vesicles were formed either with PB-PEO-SA-OH (**8**) or with a mixture containing 10% NTA.d-metal functionalized polymer PB-PEO-SA-OH/0.1PB-PEO-NTA.d-metal (**13**).

### 2.4.1 Electroformation

Giant vesicles were made via electroformation in bidistilled water in a home-made set up. The electroformation of vesicles was invented by Angelova and Dimitrov<sup>108</sup> in 1986. The mechanism of the vesicle electroformation in an AC field has not been fully established. However, the electroosmotic flow of water as main driving force has been widely accepted. This electroosmotic flow creates an oscillating density gradient in a direction perpendicular to the electrodes. Since the growing vesicles were observed to vibrate at the same frequency as the applied field, also the electric field may serve to create a gentle mechanical agitation that assists in the formation of vesicles.

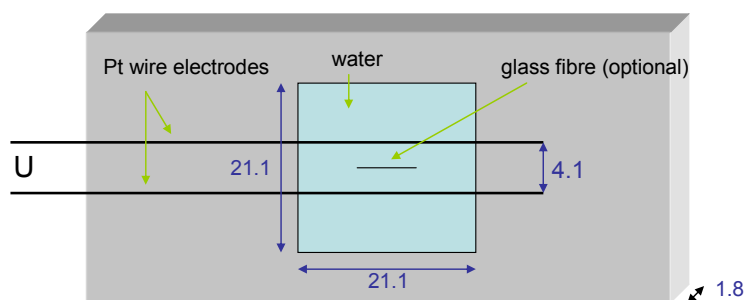
The set up consists of a glass cell with two platinum electrodes in parallel, Figure 25. Each electrode has a diameter of 1 mm. The cell can be filled with aqueous solution. Between the electrodes an alternating current with a low frequency (1Hz to 10 Hz) is

---

conducted. The polymer is placed on the platinum electrodes or on the surface of a glass fiber adjusted between the two electrodes. Application of alternating current (AC) voltage leads to the formation of vesicles.

To place the polymer on the electrode, the near end of the electrode was drop-coated with polymer solution ( $c = 10 \text{ mg/mL}$ ) in chloroform. The Pt wire was held so that the fall of the drops along the wire spread over the surface to form a thin polymer film. The covered electrodes were dried in vacuum to remove traces of chloroform. Afterwards the electrodes were put into bidistilled water for one hour to let the hydrophilic chains swell. Then the electrodes were fitted into the cell and covered with bidistilled water or buffer.

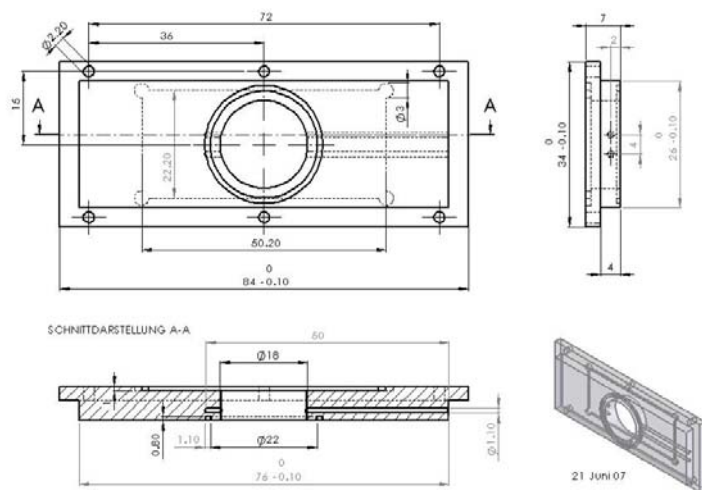
In Figure 25 the schematic draft of the electroformation set up is shown. Alternatively one can mount a glass fiber between the two platinum electrodes coated with a polymer or lipid film. The alternating voltage between the Pt electrodes is  $\tilde{U} = 2\text{V}$  to  $10\text{V}$  (average). The platinum electrodes were connected to a function generator (GFG-8215 A from GW Instek, USA) to apply the recommended voltage and frequency.<sup>107</sup>



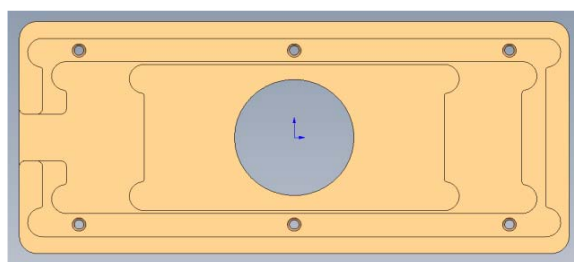
**Figure 25:** Top view of the electroformation cell. The sizes are in millimeters.

Figure 26 shows the home made glass cell which was made by Hellma Schweiz AG (Hellma-draft 665.760) and Figure 27 shows the nonconductive aluminium frame for the glass cell made by the workshop Department Chemie Universität Basel, Switzerland.

The latter embeds the glass slide beneath the glass cell. The glass cell is fixed onto the glass slight by tightening it into the aluminium frame with six screws.



**Figure 26:** The home made glass cell for the electroformation.



**Figure 27:** The home made aluminium frame for the glass cell.

## 2.4.2 Rehydration

Vesicles were generated via rehydration with Milli-Q water, bidistilled water or buffer in a 100 mL round-bottom flask. In order to form vesicles by film rehydration the polymer was dissolved in chloroform in a round-bottomed flask. The solvent was evaporated under reduced pressure, so that a thin polymer film was formed on the inner glass surface of the flask. The polymer film was hydrated with Milli-Q water, bidistilled water or buffer to give a concentration of 5  $\mu\text{M}$  up to 2 mM while the flask was rotated (25 rotations per minute) at room temperature under atmospheric pressure over night. The surface areas covered with polymer film (50 mL to 250 mL round bottomed flasks) and the calculated concentrations of

---

vesicles (5  $\mu\text{M}$  up to 2 mM) varied. The technique of rehydration is simple in comparison to the technique of electroformation and requires no special equipment.

### **2.4.3 Extrusion**

In order to remove the polymer flakes and to obtain homogeneous in size vesicles, the solutions from rehydration were successively filtered through 10  $\mu\text{m}$  and 1  $\mu\text{m}$  polycarbonate membranes. Afterwards the solutions were extruded through a polycarbonate membrane (11 $\times$ ) with a convenient cut-off diameter (nuclepore track-etch membrane, 0.08  $\mu\text{m}$  – 10  $\mu\text{m}$  cut-off diameter, Whatman, UK) by a LIPEX™ 10 mL Thermobarrel Extruder (Northern Lipids Inc., USA) or a miniextruder (Avanti lipids, AL, USA).

## **2.5 Vesicle Characterization Methods**

### **2.5.1 Optical Microscopy (OM)**

Optical microscope is an appropriate tool to check the morphology of giant vesicles and other self-aggregates. Also the formation of giant vesicles via electroformation can be observed isochronously by optical microscopy.

Vesicle dispersions in bi-distilled water and buffers were examined with a transmission Microscope DMIRE2 (Leica), at a magnification of 20 $\times$ 10 and 100 $\times$ 10 (oil immersion objective) with phase contrast Ph1 to better visualize the vesicles. Images were taken with a Leica DC camera (350 FX, Leica, Germany) with a software Leica IM 500 (Version 4.0 Release 132, Leica Microsystems Imaging Solution Ltd., UK).

### **2.5.2 Transmission Electron Microscopy (TEM)**

The TEM enables to look at vesicular structures with a much higher magnification and resolution. Drops of vesicle dispersions were deposited on graphite coated grids (Square 300 Mesh Copper Grids from Veco) and let them adsorb for 1 minute. The samples were then incubated in a 2% uranyl acetate solution for negative staining. Images were taken with a Philips CM-100 TEM, 80 kV equipped with a CCD camera.

### **2.5.3 Cryo-Transmission Electron Microscopy**

To visualize intact vesicles Cryo-TEM is the method of choice. Although not easy to handle, this technique provides precise vesicle images, and even the thickness of the membrane can be estimated. To use this technique the sample has to be frozen very fast in

its aqueous environment. A fast freezing procedure is necessary because only rapidly frozen water is amorphous. In contrast to amorphous ice, crystalline ice destroys the vesicles and is not permeable for the electron beam.

For embedding the sample in amorphous ice, the vesicle solution was frozen very rapidly ( $> 10^4$  K/s) with the “freezing machine” MARK4 from the Zentrum Mikroskopie der Universität Basel. Images were taken from a Zeiss 912 Omega TEM, 120 kV equipped with an object cooling system, cryo-stage, video and CCD camera.

### 2.5.4 Light Scattering

**Static Light Scattering (SLS).** SLS is a technique that uses the intensities of scattered light at a number of angles to derive information about the radius of gyration  $R_g$ , molecular mass  $M_w$  of polymers or polymer aggregates and the second virial coefficient  $A_2$ , for example, micellar formation.<sup>109-113</sup>

To use light scattering for the measurement of macromolecules in solution one has to investigate the intensity  $i$  of the scattered light, Figure 28.

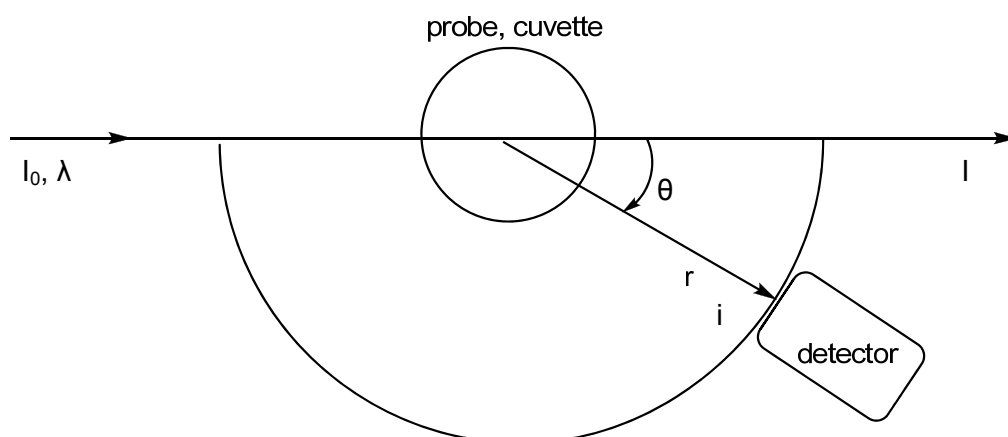


**Figure 28:** Scheme of light scattering apparatus

At the angle  $\theta$  the reduced scattering intensity  $R_\theta$  is described as follow:

$$R_\theta = \frac{i r^2}{I_0} \quad (\text{eq. 4})$$

where  $r$  is the distance between the scattering probe and the detector and  $I_0$  is the intensity at  $\theta = 0$ . The scattering part of the dissolved substance is calculated by:

$$R_\theta = R_{(solution)} - R_{(solvent)} \quad (\text{eq. 5})$$

The Raleigh ratio with the optical constant  $K$  is:

$$R_{\theta} = KcM \quad (\text{eq. 6})$$

with  $K$ :

$$K = \frac{4\pi^2 n_0^2}{N_A \lambda^4} \left( \frac{\delta n}{\delta c_2} \right)_{T,p}^2 \quad (\text{eq. 7})$$

The basic equation for the *averaged* frequency light scattering of small particles ( $d < \lambda/20$ ) is:

$$\frac{Kc_2}{R(\theta)} = \frac{1}{M_W} + 2A_2c_2 + 3A_3c_2^2 + \dots \quad (\text{eq. 8})$$

Bigger macromolecules ( $d > \lambda/20$ ) induce an internal (destructive) interference. The interference is 0 at  $\theta = 0^\circ$  and becomes maximum at  $\theta = 180^\circ$ .

The internal interference is described by the particle scattering factor:

$$P(\theta) = \frac{R_{\theta}(\text{experimental})}{R_{\theta}(\text{without interference})} \quad (\text{eq. 9})$$

and is dependent on the shape & size of the scattered molecules as well as on the wavelength  $\lambda$ . For polymers or even vesicles in solution ( $d > \lambda/20$ ) one observes an attenuation in the intensity of the scattered light due to the molecular interference as shown in Figure 29 whereas  $P(0^\circ) = 1$  and decreases with the increase of the angle  $\theta$  to  $\theta = 180^\circ$ .

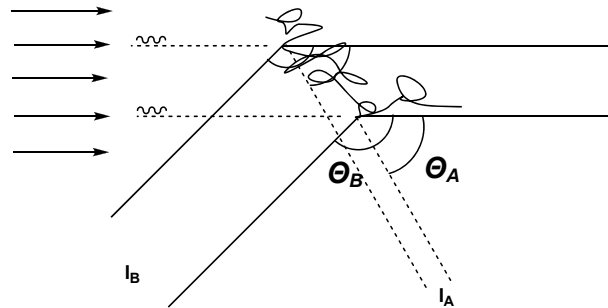


**Figure 29:** scattering of polarized light at a polymer molecule whereas the intensity is  $I_A > I_B$

Including the scattering factor  $P(\theta)$  one obtains the fundamental equation (equation 10) of the averaged frequency light scattering for big molecules ( $d > \lambda/20$ ):

$$\frac{K c_2}{R(\theta)} = \frac{1}{P(\theta)} \left( \frac{1}{M_W} + 2A_2c_2 + 3A_3c_2^2 + \dots \right) \quad (\text{eq. 10})$$

- $c_2$ : concentration of dissolved substance (polymer, vesicles)
- $R(\theta)$ : Raleigh ratio in dependence of the angle  $\theta$
- $P(\theta)$ : scattering factor in dependence of the angle  $\theta$
- $M_W$ : molar mass (weight fraction)

- 
- $A_2, A_3$ : second and third virial coefficient  
 $n_0$ : refractive index of pure solvent  
 $N_A$ : Avogadro number  
 $\lambda$ : wavelength of incident light beam  
 $\frac{\delta n}{\delta c_2}$ : refractive index increment

For a hollow sphere (vesicle) the scattering factor  $P(\theta)$  is:

$$P(X) = \left[ \frac{3}{X^3(1-\gamma^3)} (\sin X - \sin(\gamma X) - X \cos X + \gamma X \cos(\gamma X)) \right]^2 \quad (\text{eq. 11})$$

$X$ :  $q R_s$

$q$ : the monitoring angle  $\theta$  is usually described as the wave vector  $q$ :

$$q = \frac{4\pi n}{\lambda_0} \sin\left(\frac{\theta}{2}\right); n = \text{refractive index and } \lambda = \text{wavelength of incident light beam}$$

$R_s$ : (outer) radius of sphere

$\gamma$ :  $R_i/R_s$

$R_i$ : inner radius

**Dynamic Light Scattering (DLS).** Dynamic light scattering theory is a well established technique for measuring particle sizes over the range from a few nanometer to a few micrometer. The concept uses the idea that small particles in solution move randomly. If light hits small particles the light scatters in all directions as long as the particles are small compared to the wavelength ( $\lambda < 250$  nm). If the light source is monochromatic and coherent, one observes a time-dependent fluctuation in the scattering intensity. These fluctuations are due to the fact that small molecules in solution undergo a Brownian motion and so the distance between the scatterers in the solution is constantly changing with time. The scattered light undergoes either constructive or destructive interference by the surrounding particles and within this intensity fluctuation, information is gained about the time scale of movement of the scattering molecules. The dynamic information of the particles is derived from an autocorrelation function of the intensity trace recorded during the experiment. The second order autocorrelation curve is generated from the intensity course as follows:

$$g^2(q; \tau) = \frac{\langle I(t)I(t+\tau) \rangle}{\langle I(t) \rangle^2} \quad (\text{eq. 12})$$

where  $g^2(q; \tau)$  is the autocorrelation function of the wave vector  $q$  (eq. 12) and delay time  $\tau$ ; and  $I$  is the intensity. At short time delays, the correlation is high because the particles do not have a chance to move to a great extent from the initial state that they were in. The two signals are therefore unchanged compared to a short time interval. As the time

---

delays become longer, the correlation starts to exponentially decrease to zero, meaning that after a long time period has elapsed, there is no correlation between the scattered intensity of the initial and final states. This exponential decay is related to the motion of the particles, specifically to the diffusion coefficient  $D_0$ . The translational diffusion coefficient  $D_0$  is given for highly diluted (and non interacting) systems by the Stokes-Einstein equation:

$$D_0 = \frac{k_B T}{6\pi\eta R_h} \quad (\text{eq. 13})$$

wherein  $\eta$  is the solvent viscosity and  $R_h$  the hydrodynamic radius. The particles (with the radius  $R_h$ ) are viewed as solid spheres.

**SLS and DLS.** Solutions for light scattering were prepared from an extruded (11× through a PC membrane, 0.20 μm cut-off diameter) stock solution of 1 mg/mL. Dilutions from 0.1mg/mL down to 0.01mg/mL were measured. Samples were poured under laminar flow into 10 mm quartz cells mounted in an optical matching bath. Dynamic and static light scattering (DLS, SLS) experiments were done with a commercial goniometer (ALV, USA) equipped with a He:Ne laser (JDS Uniphase, wavelength  $\lambda = 632.8$  nm). Scattering angles were between 50° and 140° and the photon intensity autocorrelation function  $g^2(t)$  was determined with an ALV-5000E correlator. The experiments were performed at  $T = 293 \text{ K} \pm 0.05 \text{ K}$ . The refractive index increment  $dn/dc$  was obtained at 293 K and 632.8 nm with an ALV-DR1 differential refractometer. Angle-dependent DLS data were analyzed via non-linear decay-time analysis supported by regularized inverse Laplace transform of the decay processes (CONTIN algorithm) then characteristic decay times were converted to particle dimension using the hard ball model.<sup>114</sup> Angle and concentration-dependent SLS data were analyzed via Zimm analysis using the vesicle form factor.<sup>114, 115</sup>

**Temperature dependent DLS.** The dynamic light scattering measurements were carried out using a Malvern Instruments particle sizer (Zetasizer Nano ZS, Malvern Instruments, UK) equipped with a He-Ne laser ( $\lambda = 632.8$  nm) working in backscattering modus at a scattering angle of  $2\theta = 173^\circ$ . The aqueous sample solutions were placed into a squared 10 × 10 mm quartz cuvette. Prior to measurement the sample was centrifuged in order to clear it from dust particles. DLS measurements were performed in a temperature range of 5°C to 80°C.

The Stokes-Einstein relation was used to calculate the hydrodynamic radius (of an hydrodynamic equivalent sphere) from the diffusion coefficient,  $D_0$ , as  $R_h = k_B T / (6\pi\eta D_0)$ , where the temperature dependency of the viscosity of water  $\eta(T)$  was taken into account by the Malvern Dispersion Technology Software (version 5.02).

---

### 2.5.5 Small Angle X-ray Scattering

SAXS is a small angle scattering technique where the elastic scattering of x-rays ( $\lambda = 0.1 - 0.2$  nm) by a sample which has inhomogeneities on a length-scale of 1-1000 nm is recorded at very low angles (typically  $0.1^\circ - 10^\circ$ ). This angular range contains information about the shape and size of macromolecules. SAXS is capable of delivering structural information of macromolecules between 5 and 25 nm, of repeat distances in partially ordered systems of up to 150 nm.<sup>116</sup> The materials can be solid or liquid and they can contain solid, liquid or gaseous domains of the same or another material in any combination. The structure of ordered systems like vesicular structures (wall thickness) can also be studied. The method is accurate, non-destructive and requires a minimum of sample preparation.

SAXS experiments with vesicles from PB-PEO-SA-OH/0.1PB-PEO-NTA.d-Cu(II) in solution were performed to confirm the hypothesis that vesicles are formed as indicated by DLS. It should be noted that unilamellar vesicles are weak scatterers in SAXS when compared to multilamellar vesicles and aligned bilayers. Therefore small-angle neutron scattering is used often for the characterization of vesicles, which allows, in contrast to SAXS, a strong contrast variation.<sup>117</sup> More recently a combined global analysis approach has been introduced<sup>118</sup> to overcome the problem of low SAXS intensities from vesicles. Here the slit collimation of the compact SAXS system allowed to detect a sufficiently high scattering intensity for a polymer concentration of 1 mM.

The small-angle X-ray scattering measurements (SAXS) of polymer solutions with a concentration of 1-3 % (w/v) were performed with a SAXSess camera (Anton Paar, Austria). This camera was attached to a laboratory X-ray generator (PW3830, PANalytical) and was operated with a fine focus glass X-ray tube at 40 kV and 50 mA ( $\text{CuK}\alpha$ ,  $\lambda = 0.1542$  nm). A focusing multilayer optics and a block collimator provide a monochromatic primary beam with low background. Samples were filled in a reusable vacuum tight quartz capillary (1 mm in diameter). The scattering vector is defined in terms of the scattering angle,  $\theta$ , and the wavelength of the radiation thus  $q = 4\pi/\lambda \sin(\theta)$ . SAXS data were recorded for 15 min in a  $q$ -range of  $0.04 \text{ nm}^{-1}$  to  $6.0 \text{ nm}^{-1}$  with a CCD detection system (Anton Paar). The two-dimensional intensity data were converted to one-dimensional data with the software SAXSQuant (Anton Paar). The temperature was controlled with a TCS 120 sample holder (Anton Paar) with an accuracy of  $\pm 0.2^\circ\text{C}$ . A reusable capillary was used for all measurements to attain the same scattering volume and background contribution.

---

### 2.5.6 Inductively Coupled Plasma Atomic Emission Spectroscopy (ICP-AES)

Inductively coupled plasma atomic emission spectroscopy is an analytical technique used for the detection of trace metals. It is a type of emission spectroscopy that uses the inductively coupled plasma to produce excited atoms and ions that emit electromagnetic radiation at wavelengths characteristic of a particular element.<sup>119</sup> The intensity of this emission indicates the concentration of the element in the sample.

After extrusion the vesicle solution does not have the original concentration of complexed metal as calculated for the rehydration. One reason is the remaining polymer film on the glass inside in the flask after rehydration; another reason is the loss of material on the PC membranes due to extrusion. As the metal complexation with the amount of binding sides of the functionalized polymer is quantitative one can recalculate the initial concentration of metal. Because ICP is a quantitative method the percentage of complexed metal can be verified by the value of measurement.

The content of nickel (II) and copper (II) in the vesicle solutions were determined with a Cirovision ICP of Spectra, Germany. The specimen flux was 2 mL/min. From a cyclone spray chamber the aqueous vesicle solution was injected into the Argon plasma at a temperature of  $T = 10,000$  K.

### 2.5.7 Zeta-Potential ( $\xi$ -potential)

Zeta potential stands for the electrokinetic potential in colloidal systems (i.e. vesicle solution). A negatively charged surface of a vesicle attracts counterions at the boundary of its surface. This first layer has an opposite, cationic charge that attracts other anions and repels cations. With more layers there will be a boundary at a certain distance from the surface of the vesicle that is electrically neutral. This boundary is the shear plane. Beyond this plane all ions are less tightly bound (diffuse layer). The zeta-potential measures the difference in millivolt (mV) in the electrokinetic potential between the tightly bound layer around the surface and the distant zone of electroneutrality. A value of 25 mV (positive or negative) can be taken as the arbitrary value that separates low-charged surfaces from highly-charged surfaces. The significance of zeta potential is that its value can be related to the stability of colloidal dispersions; it indicates the degree of repulsion between vesicles in solution. A high zeta potential will confer stability, because the solution or dispersion will resist aggregation. When the potential is low, attraction exceeds repulsion and the vesicles will aggregate. Vesicle solutions with high zeta potential (negative or positive) are electrically stabilized. To know the zeta-potential of the vesicles offers also the possibility to immobilize the vesicles on charged surfaces.

---

The zeta-potential of the polymer vesicles (in aqueous solution) were measured at room temperature with a Zetasizer (Malvern, Nano-ZS, UK). The zeta-potential is calculated from the electrophoretic mobility of the vesicles under an applied potential, using Henry's equation and the Smoluchowski approximation.

### 2.5.8 Atomic force (scanning) microscopy (AFM)

Scanning probe microscopy includes a number of parental techniques which – together with the electron microscopy - are the only methods able to give information on the morphology and properties of surfaces with a nanoscale resolution. The operational principle is as follows: A miniaturized sharp probe (tip), attached to the free end of a leaf spring (cantilever), scans in close proximity or in contact with the sample surface. The scan proceeds point by point to define lines (fast scan), from left to right (trace) and from right to left (retrace) and by lines to define a rectangular area (low scan) within the sample. The cantilever acts as mechanical transducer of the surface interactions between the sample and the tip. The AFM set up, shown in Figure 30, consists of a piezoscanner onto which the sample (moving-sample setup) is mounted. The scanner allows the sample movement along the x and y axis (lateral) and along the Z axis (vertical) by applying a certain potential between its electrodes. The cantilever holds the tip whose position is monitored by a laser beam. The laser beam reflects on the back side of the cantilever and its position and intensity is detected by a position-sensitive detector PSD. The PSD is a photodiode divided in four quadrants which calculates the vertical and the lateral movement by measuring the voltage between upper and lower or right and left quadrants. The setup is completed by feedback electronics which enforces the scanning tip to certain mechanical parameters.

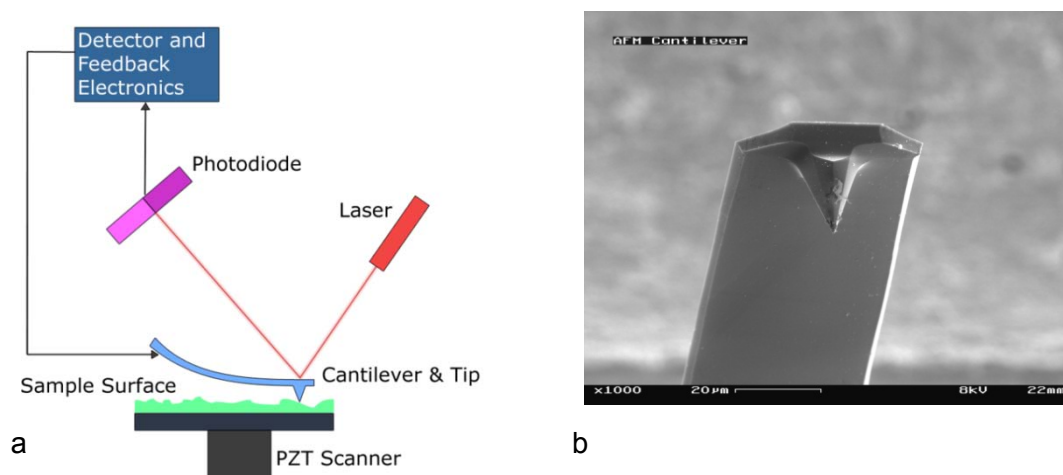


**Figure 30:** a) Block Diagram of Atomic Force Microscope; b) AFM cantilever (after use) in the Scanning Electron Microscope, magnification 1,000 x; both images from: [http://en.wikipedia.org/wiki/Atomic\\_force\\_microscope](http://en.wikipedia.org/wiki/Atomic_force_microscope)

---

Aggregates (i.e. vesicles) with a negatively charged surface attach on positively charged surfaces and remain there due to electrostatic attraction. The surface technique of AFM is an appropriate method to investigate the surface activity of vesicles.

Images on the adsorbed surfaces were performed using a Nanowizard II (JPK, Berlin, Germany) in intermittent mode at room temperature. Silicon nitride tips of spring constant 0.32 N/m (DNP, Veeco Instruments, CA, USA) were used as probes, previously cleaned in acetone and absolute ethanol to remove organic impurities. Glass substrates of 24 mm diameter and 0.17 mm thickness were incubated in a poly(ethylene imine) (PEI) solution ( $w = 2\%$  aqueous solution,  $M_w = 50,000$ ) for 30-45 min and subsequently incubated in polymer vesicle solution for 1-2 hours prior to imaging in phosphate buffer.

### 2.5.9 Quartz Crystal Microbalance (QCM)

QCM is also a surface method. It measures a mass per unit area by detecting the change in frequency of a quartz crystal resonator. The resonance is disturbed by the addition of a polymer film or adhesion of vesicles on the surface of the acoustic resonator. Usually QCM is used in liquid environment which is highly effective for determining the affinity of functionalized vesicles to surfaces. Frequency measurements are made to high precision as it is easy to measure mass densities at a level below  $1 \mu\text{g}/\text{cm}^2$ . In addition to measuring the frequency, the dissipation is often measured to help analysis. The dissipation is a parameter quantifying the attenuation in the system, and is related to the sample's viscoelastic properties. Applying alternating current to the quartz crystal will induce oscillations. With an alternating current between the electrodes of a precisely cut crystal, a standing shear wave is generated. The Q factor, which is the ratio of frequency and band width, can be as high as  $10^6$ . Such a narrow resonance leads to highly stable oscillators and a high accuracy in the determination of the resonance frequency. A change in thickness of the quartz crystal surface correlates to a change in frequency. As a mass is deposited on the surface of the crystal the thickness increases and the frequency of oscillation decreases from the initial value. This frequency change can be quantified and correlated to the mass change using Sauerbrey's equation.<sup>120</sup> The equation is derived from the assumption that the deposited mass is equal in extension of the thickness of the underlying quartz. Due to this, the mass to frequency correlation is independent of electrode geometry and allows mass determination without calibration. The Sauerbrey equation is as follows:

$$\Delta f = \frac{-2f_0^2}{A \sqrt{\rho_q \mu_q}} \Delta m \quad (\text{eq. 14})$$

- 
- $f_0$ : resonant frequency in Hz  
 $\Delta f$ : frequency change in Hz  
 $\Delta m$ : mass change in g  
 $A$ : Piezoelectrically active crystal area in  $m^2$   
 $\rho_q$ : density of quartz ( $\rho_q = 2.648 \text{ g/cm}^3$ )  
 $\mu_q$ : shear modulus of quartz crystal ( $\mu_q = 2.947 \times 10^{11} \text{ g/cm} \times \text{s}^2$ )

A quartz crystal microbalance equipped with flow modules (Q-sense E4, Q-sense, Sweden) allowed to perform up to four parallel in-flow experiments. *In-situ* adsorption experiments of polymer dispersions were done on  $\text{SiO}_2$  coated AT-cut quartz sensors (5MHz resonance frequency, Q-sense, Sweden), which were previously cleaned as follows: immersion in chloroform for 2-5 minutes previous to immersion in surfactant (SDS, 2%) for at least 30 minutes and subsequent UV-cleaning for another 30 minutes. The frequency variation on the vibrating sensors was in real time monitored while exchanging media. The adsorption experiment consisted of a preliminary step where the sensors were coated with positive polyelectrolyte (PEI), an intermediate step of polymer vesicle adsorption and a final step where His tag-EGFP was allowed to adsorb on the sensors; after each step, the sensors were rinsed in the common solvent (phosphate buffer), except for the preliminary step, where they were rinsed in Milli-Q water.

### 2.5.10 Fluorescence Correlation Spectroscopy (FCS)

The interest of FCS measurements is not the fluorescence intensity itself but the random intensity fluctuation around the mean value. Intensity fluctuations are induced by thermal noise in a tiny observation volume, which is in FCS the confocal volume with a volume smaller than  $\frac{1}{4}$  femtoliter. FCS is commonly used to investigate diffusion. Diffusing fluorescent molecules entering or leaving the observation volume cause intensity fluctuations, which are analyzed by calculating the temporal autocorrelation of the observed signal. The autocorrelation is a measure for the self-similarity of a signal and contains information about the average fluctuation strength and duration. To achieve a high signal-to-background ratio a small observation volume is inevitable because the background increases with the size of the observation volume. Additionally a small volume assures a small average number of fluorophores inside the observation volume. Therefore a small volume leads to a high FCS signal.

The measured signal can be described as constant mean intensity  $\langle I \rangle$  and a fluctuating contribution  $\delta I(t)$ . From comparing the signal with each other a correlation function can be calculated:

---


$$G(\tau) = 1 + \frac{\langle \delta I(t) \delta I(t + \tau) \rangle}{\langle I \rangle^2} \quad (\text{eq. 15})$$

Thus obtained function can be fitted to a biophysical model like a liposome or an amphiphilic diblock vesicle.

$$G(\tau) = \frac{1}{N} \cdot \frac{1}{\left(1 + \frac{\tau}{\tau_D}\right)} \cdot \frac{1}{\sqrt{1 + \frac{\tau}{\omega^2 \cdot \tau_D}}} \quad (\text{eq.16})$$

$N$  : number of molecules

$\tau_d$  : diffusion time of molecule

$\omega$  :  $\omega_z / \omega_{xy}$ , aspect ratio of determined volume

The binding affinity of the NTA.d-Ni<sup>2+</sup> groups to the oligohistidines was quantified via fluorescence correlation spectroscopy (FCS). The diffusion time is related to the hydrodynamic radius of a particle via the Stokes-Einstein relation, and its change provides information about the coupling of the fluorescent molecule to a larger target molecule.<sup>121</sup>

Fluorescence-correlation spectroscopy (FCS) measurements were obtained with a Zeiss LSM 510-META/Confocor2 laser-scanning microscope equipped with an argon laser (488 nm) and a 40× water-immersion objective (Zeiss C/Apochromat 40X, NA 1.2), with the pinhole adjusted to 70 μm. Solutions were measured at room temperature in special chambered quartz-glass holders (Lab-Tek; 8-well, NUNC A/S) that provide optimal conditions by reducing evaporation.

## 2.6 Formation of Monolayers

### 2.6.1 Langmuir Isotherms.

To obtain a homogeneous monolayer of the amphiphilic diblock copolymers at the air/water interface, a Langmuir trough was used.

For surface pressure-area ( $\pi$ -A) isotherms, either a Langmuir-Blodgett minitrough (surface area 273 cm<sup>2</sup>) or a BAM trough (surface area 432 cm<sup>2</sup>) was used (both from KSV Instruments Ltd., Helsinki, Finland; solid PTFE/Teflon troughs equipped with two symmetrically moving hydrophilic Delrin barriers and a Wilhelmy plate film balance).

---

Prior to experiments, the trough was thoroughly cleaned with chloroform and ethanol, rinsed with water (double-distilled or ultrapure from ELGA, resistivity 18 M $\Omega$  \*cm, pH 5.5), and filled with the aqueous subphase (either pure water or a phosphate buffer saline, 50 mM Na<sub>2</sub>HPO<sub>4</sub>, 10 mM KCl (Fluka AG, Buchs/CH, puriss.), pH 7.4). The barriers were cleaned with ethanol and rinsed with water. The Wilhelmy plate (made of chromatography paper, ashless Whatman Chr 1, perimeter 20 mm) was equilibrated for at least 20 min. The surface was cleaned repeatedly through compression-aspiration-expansion cycles and checked for impurities.

The polymer was spread dropwise from chloroform solution ( $c = 1$  mg/mL) on the air/water interface. The solvent was allowed to evaporate for 10 min, and the monolayers were compressed at the rate of 10 mm/min. After each measurement, the surface was cleaned and checked for impurities. All experiments were performed at 20°C in a dust-free room; for additional protection from impurities, the trough was housed in a Plexiglas cabinet.

### **2.6.2 Langmuir-Schaeffer films on graphite (HOPG)**

In order to achieve a homogeneous monolayer on a solid surface, the technique of Langmuir-Schaeffer transfer was used. A standard-sized LB trough (R&K, Berlin, Germany) of 160 cm<sup>2</sup> horizontal area and 3 mm depth was used to prepare the LB films. The trough was equipped with a Wilhemy plate that allowed measuring the surface pressure of the air-liquid interface. 40-50  $\mu$ l of polymer solution ( $c = 1$  mg/mL) were deposited onto the water surface and let equilibrate for 5 minutes. The free-standing polymer film was compressed until a surface pressure of 35.5 mN/m was reached, at which the film is in the condensed phase (see *I-A* isotherms in the part “Results & Discussion”). Horizontal transfer from the air-water interface to the HOPG substrate (hydrophobic Highly Ordered Pyrolytic Graphite slides, 10×10×1mm; 7×7×1mm brand grade SPI-1 and 12×12×2mm brand grade ZYA, all from SPI Supplies, USA) was performed under these conditions by means of a motorized lifter (R&K, Berlin, Germany), see Figure 31. The substrates were detached from the interface after 2 hours and kept immediately in water or PBS before experiments. Samples were subject to AFM measurements immediately or after maximum 48 h storage time in Petri dishes with saturated vapor at 4°C.

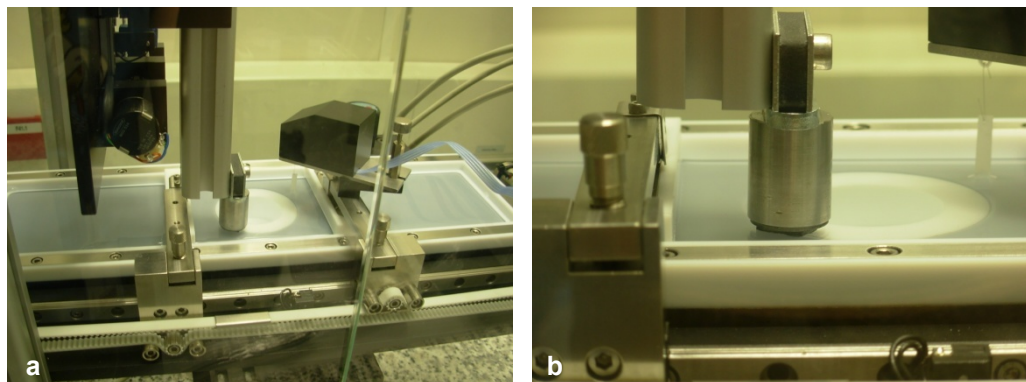


**Figure 31:** Langmuir-Schaeffer transfer: a) a standard-sized LB trough + lifter; b) at the end of the motorized lifter a magnet with the HOPG was attached which dipped onto the film (water) surface.

## 2.7 Characterization Methods of Monolayers

### 2.7.1 Langmuir Isotherms & Brewster Angle Microscopy (BAM)

To characterize polymer monolayers at the air/water interface, we first measured surface pressure ( $\pi$ ) – area ( $A$ ) isotherms, with the accuracy of  $\pm 0.1$  mN/m. Additionally, BAM was performed in order to visualize the formation of the film at the interface.

A BAM2plus Brewster angle microscope (Nanofilm Technologie GmbH, Göttingen, Germany) with a Nd:YAG laser at 532 nm, Nikon 10x Plan Epi SLWD objective (N. A. 0.30), and monochrome CCD camera attached to real-time frame grabber was used, mounted over the Langmuir trough. The images were captured in line scan mode and corrected for geometry and contrast.

### 2.7.2 AFM of monolayer and of monolayer + protein, both on HOPG

The surface morphology of polymer films before and after protein incubation were studied in tapping® mode using a Multimode atomic force microscope equipped with a Nanoscope V controller (Veeco Instruments, Santa Barbara, CA, USA). SiN probes with oxide sharpened tips and cantilever constants of 0.32 N/m (NP-S and DNP-S, Veeco Instruments) were mounted in an enclosed liquid cell that allowed to perform the measurements in liquid. All substrates were imaged in phosphate buffer before and after incubation with protein (incubation time = 1.5h, protein concentration = 0.1 mg/mL = 311 nM).

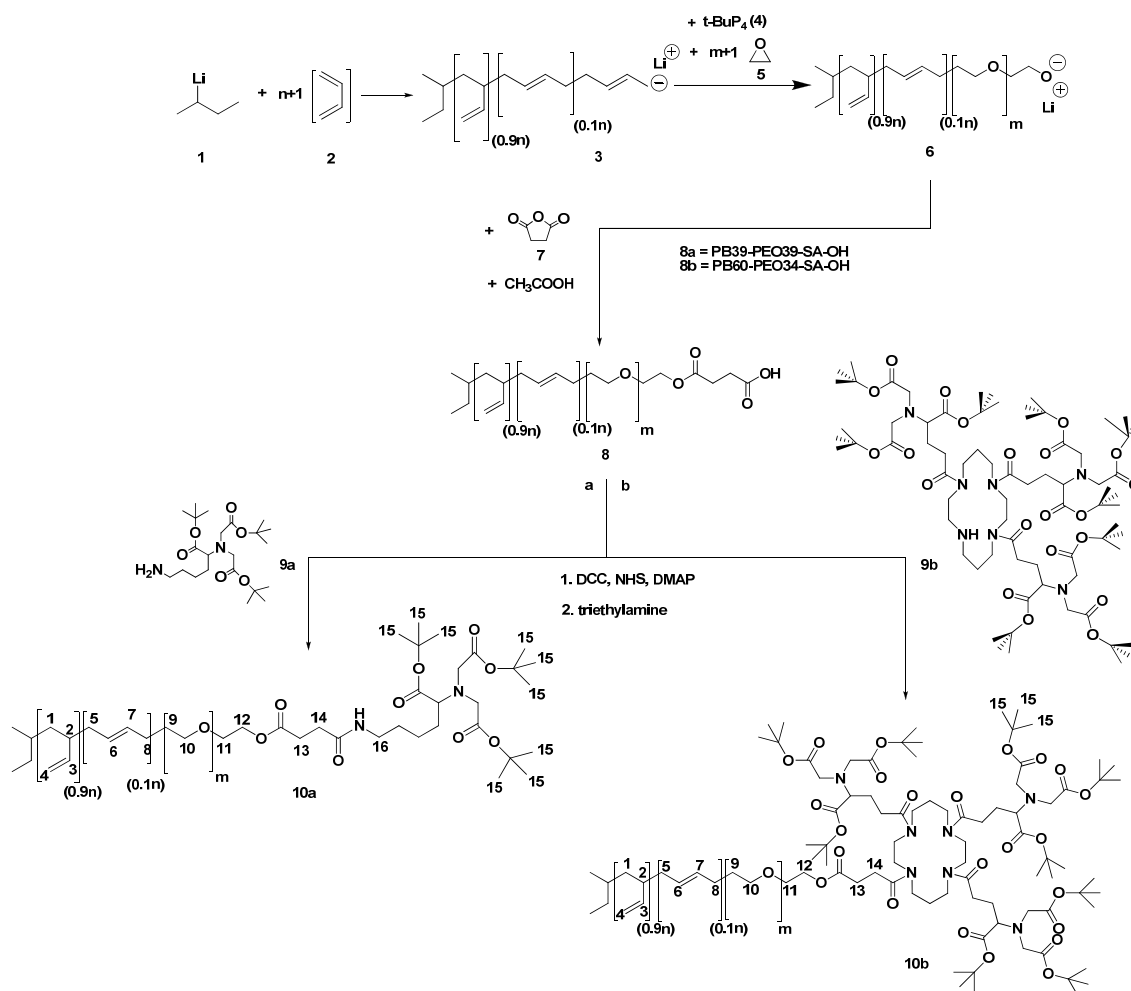
---

To bring the His-tag protein onto the film the buffer was removed from the film and immediately replaced by the protein solution. The incubation time of the protein was 120 min. After incubation the remaining protein solution was removed and the film was rinsed three times with buffer. Samples were scanned under liquid conditions to provide the activity of the hydrophilic part of the diblock copolymer as well as the binding activity of the His tagged proteins.

### 3. Results

#### 3.1 Polymers

Figure 32 shows the complete synthesis of the metal functionalized diblock copolymers  $\text{PB}_{60}\text{-PEO}_{34}\text{-SA-NTA.d-Ni}^{2+}$  (**13a**) and  $\text{PB}_{39}\text{-PEO}_{36}\text{-SA-TrisNTA.d-Ni}^{2+}$  (**13b**). Both diblock copolymers were synthesized in a one pot procedure by anionic polymerization. In order to functionalize the prefunctionalized diblock copolymers (PB-PEO-SA-OH) with nitrilotriacetates two reaction steps (forming of a peptide bond and deprotection) were performed. Another reaction- and purification steps were necessary due to form metal complexes with the NTA.d functionalized polymers. Hence the yield was accordingly low.



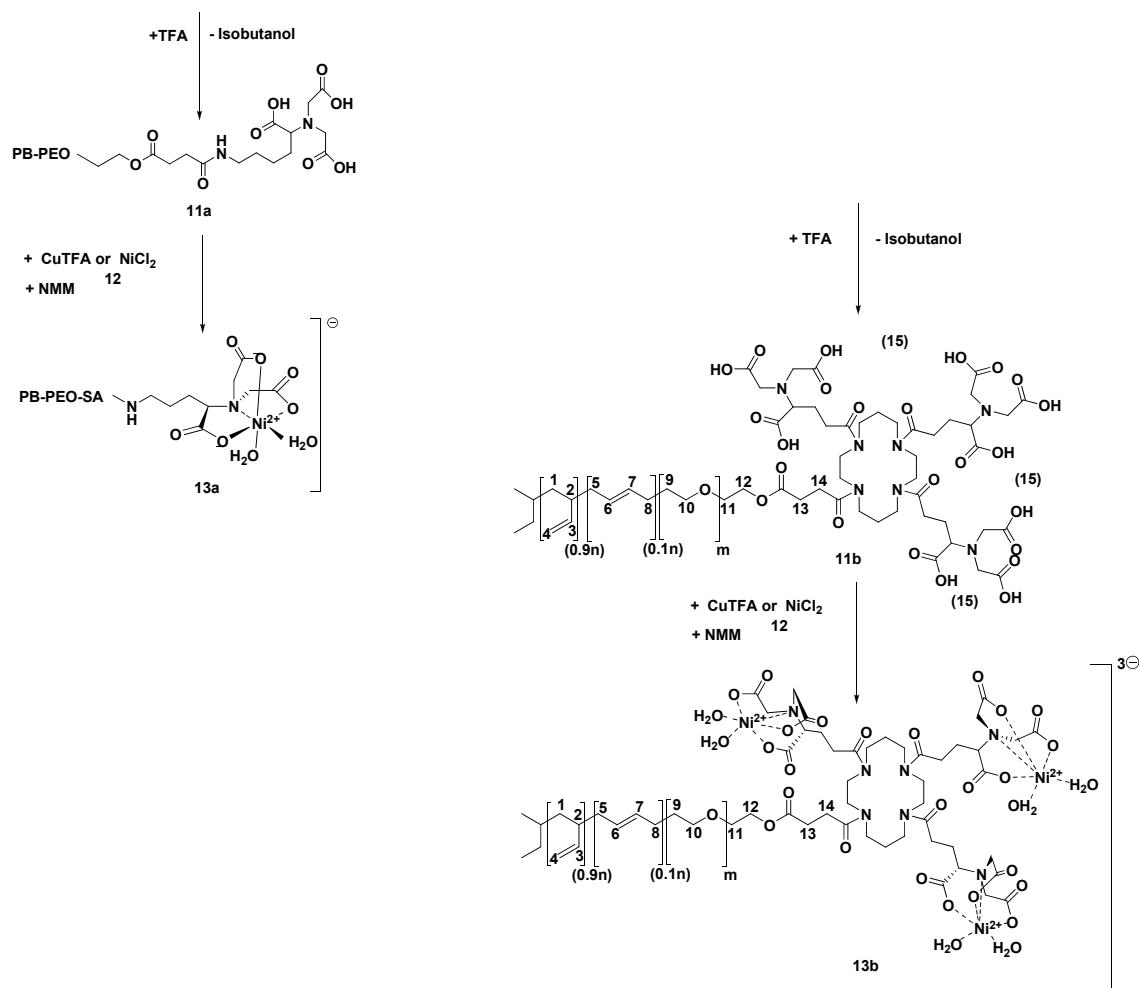


**Figure 32:** Synthesis: Ni<sup>2+</sup>-NTA modified poly(butadiene)-block-poly(ethylene oxide) (PB<sub>60</sub>-PEO<sub>34</sub>-SA-NTA.d-Ni<sup>2+</sup>) **13a**, and Ni<sup>2+</sup>-TrisNTA modified poly(butadiene)-block-poly(ethylene oxide) (PB<sub>39</sub>-PEO<sub>36</sub>-SA-TrisNTA.d-Ni<sup>2+</sup>) **13b** via the semi-ester of the poly(butadiene)-block-poly(ethylene oxide) (PB-PEO-SA-OH) **8**

<sup>1</sup>H-NMR spectroscopy was used to follow each PB-PEO block copolymers functionalization step.

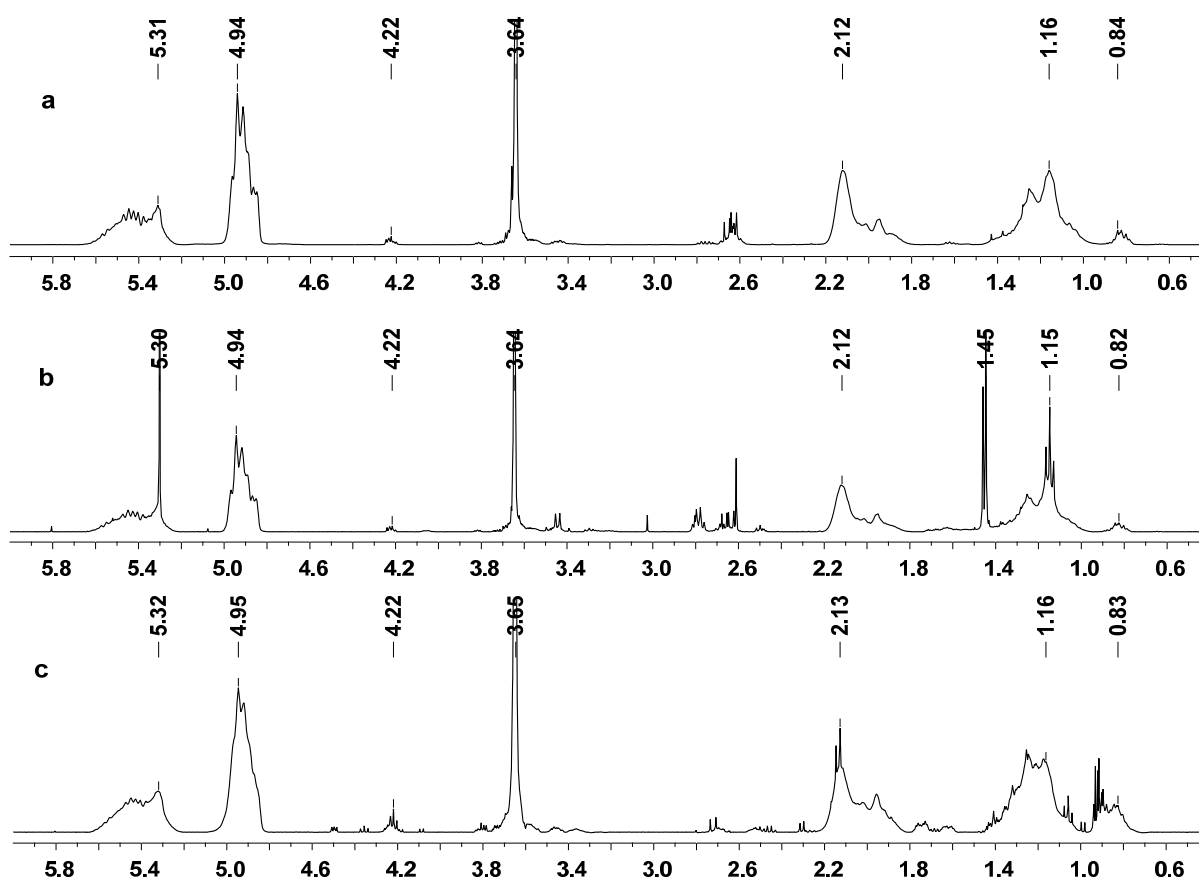


**Figure 33:** <sup>1</sup>H-NMR a) PB<sub>60</sub>-PEO<sub>34</sub>-SA-OH, b) PB<sub>60</sub>-PEO<sub>34</sub>-SA-NTA.p and c) PB<sub>60</sub>-PEO<sub>34</sub>-NTA.d showing the stepwise specific functionalization at 4.22 ppm (-CH<sub>2</sub>-O-CO-) (a), at 1.45 ppm (3×(CH<sub>3</sub>)<sub>3</sub>-) (b) and the decrease of the peak intensity at 1.45 ppm for the deprotected polymer (c).

<sup>1</sup>H-NMR spectroscopy of PB<sub>60</sub>-PEO<sub>34</sub>-SA-OH, **8a** (Figure 33a) shows the presence of the terminal succinic acid semi ester as the multiplet at  $\delta = 4.22$  ppm can be attributed to the methylene protons of the terminal ester. More than 90% of the PEO blocks of the polymers have been converted. Upon reaction of tert.-butyl protected Lys-NTA with polymer PB<sub>39</sub>PEO<sub>36</sub>-SA-OH two very narrow singulets at  $\delta = 1.45$  ppm (s, 27H) (Figure 33b) appeared, which can be attributed to the methyl protons of the tert-butyl groups. As the chemical neighborhood of the methyl protons differs and since they are magnetically not identical a signal of two narrow singulets is obtained. Furthermore <sup>1</sup>H-NMR spectroscopy indicates the formation of an amide bond<sup>43</sup> between the polymer and the protected NTA by the presence of the multiplet at  $\delta = 3.3$  ppm (-CO-NH-CH<sub>2</sub>-C-) (m, 2H). HMBC (2D-NMR) indicates a coupling of these two protons (C-Atom 16; Figure 32, 10a) with the carbon of the

carboxylic group of the amide bond, see Figure 34. Finally the  $^1\text{H-NMR}$  spectrum in Figure 33c indicates that NTA-group deprotection was nearly complete since the peaks for the tert-butyl groups at  $\delta = 1.45$  ppm disappeared.

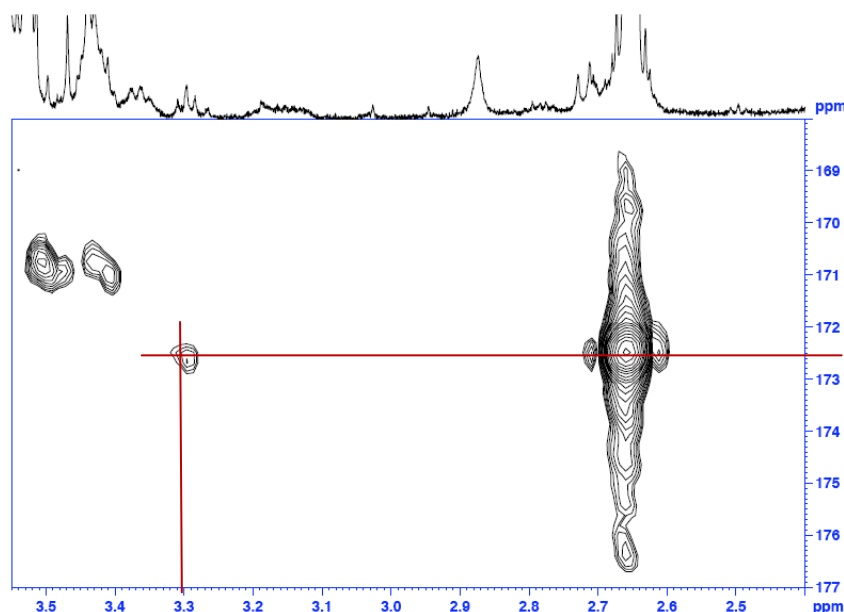


**Figure 34:** HMBC (2D-NMR) of the coupling of the two protons (at C-Atom no. 16) at 3.3 ppm with the carbon (172.4 ppm) of the carboxylic group of the amide bond.

### 3.1.1 List of mixtures of functionalized diblock polymers

The polymer library was already introduced in Table 2 in the Experimental part along with their principal analytical data. Here functionalized diblock copolymer mixtures are presented. Table 2 summarizes the analytical data and investigations regarding the diblock copolymer mixtures composed of 90 mol % pure, non functionalized polymer and 10 mol %  $\text{Me}^{2+}$ -NTA-functionalized polymer.

**Table 2:** List of functionalized diblock copolymer mixtures used for forming monolayers and vesicles.

Mixtures	SEC	NMR	SEC	SEC/ NMR
	$N_n$ (PB)	$N_n$ (PEO)	$M_w/M_n$ (block)	$M_n$ (Block)
<b>PB<sub>60</sub>-PEO<sub>34</sub>-SA-OH/-SA-NTA.d-Ni<sup>2+</sup>/(Cu<sup>2+</sup>)</b> 10 : 1	60	34	1,1	4357
<b>PB<sub>39</sub>-PEO<sub>36</sub>-SA-OH/-SA-TrisNTA.d-Ni<sup>2+</sup>/(Cu<sup>2+</sup>)</b> 10 : 1	39	36	1,1	3548

---

### 3.1.2 Characterization of Metal-functionalized diblock copolymers

EPR and UV-Vis spectroscopy were used to investigate metal coordination with NTA moieties at the hydrophilic chain ends. Complexes were prepared by stirring block copolymer solutions with aqueous solutions of  $\text{Cu}(\text{TFA})_2$  or  $\text{NiCl}_2$ . Addition of the metallic solutions to the polymer solutions led to a change in the color of the latter from pale yellow to green. Figure 35 shows the bluish and greenish color of the metal functionalized diblock copolymers (left: copper (II) and right: nickel (II)), and in the middle the non metal-functionalized sample as a reference.



**Figure 35:** 1)  $\text{PB}_{60}\text{-PEO}_{34}\text{-SA-NTA.d-Cu}^{2+}$ ; 2)  $\text{PB}_{60}\text{-PEO}_{34}\text{-SA-NTA.d}$ ; 3)  $\text{PB}_{60}\text{-PEO}_{34}\text{-SA-NTA.d-Ni}^{2+}$

#### 3.1.2.1 UV/ VIS: Cu, Ni

UV-VIS spectra of  $\text{PB}_{60}\text{-PEO}_{34}\text{-SA-OH}$  **8a** and  $\text{PB}_{39}\text{-PEO}_{36}\text{-SA-OH}$  **8b** were compared to the corresponding metal functionalized polymers  $\text{PB}_{60}\text{-PEO}_{34}\text{-SA-NTA.d-Ni}^{2+}/\text{Cu}^{2+}$  **13a**, (Figure 36) and  $\text{PB}_{39}\text{-PEO}_{36}\text{-SA-TrisNTA.d-Ni}^{2+}/\text{Cu}^{2+}$  **13b**, respectively.

After addition of  $\text{Ni}(\text{II})$ , both metal-NTA-functionalized complexes showed nearly identical electronic spectra. The absorption bands at  $\lambda_1 = 622 \text{ nm}$  and  $\lambda_2 = 390 \text{ nm}$  are characteristic for hexacoordinated  $\text{Ni}(\text{II})$ .<sup>122</sup> The clearly resolved absorption band  $\lambda_1$  in the visible region is attributed to the  ${}^3\text{A}_{2g} \rightarrow {}^3\text{T}_{1g}(\text{F})$  transition. In turn,  $\lambda_2$  is attributed to the  ${}^3\text{A}_{2g} \rightarrow {}^3\text{T}_{1g}(\text{P})$  transition and is present only as a shoulder resulting from several high intensity change transition and UV intra-ligand bands superposition. Both bands confirm  $[\text{Ni}(\text{NTA})(\text{H}_2\text{O})_2]^-$  complex existence.<sup>123</sup> Electronic spectra of  $\text{Cu}(\text{II})$ -NTA modified polymers were similar. The large d-d band at  $745 \text{ nm}$  indicates a pyramidal symmetry around the metal. This band is characteristic for  $[\text{Cu}(\text{NTA})\text{H}_2\text{O}]$ ,<sup>124</sup> despite its slight blue-shift, as a consequence of the polymer environment. Figure 36 shows the UV/VIS spectra of the metal ( $\text{Cu}^{2+}$  and  $\text{Ni}^{2+}$ ) functionalized polymer  $\text{PB}_{60}\text{-PEO}_{34}\text{-SA-NTA.d-Me}^{2+}$ . The non functionalized polymer is drawn in black and shows negligible absorbance.

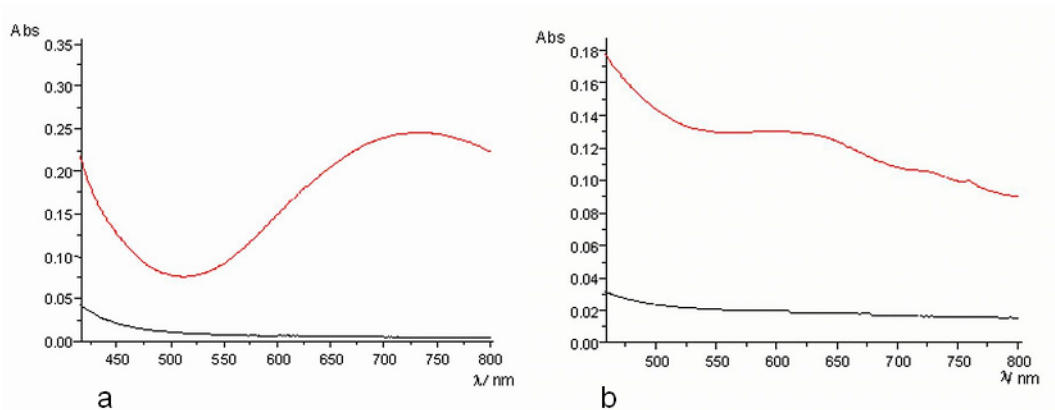


**Figure 36:** a) Cu: UV-VIS spectra of PB<sub>60</sub>-PEO<sub>34</sub>-SA-NTA.d-Cu<sup>2+</sup> (13a; red) and PB<sub>60</sub>-PEO<sub>34</sub>-SA-OH (8b; black) in chloroform at RT. b) Ni: UV-VIS spectra of PB<sub>60</sub>-PEO<sub>34</sub>-SA-NTA.d-Ni<sup>2+</sup> (13a; red) and PB<sub>60</sub>-PEO<sub>34</sub>-SA-OH (8a; black), in chloroform at RT. Concentration for all samples were  $c = 0.1$  mg/mL, the cell length was 1 cm.

### 3.1.2.2 EPR: Cu

The complex formation of Cu(TFA)<sub>2</sub> with polymers **8a**, **11a**, and **13a** was examined by EPR. Different coordinations of Cu(II) are directly reflected in the EPR spectra, since the spin Hamiltonian parameters of copper ions are very sensitive to changes in the coordination sphere around the metal.<sup>106</sup> This makes Cu(II) ideally suited as a probe to investigate the interactions with the corresponding polymers.

As shown in Figure 37a, the shape of the EPR spectrum for polymer **8b** indicates the presence of two paramagnetic Cu(II) species (parallel (low-field) region of the spectrum: \* and + signals). Therefore, the frozen solution spectrum was simulated taking into account two paramagnetic species, **A** and **B**. (Figure 37b). The best fit with axial gromagnetic and hyperfine tensors (see Table 2) suggests a formation in a 3:2 ratio (A:B).

The overall shape of the polymer-copper(II) complex (**13b**) in the EPR spectrum was conserved but intensity decreased significantly. This suggests the same paramagnetic species as before, but in a significantly lower concentration. Finally, in the presence of the polymer 13b, with a free NTA end group, a different EPR spectrum was obtained (Figure 37c).

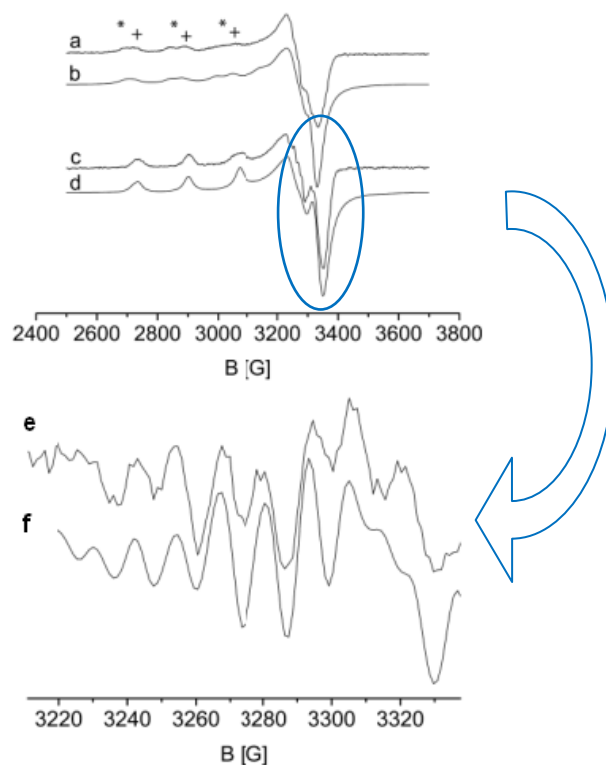


**Figure 37:** EPR spectra of the Cu(II) paramagnetic species formed by addition of Cu(TFA)<sub>2</sub> to: a) PB<sub>39</sub>-PEO<sub>36</sub>-SA-OH, c) PB<sub>39</sub>-PEO<sub>36</sub>-SA-TrisNTA.d, together with their simulations b) and d), respectively. “\*” signals belong to the species A, while “+” signals belong to species B. A close up of the perpendicular region of the D2-EPR spectrum of c), is presented in e), together with its simulation f). The spectra were recorded at 77K.

The spectrum was simulated by taking into account axial gyromagnetic and hyperfine tensors (Figure 37d). EPR parameters (Table 3), and the presence of a superhyperfine pattern in the perpendicular region of the EPR spectrum points out clearly to the formation of a new type of paramagnetic Cu(II). In order to improve the resolution we measured the second derivative of the absorption spectrum in the high-field region of the EPR spectrum (see circle in Figure 37). The presence of superhyperfine structure provides information about nitrogen nuclei present in the first coordination sphere around the metal.<sup>125</sup> In our system copper (II) has only one nitrogen atom in its coordination sphere, with a hyperfine coupling constant of  $a_N = 1.1$  mT, similar to the values of the hyperfine coupling constants found in other <sup>1</sup>N<sup>3</sup>O Cu(II) complexes.<sup>126</sup> The fact that only one paramagnetic species is present (Figure 37c) together with the presence of N in the coordination sphere of this species let us to conclude that the metal is exclusively bound to the NTA moiety of the block copolymer.

**Table 3:** Spin Hamiltonian parameters of the Cu(II) paramagnetic species formed by addition of Cu(TFA)<sub>2</sub> to the functionalized copolymer systems.

polymer system		g			A [mT]		
		g <sub>xx</sub>	g <sub>yy</sub>	g <sub>zz</sub>	A <sub>xx</sub>	A <sub>yy</sub>	A <sub>zz</sub>
PB <sub>39</sub> -PEO <sub>36</sub> -SA-OH:	A	2.047	2.053	2.309	2.0	2.0	14.6
	B	2.053	2.053	2.272	1.5	1.5	16.0
PB <sub>39</sub> -PEO <sub>36</sub> -SA-TrisNTA-d.:	C	2.052	2.052	2.253	3.3	3.1	16.4

The samples containing Ni(II) together with polymers **8b**, **11b** and **13b** were silent in EPR, from room temperature until 77K, as expected.

## 3.2 Vesicles

In order to test the accessibility of the Ni<sup>2+</sup>-NTA groups, vesicles were prepared from a mixture of 10 mol% of polymer **13a** in polymer **8a** as well as from a mixture of 10 mol% of polymer **13b** in polymer **8b** (metal-doped vesicles), using the film rehydration & electroformation methods.<sup>127</sup> The metal-free diblock copolymers **PB<sub>60</sub>-PEO<sub>34</sub>-SA-NTA.d** and **PB<sub>39</sub>-PEO<sub>36</sub>-SA-TrisNTA.d** and the **polymer mixtures** (10 mol% metal-doped polymers) formed vesicular structures, i.e. the presence of the metal functionalized polymer did not affect the self-assembly behavior. Similar behavior has been reported for other end-group functionalized block copolymers.<sup>87, 89, 90</sup>

### 3.2.1 Giant vesicles and vesicular structures.

Both film rehydration method and electroformation method formed giant vesicles visible under the optical microscope. Here the polymer mixture vesicles PB<sub>60</sub>-PEO<sub>34</sub>-SA-OH/0.1PB<sub>60</sub>-PEO<sub>34</sub>-SA-NTA.d-Ni<sup>2+</sup> and PB<sub>39</sub>-PEO<sub>36</sub>-SA-OH/0.1PB<sub>39</sub>-PEO<sub>36</sub>-SA-TrisNTA.d-Ni<sup>2+</sup> were examined and imaged.

In general the polymer mixture PB<sub>39</sub>-PEO<sub>36</sub>-SA-OH/0.1PB<sub>39</sub>-PEO<sub>36</sub>-SA-TrisNTA.d-Ni<sup>2+</sup> formed giant vesicles in Milli-Q water (Figure 38 - Figure 40) and in salt solutions (Figure 41 - Figure 42) by the rehydration method.

The polymer mixture PB<sub>60</sub>-PEO<sub>34</sub>-SA-OH/0.1PB<sub>60</sub>-PEO<sub>34</sub>-SA-NTA.d-Ni<sup>2+</sup> formed a heterogeneous size distribution of vesicles in buffers easily by rehydration (Figure 44).

Electroformation was only performed in bidistilled water.<sup>107</sup> The polymer mixture PB<sub>60</sub>-PEO<sub>34</sub>-SA-OH/0.1PB<sub>60</sub>-PEO<sub>34</sub>-SA-NTA.d-Ni<sup>2+</sup> formed much bigger giant vesicles (Figure 45)

---

than the polymer mixture  $\text{PB}_{39}\text{-PEO}_{36}\text{-SA-OH}/0.1\text{PB}_{39}\text{-PEO}_{36}\text{-SA-TrisNTA.d-Ni}^{2+}$  (Figure 46).

As it was much easier to obtain a “free” vesicles solution (vesicles not attached to an electrode) by the rehydration method, the vesicles for further investigations were produced via rehydration. Furthermore the vesicles were made in TRIS or PBS buffer to gain a protein friendly solution. Therefore all vesicles for further investigations were made by the polymer mixture  $\text{PB}_{60}\text{-PEO}_{34}\text{-SA-OH}/0.1\text{PB}_{60}\text{-PEO}_{34}\text{-SA-NTA.d-Ni}^{2+}$  in PBS or TRIS buffer via rehydration and further extrusion.

### 3.2.1.1 Optical microscopy imaging:

The **film rehydration** method produced a homogeneous vesicle solution containing giant vesicles (GUVs) of the polymer  $\text{PB}_{39}\text{-PEO}_{36}\text{-SA-OH}/0.1\text{PB}_{39}\text{-PEO}_{36}\text{-SA-TrisNTA.d-Ni}^{2+}$ , with diameters up to 8  $\mu\text{m}$  (Figure 38). Upon solvent evaporation, the drop aspect changes until a dried surface, characterized by hexagonal structures, was obtained. Here the very low polymer concentration of 5  $\mu\text{M}$  led to a homogeneous vesicle size distribution. The polymerfilm of the rehydration was obviously so thin and uniformly coated on the inside wall of a flask that the formation of vesicles of the same size was kinetically favored. Regarding to literature<sup>58</sup>, the hydrophobic to hydrophilic ratio of the diblock copolymer was 1:0.92 (PB:PEO) which influenced the packing parameter on the self-assembly structures to vesicles.

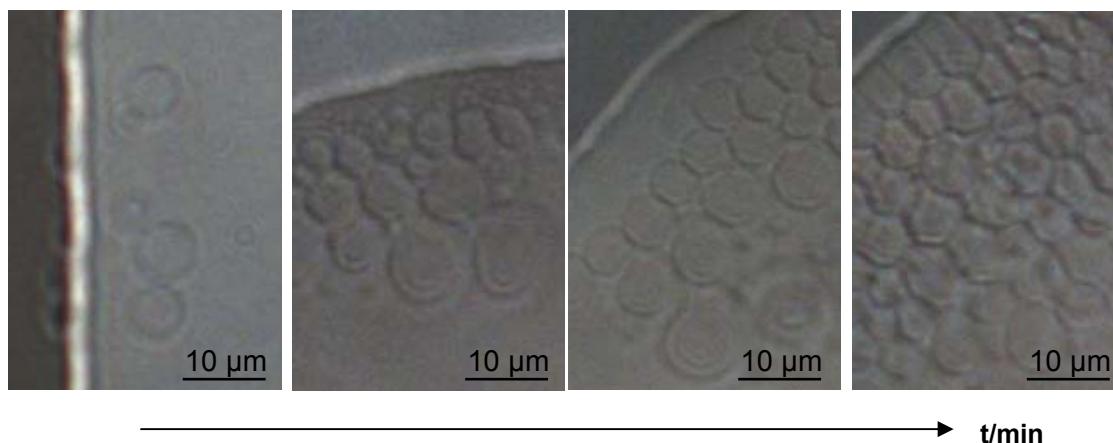


**Figure 38:** Film Rehydration. Images of a drop of  $\text{PB}_{39}\text{-PEO}_{36}\text{-SA-OH}/\text{PB}_{39}\text{-PEO}_{36}\text{-SA-TrisNTA.d-Ni}^{2+}$  10:1,  $c(\text{polymer, stock solution}) = 5 \mu\text{M}$ . Microscope: Transmission Microscope Leica JPK, magnification: 100x10 Pol. 1, media: Milli-Q water.

In solution of the same concentration, GUVs with inner vesicles were observed. In contrast to lipid vesicles<sup>107</sup> the membranes remained stable and the inner vesicles resided entrapped. The GUV with two smaller vesicles inside, see Figure 39, was monitored for at least one hour at room temperature.

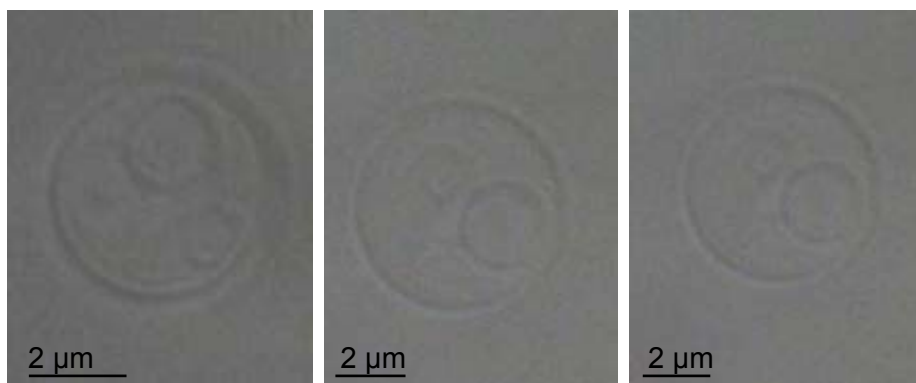


**Figure 39:** Vesicle-in-vesicle structure. PB<sub>39</sub>-PEO<sub>36</sub>-SA-OH/ PB<sub>39</sub>-PEO<sub>36</sub>-SA-TrisNTA.d-Ni<sup>2+</sup> 10:1  
c(polymer, stock solution) = 5 μM, Microscope: Transmission Microscope Leica JPK, magnification:  
100x10 Pol. 1, media: Milli-Q water.

In more concentrated vesicle dispersions of the polymer, fractions with heterogeneous in size vesicles and flakes were observed due to film particles floating into the solution, see Figure 40. Due to the relatively high polymer concentration, the polymer was not uniformly coated on the inside wall of the flask and hence some polymer flakes were removed from the thicker parts of the film by shear forces during rehydration.

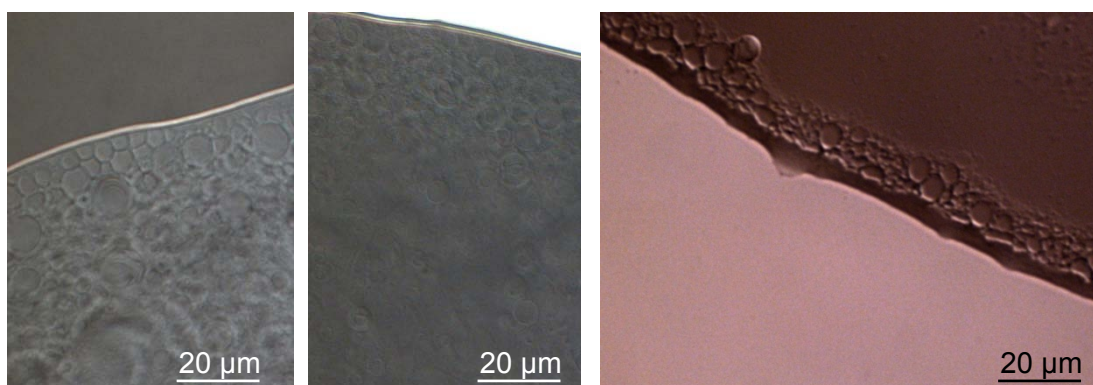


**Figure 40:** Film rehydration. PB<sub>39</sub>-PEO<sub>36</sub>-SA-OH/ PB<sub>39</sub>-PEO<sub>36</sub>-SA-TrisNTA.d-Ni<sup>2+</sup> 10:1  
c(polymer, stock solution) = 800 μM, Microscope: Transmission Microscope Leica JPK, magnification:  
100x10 Pol. 1, media: Milli-Q water.

Vesicle formation of the same diblock copolymer was now tested in a salt solution in order to create a medium of higher ionic strength and to test the usability of buffers. The use of sodium chloride solutions with different concentrations resulted in the formation of different vesicular structures of PB<sub>39</sub>-PEO<sub>36</sub>-SA-OH/0.1PB<sub>39</sub>-PEO<sub>36</sub>-SA-TrisNTA.d-Ni<sup>2+</sup> polymer.

Figure 41 shows vesicles with pearl necklace-like structures obtained in a 300 mM sodium chloride solution. The surfactant packing parameter  $v/a_l$  (with the length  $l$  of the hydrophobic block being constant) determines the volume to area ratio  $v/a$ .<sup>65</sup> Changes in the packing parameter  $v/a$  are induced by swelling or deswelling, e.g. by introducing or changing a salt concentration. Also temperature changes affect the volume to area ratio

*v/a*. Similar change in the shape from a tubular structure (PB-PEO) to pearl necklace-like vesicles after a rapid temperature decrease was also reported by Antonietti and Foerster.<sup>58</sup> Other factors determining vesicle shapes include the composition of the diblock and the electrolyte concentration which influences the electrostatic interactions.<sup>58</sup> As in our case the temperature and the composition remained constant, most likely the salt concentration caused the change in the vesicle's shape. Ions interact with the hydrogen bonds between the hydrophilic part of the diblock copolymer and the solvent (water) and induce electrostatic forces between the single hydrophilic strands of the vesicle membrane. More electrostatic repulsive forces between the outer hydrophilic strands than between the inner hydrophilic strands – due to the higher number of outer strands<sup>65</sup> - might determine smaller radii which lead to these pearl necklace-like structures or even wormlike micelles.

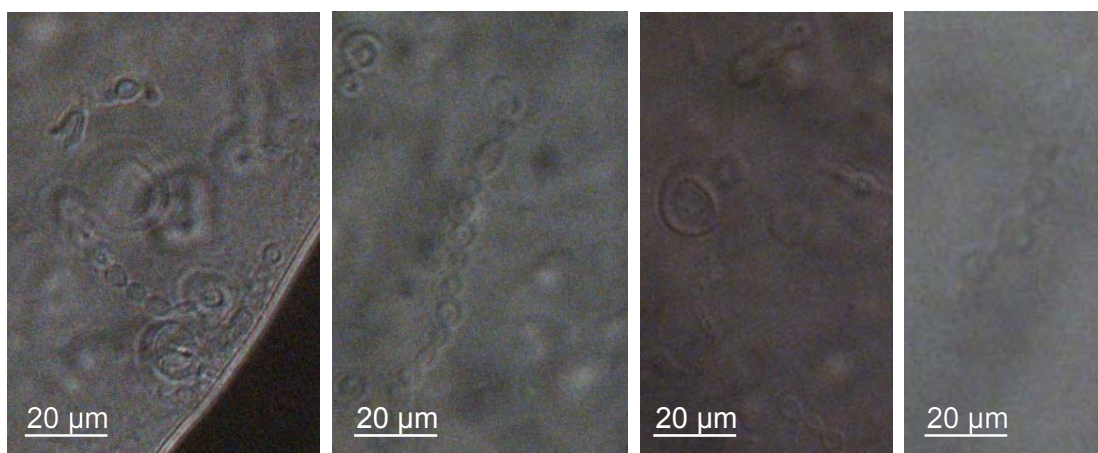


**Figure 41:** Film rehydration. PB<sub>39</sub>-PEO<sub>36</sub>-SA-OH/ PB<sub>39</sub>-PEO<sub>36</sub>-SA-TrisNTA.d-Ni<sup>2+</sup> 10:1  
*c*(polymer, stock solution) = 400 μM, Microscope: Transmission Microscope Leica JPK, magnification: 100x10 Pol. 1, media: 300 mM NaCl-solution.

In a 100 mM sodium chloride solution (Figure 42), vesicles of PB<sub>39</sub>-PEO<sub>36</sub>-SA-OH/0.1PB<sub>39</sub>-PEO<sub>36</sub>-SA-TrisNTA.d-Ni<sup>2+</sup> with one or two tails, i.e. spermasomes, were obtained. Interestingly in a lower concentrated salt solution the pearl necklace-like structures disappeared and were replaced by spermasomes. Here the “head” remained in the classical vesicle shape ( $v/a$  = 1/2 to 1) but its tail looked very much like a cylindrical micelle ( $v/a$  = 1/3 to 1/2) which was also shown in the TEM image of Figure 48. A reason for the conformational change might be the change in the concentration of the electrolyte. Polymer structures have such a low molecular solubility in salt solutions that the conformation and size is not a product of exchange and equilibrium process but trapped kinetically by the preparation conditions. So the change in sodium chloride concentration and therefore the change in the ionic strength might be an effective factor to control vesicles shapes. Also the terminal Ni<sup>2+</sup>-NTA functionalization of the hydrophilic polymer part might

---

induce a screening at different parts of the self assembled structures leading to spermasome like shapes.

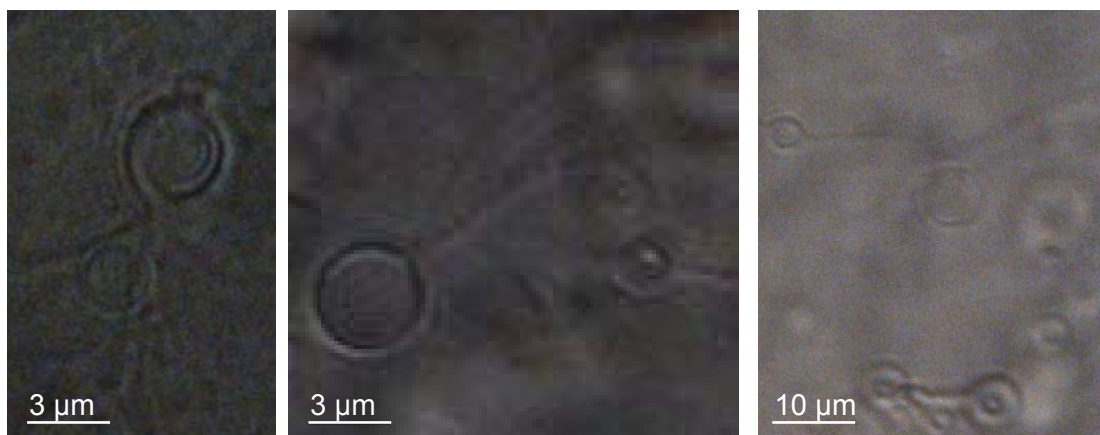


**Figure 42:** Film rehydration. PB<sub>39</sub>-PEO<sub>36</sub>-SA-OH/ PB<sub>39</sub>-PEO<sub>36</sub>-SA-TrisNTA.d-Ni<sup>2+</sup> 10:1 c(polymer, mother solution) = 400 μM, Microscope: Transmission Microscope Leica JPK, magnification: 100x10 Pol. 1, media: 100 mM NaCl-solution.

The other diblock copolymer **PB<sub>60</sub>-PEO<sub>34</sub>-SA-OH** and its functionalized homologues have higher molecular weight and a bigger hydrophobic segment compared to the PB<sub>39</sub>-PEO<sub>36</sub> polymer mentioned above. Vesicles were prepared by the rehydration method (using MilliQ-water). The polymer film in water was rotated at 120 rpm and at 45°C for two weeks. After extrusion through a PC membrane (5 μm pore size), both vesicles homogeneous in size, and polymer particles were obtained, as shown in Figure 43.



**Figure 43:** Film rehydration. PB<sub>60</sub>-PEO<sub>34</sub>-SA-OH/ PB<sub>60</sub>-PEO<sub>34</sub>-SA-NTA.d-Ni<sup>2+</sup> 10:1; c(polymer) = 800 μM, 14d at 120 rpm and T= 45°C, 5 μm extruded: Microscope: Transmission Microscope Leica JPK, magnification: 100x10 Pol. 1, media: Milli-Q water..

In contrast PB<sub>60</sub>-PEO<sub>34</sub>-SA-OH/PB<sub>60</sub>-PEO<sub>34</sub>-SA-NTA.d-Ni<sup>2+</sup>(10:1) formed in PBS buffer (pH 7.4) a heterogeneous mixture of vesicles, wormlike micelles, spermasomes and other vesicular structures, as shown in Figure 44. Obviously the high ionic strength of the buffer

---

led to repulsive electrostatic interactions between the hydrophilic strands which forced the swollen polymer bilayers (rehydration) to close into vesicular structures.

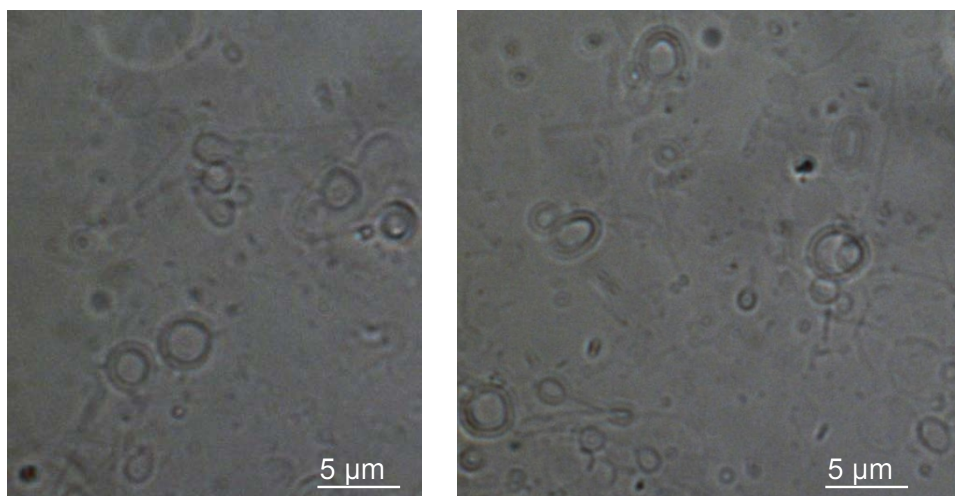


**Figure 44:** Film rehydration.  $\text{PB}_{60}\text{-PEO}_{34}\text{-SA-OH}/\text{PB}_{60}\text{-PEO}_{34}\text{-SA-NTA.d-Ni}^{2+}$  10:1 c(polymer, mother solution) = 400  $\mu\text{M}$ , 5d at 120 rpm and at  $T= 45^\circ\text{C}$ ; Microscope: Transmission Microscope Leica JPK, magnification: 100x10 Pol. 1, media: PBS buffer, pH 7.4.

Applying the **electroformation** method for the  **$\text{PB}_{60}\text{-PEO}_{34}\text{-SA-OH}$**  and its functionalized homologue mixtures  $\text{PB}_{60}\text{-PEO}_{34}\text{-SA-OH}/0.1\text{PB}_{60}\text{-PEO}_{34}\text{-SA-NTA.d}$  and  $\text{PB}_{60}\text{-PEO}_{34}\text{-SA-OH}/0.1\text{PB}_{60}\text{-PEO}_{34}\text{-SA-NTA.d-Ni}^{2+}$  in bidistilled water resulted in the formation of GUVs with diameters up to 100  $\mu\text{m}$  (Figure 45). Electroformation was performed in bidistilled water as this technique is limited to low ionic strengths, i.e. below 10 mM NaCl,<sup>128</sup> which is a much lower salt concentration compared to the desired buffers.

Since the growing vesicles were observed to vibrate at the same frequency as the applied ac voltage, the electric field may serve to create a gentle mechanical agitation that leads to the formation and detachment (lower frequency) of the GUVs.<sup>129</sup>

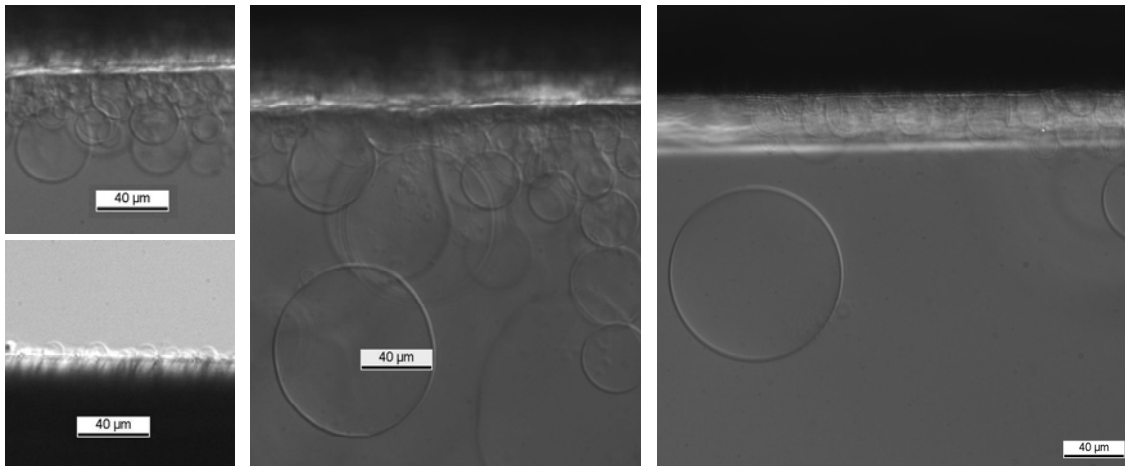


**Figure 45:** Electroformation.  $\text{PB}_{60}\text{-PEO}_{34}\text{-SA-OH}$  and  $\text{PB}_{60}\text{-PEO}_{34}\text{-SA-OH/PB}_{60}\text{-PEO}_{34}\text{-SA-NTA.d-Ni}^{2+}$  (10:1), media: bidistilled water. Transmission Microscope Leica DMIRE2, magnification: 20x10 Pol. 1, The black bar in all images is a Pt electrode covered with polymer film.

Also the polymer mixture  $\text{PB}_{39}\text{-PEO}_{36}\text{-SA-OH/PB}_{39}\text{-PEO}_{36}\text{-SA-TrisNTA.d-Ni}^{2+}$  (10:1) formed vesicles via electroformation as shown in Figure 46. But in contrast to the  $\text{PB}_{60}\text{-PEO}_{34}\text{-SA-OH}$  polymer homologues, it formed a jelly like layer which ended in mycelia like structures with vesicles “on top”. Here the diblock copolymer has a hydrophobic to hydrophilic ratio (PB:PEO) of 1:0.92 which is nearly 1:1 considering also the terminal functional group of the hydrophilic  $\text{TrisNTA-Ni}^{2+}$ . In contrast, the other diblock copolymer consists of a higher molecular weight and a bigger hydrophobic segment with a hydrophobic to hydrophilic ratio (PB:PEO) of 1:0.57. A larger hydrophilic moiety leads to a more homogeneous jelly like layer in aqueous media and hinders the system to create compartments, i.e. vesicles.

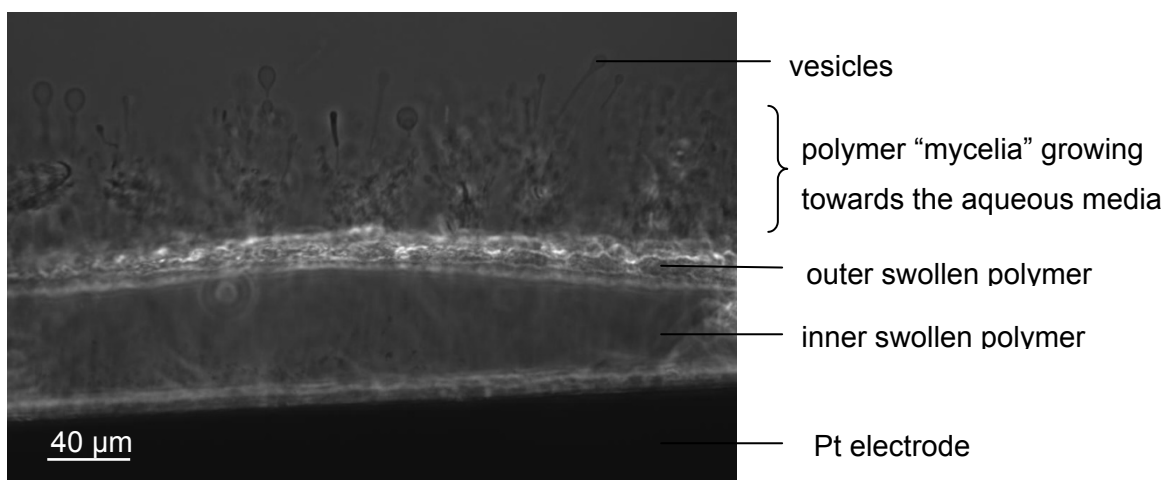


**Figure 46:** Electroformation.  $\text{PB}_{39}\text{-PEO}_{36}\text{-SA-OH/PB}_{39}\text{-PEO}_{36}\text{-SA-TrisNTA.d-Ni}^{2+}$ , (10:1); Transmission Microscope Leica DMIRE2, magnification: 20x10 Pol.1; media: bidistilled water.

### 3.2.1.2 TEM

The rehydration method was used to form vesicles from the polymer mixture PB<sub>60</sub>-PEO<sub>34</sub>-SA-OH/PB<sub>60</sub>-PEO<sub>34</sub>-SA-NTA.d-Cu<sup>2+</sup> (10:1) in TRIS buffer pH 8.0. After extrusion through a 0.2 μm pore size PC membrane, vesicles have a heterogeneous shape distribution with an overall size of 200 nm in diameter, shown in Figure 47.

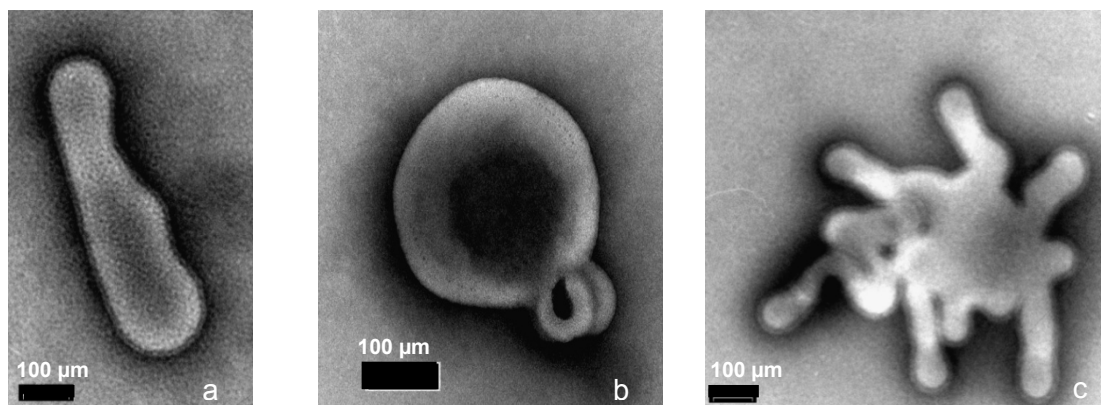


**Figure 47:** Film rehydration. PB<sub>60</sub>-PEO<sub>34</sub>-SA-OH/PB<sub>60</sub>-PEO<sub>34</sub>-SA-NTA.d-Cu<sup>2+</sup> 10:1; a, b: c(polymer) = 222 μM; c: c(polymer) = 22 μM; 0.2 μm extruded, media: TRIS buffer, pH 8.0; Philips CM-100 TEM, 80 kV.

Figure 48 shows that the polymer mixture PB<sub>39</sub>-PEO<sub>36</sub>-SA-OH/PB<sub>39</sub>-PEO<sub>36</sub>-SA-TrisNTA.d-Cu<sup>2+</sup> (10:1) formed spermasomes in a lower concentrated salt media. The vesicles of this polymer mixture were formed in bidistilled water, but due to the negative staining of the probe, the final media may be characterized as a lower concentrated salt solution. Interestingly the tail of the vesicle consists of a helical structure and not a rod-like micelle. Obviously the systems self assemble into much more complicated structures than predicted by literature.<sup>58</sup> This is may be due to the 10% Ni<sup>2+</sup>-NTA functionalization of the polymers.

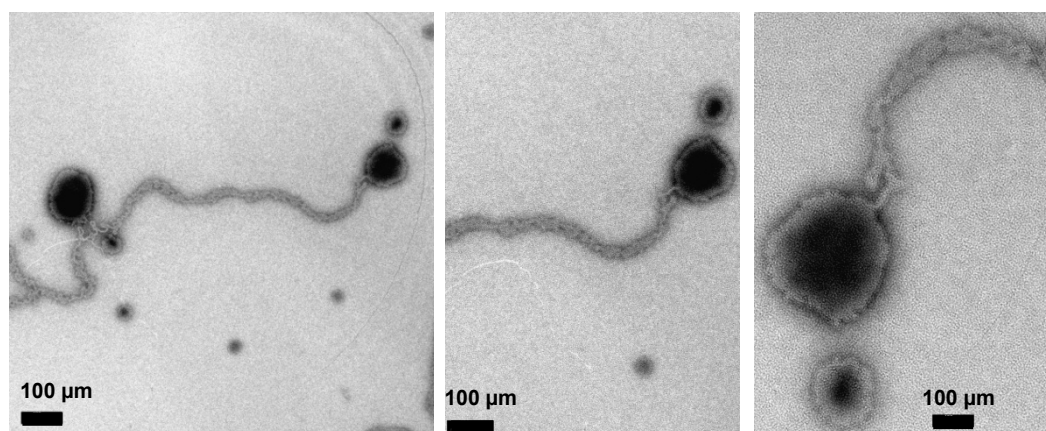


**Figure 48:** Film rehydration. PB<sub>39</sub>-PEO<sub>36</sub>-SA-OH/PB<sub>39</sub>-PEO<sub>36</sub>-SA-TrisNTA.d-Cu<sup>2+</sup> (10:1); c(polymer) = 270 μM, media: bidistilled water; Philips CM-100 TEM, 80 kV

### 3.2.1.3 Cryo-TEM

Figure 49 shows vesicles populations prepared from PB<sub>60</sub>-PEO<sub>34</sub>-SA-OH/PB<sub>60</sub>-PEO<sub>34</sub>-SA-NTA.d-Cu<sup>2+</sup> (10:1) polymer mixture at a concentration of 0.22 μM and after extrusion (11×) through a 0.2 μm cut-off diameter PC membrane. Most of the vesicles have a diameter of 200 nm or below. Some vesicles show a hexagonal-like structure which may be due to crystalline water attached to the hydrophilic part of the polymers. The strong contrast of the vesicles is due to the 10% copper functionalization of the polymers. In all cases, the vesicle membrane thickness estimated from the images was approximately 10 nm.

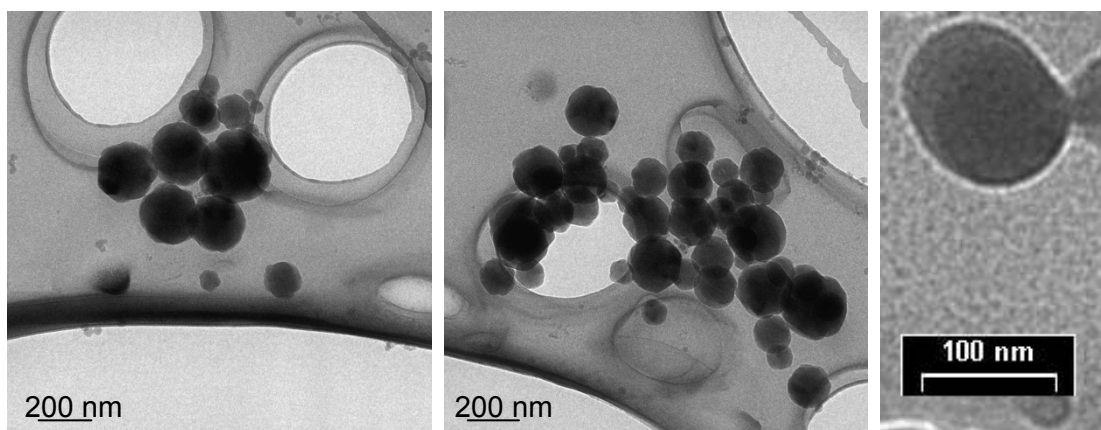


**Figure 49:** Film rehydration. PB<sub>60</sub>-PEO<sub>34</sub>-SA-OH/PB<sub>60</sub>-PEO<sub>34</sub>-SA-TrisNTA.d-Cu<sup>2+</sup> (10:1); c(polymer) = 0.22 μM; 0.2 μm extruded, media: TRIS buffer, pH 8.0; Zeiss 912 Omega TEM, 120 kV

### 3.2.2 Vesicles morphology

As typical for the film rehydration method, the samples showed a broad size distribution with vesicle sizes ranging from several micrometers (Figure 50) to 50 nm (LS data). Interestingly vesicles modified with Cu-NTA groups showed identical size distributions. The average size and size distribution was reduced by repeated extrusion through polycarbonate membranes of defined and decreasing pore sizes. After extrusion, the vesicles were characterized by dynamic and static light scattering and small angle x-ray scattering (DLS, SLS and SAXS).

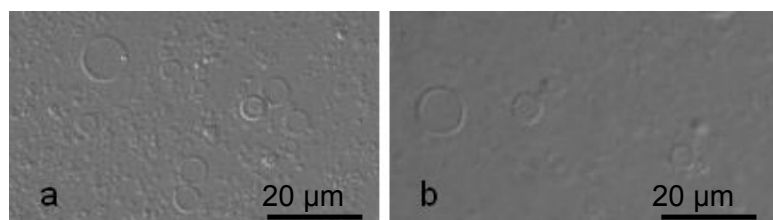


**Figure 50:** Giant vesicles obtained via film rehydration of a) PB<sub>39</sub>-PEO<sub>36</sub>-SA-OH and of b) PB<sub>39</sub>-PEO<sub>36</sub>-SA-OH/PB<sub>39</sub>-PEO<sub>36</sub>-SA-TrisNTA.d-Ni<sup>2+</sup> (10:1). Optical Microscope Leica DMIRE2, with magnification: 20x10. Media: bidistilled water

### 3.2.2.1 Dynamic Light Scattering (DLS) and Temperature Dependence

Dynamic light scattering measurements were performed to determine the hydrodynamic radii of vesicles of PB<sub>60</sub>-PEO<sub>34</sub>-SA-OH/PB<sub>60</sub>-PEO<sub>34</sub>-SA-NTA.d-Cu<sup>2+</sup> (10:1). The intensity and volume weighted size distribution of the aggregates at T = 25°C is shown in Figure 51. It can be seen that the functionalized diblock copolymer forms aggregates with a hydrodynamic radius of  $R_h = 107 \text{ nm}$  and a polydispersity index (PDI) of 0.169.

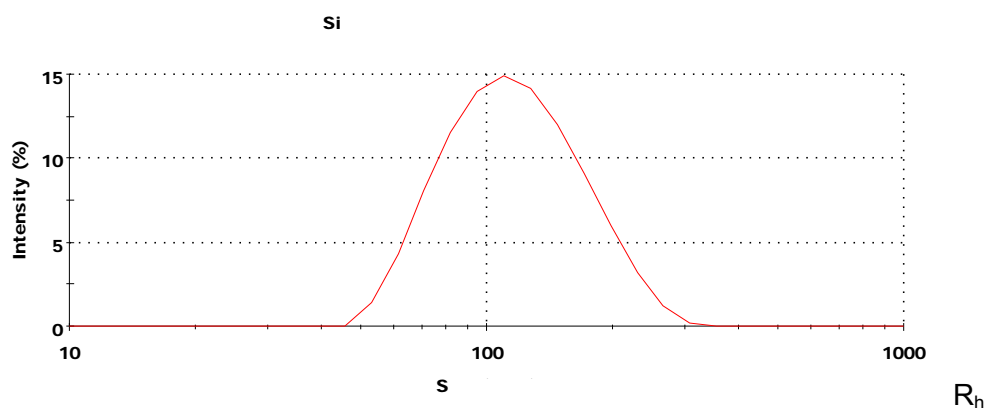


**Figure 51:** Hydrodynamic radii intensity and volume weighted distributions of vesicles made via rehydration of the polymer mixture of PB<sub>60</sub>-PEO<sub>34</sub>-SA-OH/PB<sub>60</sub>-PEO<sub>34</sub>-SA-NTA.d-Cu<sup>2+</sup> (10:1), c (polymer) = 2.2 μM; media: TRIS/HCl buffer pH 8.0

The radii  $R_h$  ( $\sigma R_h = 111 \text{ nm}$ ) were constant within a temperature range from 8°C to 90°C (Figure 52). The polydispersity index<sup>130</sup> of the vesicles was 0.140.

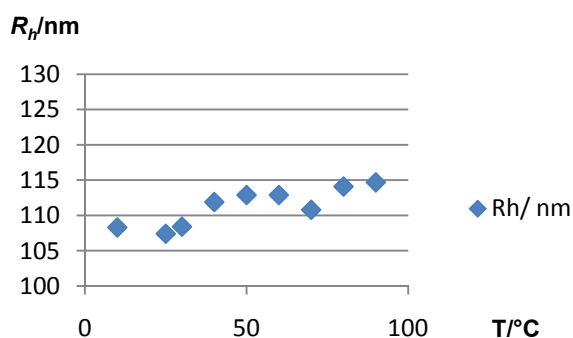


**Figure 52:** Rh versus temperature. Vesicles of PB<sub>60</sub>-PEO<sub>34</sub>-SA-OH/PB<sub>60</sub>-PEO<sub>34</sub>-SA-NTA.d-Cu<sup>2+</sup> (10:1), c (polymer) = 2.2 μM; media: TRIS/HCl buffer pH 8

### 3.2.2.2 Dynamic Light Scattering

DLS measurements showed that extrusion in contrast to a simple filtering led to a monodisperse population of vesicular structures with a hydrodynamic radius of  $118 \pm 9 \text{ nm}$ . Figure 53 shows the DLS autocorrelation function Inverse Laplace transform of PB<sub>60</sub>-PEO<sub>34</sub>-SA-NTA.d-Cu<sup>2+</sup> (10% NTA.d-Cu<sup>2+</sup>) vesicles obtained via film rehydration. Here the

hydrodynamic radius  $R_h$  was **118 nm**, which corresponded to the 200 nm extrusion pore size and the population had a  $PDI$  of 1.08. The small intensity peak (**A**) in Figure 53 b appears at larger dimensions of the hydrodynamic radii and therefore describes a minimum bulk of major aggregates.

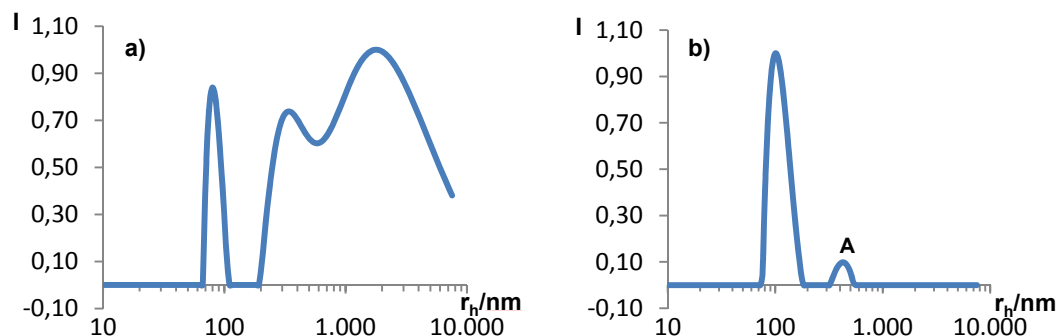


**Figure 53:** PB<sub>60</sub>-PEO<sub>34</sub>-SA-OH/PB<sub>60</sub>-PEO<sub>34</sub>-SA-NTA.d-Cu<sup>2+</sup>, (10:1); c = 22 μM; media: TRIS/HCl buffer pH 8.0, a) Filtered through a 10 μm PC membrane b) Filtered successively through 10 μm and 1 μm and extruded 11× through 0.2 μm PC membranes.

As mentioned above, only the diblock copolymer **PB<sub>60</sub>-PEO<sub>34</sub>-SA-OH** and its functionalized homologue mixtures were used for further investigations. Therefore only this polymer was examined via dynamic light scattering. The temperature dependent DLS measurements (performed with a Zetasizer Nano ZS, Malvern Instruments, UK) as well as the DLS measurements (performed with a commercial goniometer ALV, USA) gave an average hydrodynamic radius  $R_h$  of **112 nm ± 6 nm** which corresponded to the pore size of 200 nm in diameter of the PC membranes (extrusion). Since vesicles can be described as 2-dimensional liquids, it is possible that also hollow spheres with a larger diameter than 200 nm pass through the pore sizes, which is confirmed by the DLS results.

### 3.2.2.3 Static Light Scattering (SLS)

Static light scattering (SLS) was used to get additional structural information like molar mass and shell thickness for the PB<sub>60</sub>-PEO<sub>34</sub>-SA-NTA.d-Cu<sup>2+</sup> containing vesicles. Both quantities can be obtained through a careful form factor analysis since they are directly related to the concentration and angle-dependent scattered light intensity via:<sup>114</sup>

$$\frac{K \cdot C}{R_\theta} = \left( \frac{1}{M_w} + 2 \cdot A_2 \cdot C \right) \cdot \frac{1}{P(q)} \quad (\text{eq. 17})$$

where  $R_\theta$  is the solute Rayleigh ratio ( $\text{m}^{-1}$ ),  $K$  is the contrast factor ( $\text{mol} \cdot \text{m}^2 \cdot \text{g}^{-2}$ ) and  $q = (4\pi n/\lambda) \cdot \sin(\theta/2)$  is the momentum transfer ( $\text{m}^{-1}$ ). Usually the form factor  $P(q)$  is the one for random coils which gives a linear Zimm plot. In this case, due to the size of the vesicles and

the contrast induced by the presence of the metal (refractive index increment of 0.35 g/mL, instead of 0.1 g/mL usually found for polymers), we used a different form factor, for monodisperse vesicles. The dimensionless form factor  $P(q)$  is given for large monodisperse vesicles by:<sup>115</sup>

$$P(q) = \left\{ \frac{3}{U^3 - u^3} [\sin(U) - U \cdot \cos(U) - \sin(u) + u \cdot \cos(u)] \right\}^2 \quad (\text{eq. 18})$$

where  $U = q \cdot R$  and  $u = q \cdot r$  ( $R$  is the outer radius of vesicle, and  $r$  the inner one, respectively). Figure 54 shows a Zimm plot for the  $\text{Cu}^{2+}$ -NTA modified vesicles. Here the normalized inverse scattering ratio ( $K \cdot C/R_\theta$ , mol/g) was fitted as a function of angle ( $\theta$ ) and mass concentration ( $C$ ) with 4 parameters: the outer and the inner radii ( $R$ ,  $r$ ) of the vesicles (and with that, the membrane thickness  $R-r$ ), the weight-average molecular mass ( $M_w$ ) and second virial coefficient ( $A_2$ ) (Figure 54). The vesicles radii polydispersity (as indicated by DLS) caused a slight deviation between the fitting curves curvature and the experimental data.

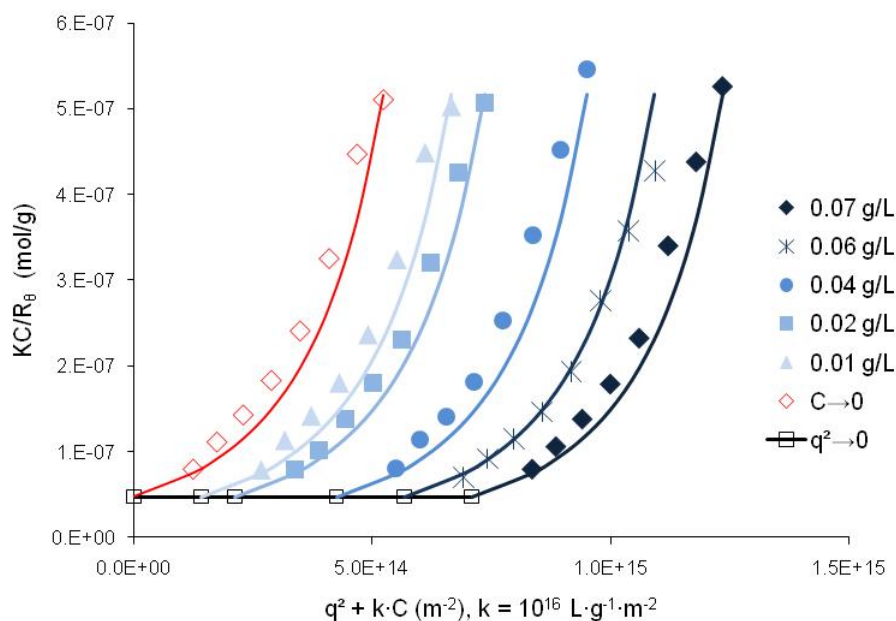


**Figure 54:** Zimm-plot for the  $\text{PB}_{60}\text{-PEO}_{34}$  block copolymer vesicles containing 10 mol% of  $\text{Cu}^{2+}$ -NTA modified polymer. Data were fitted using the vesicle form factor.

The analysis yields  $M_w = 21 \times 10^6 \text{ mol/g} \pm 2 \times 10^6 \text{ mol/g}$  and  $A_2 \approx 0$  within experimental error suggesting that long range interactions between the vesicles are negligible. As the diblock copolymer of the vesicles has a molecular weight of  $M_w = 4357 \text{ g/mol}$ , the average number of polymer molecules per vesicle is calculated to  $N_V \approx 5000$ . This number  $N_V$  relates to vesicles with a diameter of  $d = 200 \text{ nm}$ .

---

The membrane thickness ( $R - r$ ) was estimated to be  $8 \text{ nm} \pm 2 \text{ nm}$ . Cryo-TEM suggested a similar membrane thickness for polymer vesicles formed by a non-functionalized PB-PEO block copolymer with similar molar mass and block length ratio<sup>131</sup>. The outer radius of the vesicles was determined to be  $R = 107 \text{ nm} \pm 10 \text{ nm}$ , in good agreement with the hydrodynamic radius  $R_h$  obtained by DLS. These data showed that within experimental error the presence of the metal-NTA groups did not affect the polymer vesicles morphology.

### 3.2.2.3 Small Angle X-ray Scattering (SAXS)

SAXS experiments on vesicles (PB<sub>60</sub>-PEO<sub>34</sub>-SA-0.1NTA.d-Cu<sup>2+</sup>) solutions were performed to confirm the nature of the created objects. It should be noted that unilamellar vesicles are weak scatterers in SAXS compared to multilamellar vesicles and aligned bilayers. Therefore small-angle neutron scattering is used often for the characterization of vesicles, which allows, in contrast to SAXS, a strong contrast variation.<sup>117</sup> More recently a combined global analysis approach has been introduced<sup>132</sup> to overcome the problem of low SAXS intensities from vesicles. In our case the slit collimation of the compact SAXS system allows to detect a sufficiently intense scattering intensity for a polymer concentration of 1 mM as can be seen in Figure 55 (symbols). The data were approximated and desmeared using the method of the indirect Fourier transformation developed by Glatter<sup>116</sup>, (dashed and solid line in Figure 55). It can be seen in Figure 55 that the desmeared SAXS intensity

scales with  $q^{-2}$  from the lowest  $q$ -value ( $0.04 \text{ nm}^{-1}$ ) to  $0.12 \text{ nm}^{-1}$ . This  $q^{-2}$ -scaling is characteristic for unilamellar vesicles.

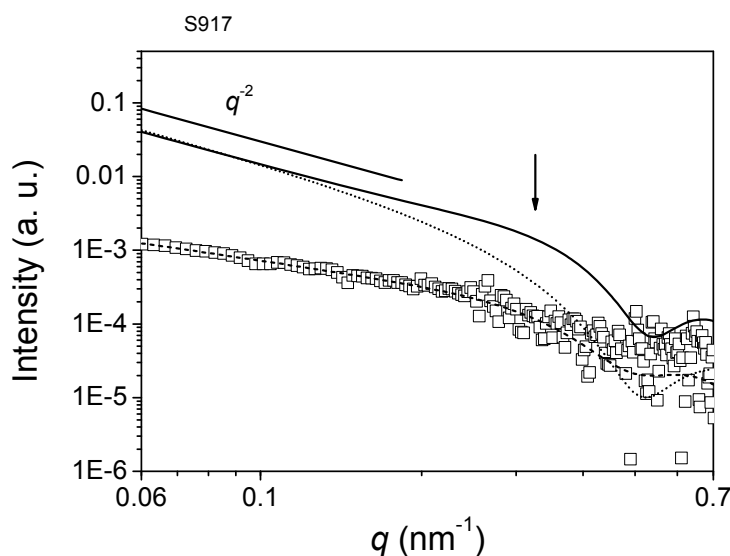


**Figure 55:** Vesicles of PB<sub>60</sub>-PEO<sub>34</sub>-SA-OH/PB<sub>60</sub>-PEO<sub>34</sub>-SA-NTA.d-Cu<sup>2+</sup> (10:1);  $c = 1 \text{ mM}$ ; media: TRIS/HCl buffer pH 8.0; filtered successively through  $10 \mu\text{m}$  &  $1 \mu\text{m}$  and extruded  $11\times$  through  $0.2 \mu\text{m}$  PC membranes. SAXS intensity of the vesicles with a concentration of  $1\text{mM}$  in TRIS/HCl buffer solution (symbols), IFT fit function (dashed line) and the corresponding desmeared intensity (solid line), which takes into account the slit collimation geometry of the SAXS instrument. The model curve (dotted line) corresponds to a simple vesicle with a constant electron density profile in the direction transversal to the vesicle wall (vesicle radius is  $200 \text{ nm}$ , wall thickness  $12.0 \text{ nm}$ ). The arrow at  $q = 0.3 \text{ nm}^{-1}$  indicates the region where the data and the fit curve differ maximally. A slope of  $q^{-2}$  is indicated for comparison to the intensity at low values of  $q$ .

In contrast, compact spheres intensity scales with  $q^{-4}$  and multilamellar vesicles scaling lies between  $q^{-2}$  and  $q^{-4}$ .<sup>133</sup> In addition to the DLS results one concludes that the  $q^{-2}$ -scaling in the low  $q$ -region proves the presence of unilamellar vesicles. It should be mentioned that a Guinier region, which gives the radius of gyration of the whole vesicle, is absent in the SAXS curve due to the large vesicle size. The radius of gyration of a unilamellar vesicle (hollow sphere,  $R_h = 100 \text{ nm}$ , with a shell thickness of ca.  $10 \text{ nm}$ )<sup>116</sup> is  $R_g = 95 \text{ nm}$ . This large value cannot be determined from the SAXS data as the upper  $q$ -value for the determination of the radius of gyration is  $q_{\text{max}} < R_g^{-1}$ . Therefore the upper limit for the  $q$ -region to determine a  $R_g$  of  $100 \text{ nm}$  is about  $0.01 \text{ nm}^{-1}$ . This is outside of the  $q$ -range and the absence of a Guinier region is therefore in agreement with the results from DLS ( $R_h = 100 \text{ nm}$ ).

Wall thickness can be obtained from an approximation of the SAXS curve with a simple core-shell model. The easiest useful model structure is a polydisperse vesicle with a polydisperse core and a constant shell thickness. Bartlett and Ottewill derived the form factor for this model.<sup>134</sup> They describe the polydispersity with a Schulz distribution, which is physically realistic as well as mathematically traceable. The best approximations of this

---

model to our SAXS data result in a shell thickness of about 11 nm (see solid line in Figure 55). Therein fixed values were used for core radius (100 nm, known from DLS) and a polydispersity of  $\lambda = 0.2$ . Model curves with a lower polydispersity than 0.2 produce oscillations in the low  $q$ -region of the data and can therefore be excluded. This is in agreement with the polydispersity index from DLS. When comparing the model curve with the data it can be seen that the characteristic strong decay of the data and simulation is for both at a  $q$ -value of about  $0.4 \text{ nm}^{-1}$ , which indicates that the model is a good approximation on a length scale of about 11 nm. But one finds a systematic higher intensity of the data than in the simulated curve with a maximum deviation around  $0.3 \text{ nm}^{-1}$ . This deviation indicates that the assumption of a constant electron density profile for the shell is only a rough estimation. The total thickness of the wall must be assumed to be larger than 11 nm. Furthermore the density difference between buffer and the inner membrane wall should be of opposite sign than in the outer region of the wall. This resembles to vesicles formed by membrane lipids, for example, dimyristoyl phosphatidyl choline vesicles.<sup>116</sup>

Important characteristics of the vesicle wall can be determined by calculating the cross-sectional density profile,  $\rho(r)$ , from the transversal pair distribution function  $P_t(r)$ .<sup>116</sup> The  $P_t(r)$  has been determined by the IFT method introduced by Glatter<sup>135</sup> and is shown in Figure 56. It can be understood as a distance histogram of the wall in real space. The  $P_t(r)$  of a vesicle wall with a constant density is simply a straight line with a negative slope. Its intersection with the distance axis gives directly the wall diameter. Instead of that simple linear behavior the  $P_t(r)$  shows first an approximately linear decay at small distances (up to 7 nm) but then oscillates around zero. The maximum distance is at about 24 to 30 nm which can be identified as the maximal possible distance between the two sides of the wall. The calculated  $\rho(r)$  (inset of Figure 56) shows that the electron density in the center of the wall is lower than that of the surrounding buffer solution while the outer region has a higher electron density.

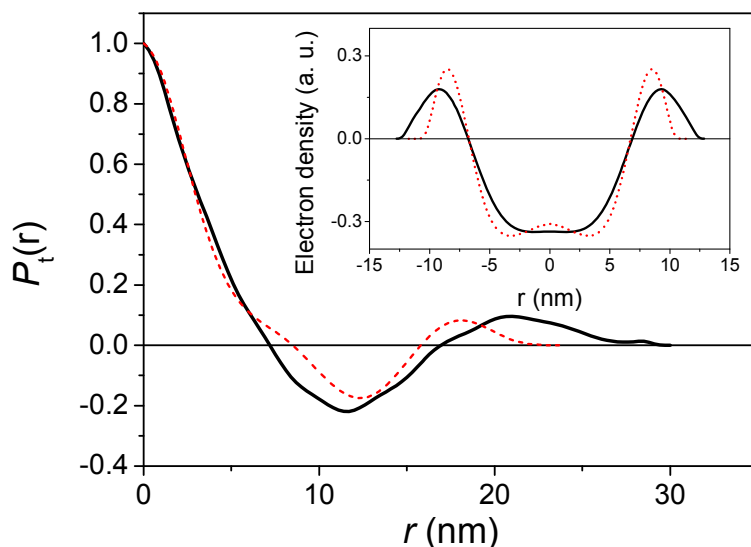


**Figure 56:** Transversal pair distance distribution function  $P_t(r)$ , resulting from the IFT of the desmeared SAXS data. Inset: transversal electron density profile as calculated from the  $P_t(r)$ .

This result was expected due to the characteristic and strong deviation between the curve fit and the data (cf. arrow in Figure 55). A negative excess electron density in the center is in agreement with the molecular structure of the polymer as the center of the vesicle membrane is formed by poly(butadiene) whose density is lower ( $0.892 \text{ g cm}^3$  in an amorphous state)<sup>136</sup> than that of water. A layer containing only poly(butadiene) is in the center ranging from  $-3 \text{ nm}$  to  $3 \text{ nm}$ . This layer is followed by a  $3 \text{ nm}$  to  $4 \text{ nm}$  thick transition layer on both sides where the electron density increases and matches the density of the buffer at  $\pm 7 \text{ nm}$ . Herein poly(butadiene) and poly(ethylene oxide) chains are present. Positive excess electron densities are found in the region of  $\pm (7-12) \text{ nm}$  with maxima at  $\pm 9 \text{ nm}$  from the membrane center. This is in agreement with the assumption that water-swollen poly(ethylene oxide) blocks, containing the complexed copper ions, form the outer regions of the membrane. Such have a higher electron density than water and a layer thickness of  $5 \text{ nm}$ . In summary, the total vesicle wall has a thickness of about  $24 \text{ nm}$ . The electron density in transversal direction to the membrane has a negative excess electron density in the center (inner layer with a thickness of  $14 \text{ nm}$ ). On both sides of this central layer lies a layer with a positive excess electron density with a thickness of  $5 \text{ nm}$ , containing the poly(ethylene oxide) chains and complexed copper ions.

---

### 3.2.3 Metal doped vesicles surface functionality

Immobilization strategies require knowledge of the vesicles dispersion zeta-potential as the surface adsorption is driven by electrostatic interactions. Moreover, it is of interest to determine the actual concentration of metal ( $\text{Ni}^{2+}$ ,  $\text{Cu}^{2+}$ ) exposed on the vesicle surface in the vesicle solution. In order to calculate the fraction of bound protein it is assumed that around 50 % of the overall metal ( $\text{Ni}^{2+}$ ,  $\text{Cu}^{2+}$ ) groups are exposed on the outer surface of the vesicle, due to the statistic character of self-assembly process of vesicle formation.

#### 3.2.3.1 Vesicle zeta potential

Zeta-potential measurements indicate that polymer dispersions (vesicles of  $\text{PB}_{60}\text{-PEO}_{34}\text{-SA-OH/PB}_{60}\text{-PEO}_{34}\text{-SA-NTA.d-Ni}^{2+}$ , 10:1,  $c = 800 \mu\text{M}$ ), extruded through 0.05  $\mu\text{m}$ ; 0.2  $\mu\text{m}$ ; 1  $\mu\text{m}$  and 5  $\mu\text{m}$  PC-membranes, in phosphate buffer pH 7.4 have a negative surface potential between -22 and -34 mV, whereas vesicles with a 1  $\mu\text{m}$  cut-off diameter show the most negative zeta-potential (Figure 57). The general curve progression (green curve in Figure 57) indicates an increasing zeta-potential with an increasing pore sizes of the membranes and therefore with increasing radii of the vesicles.

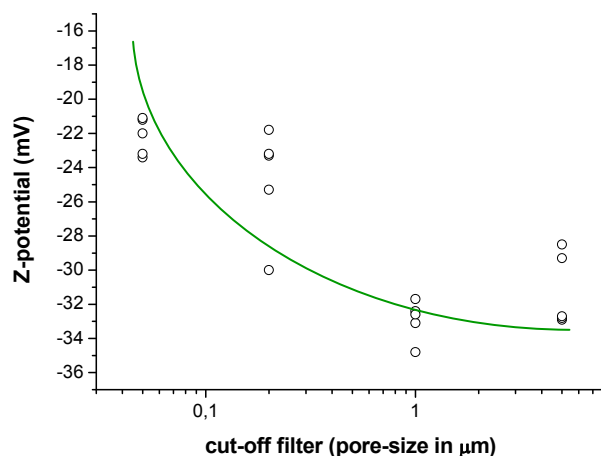


**Figure 57:** Zeta-potential of  $\text{PB}_{60}\text{-PEO}_{34}\text{-SA-OH/PB}_{60}\text{-PEO}_{34}\text{-SA-NTA.d-Ni}^{2+}$ , (10:1) dispersions,  $c = 800 \mu\text{M}$  in PBS pH 7.4. All results correspond to non-diluted and extruded samples.

The major the radii, the higher are the negative charges on the membranes. In conclusion, membranes with less curvature favor a surface geometry which decreases the electrostatic repulsive forces on its surface. Therefore more charged groups can be placed on flat surface structures.

$\text{Ni}^{2+}$ -content dependent zeta-potential measurements indicate that the polymer vesicle dispersions of the mixtures  $\text{PB}_{60}\text{-PB}_{34}\text{-SA-OH/PB}_{60}\text{-PB}_{34}\text{-SA-NTA.d-Ni}^{2+}$ , extruded through a

PC-membrane 0.2µm in diameter, in phosphate buffer pH 7.4 had negative surface potentials of  $-30.1 \pm 0.7$  mV,  $-26.2 \pm 0.6$  mV and  $-24.1 \pm 0.5$  mV for 0, 10 and 100% of PB<sub>60</sub>-PB<sub>34</sub>-SA-NTA.d-Ni<sup>2+</sup>, respectively (Table 4). The values did not vary in a great extent with the Ni-NTA content, indicating that the zeta potential is determined by negative charges on the vesicle surfaces that appear to be equal in all cases. In the case of PB<sub>60</sub>-PB<sub>34</sub>-SA-OH vesicles (0% Ni-NTA), each polymer end possesses a carboxylic group, which can be deprotonated at pH = 7.4 (pK~4.16)<sup>137</sup> and contributes with one negative charge. In the case of PB<sub>60</sub>-PB<sub>34</sub>-SA-NTA.d-Ni<sup>2+</sup> vesicles (100%Ni-NTA) each molecule also contributes with a net negative charge (see Figure 32, 13a).

**Table 4:** Zeta-potential and diameter of extruded (0.2 µm pore size) polymer dispersions of a mixture of PB<sub>60</sub>-PB<sub>34</sub>-SA-OH /PB<sub>60</sub>-PB<sub>34</sub>-SA-NTA.d-Ni<sup>2+</sup>, (10:1) dispersions in phosphate buffer. All results correspond to non-diluted, 0.2 µm extruded samples.

% Ni-NTA	Zeta-potential (mV)
0	$-30.1 \pm 0.7$
10	$-26.2 \pm 0.6$
100	$-24.1 \pm 0.5$

### 3.2.3.2 Metal content determined by Inductive Coupled Plasma Atom Emission Spectroscopy (ICP-AES)

Total nickel(II) and copper(II) contents in the metal-doped vesicle solutions were determined with Inductive Coupled Plasma Atom Emission Spectroscopy, see Table 5. The theoretical maximum content of metal in the probes (metal-doped vesicle solution) was  $c_{max}$  in mg/L. The metal doped fraction (%) was calculated on  $c_{measured}/c_{max} \times 100\%$ .

**Table 5:** The amount of actual complexed metal in different media after filtration or extrusion.

probe	matrix	cation	$c_{max}/$ (mg/L)	$c_{measured}/$ (mg/L)	%
<b>PB<sub>60</sub>PEO<sub>34</sub>-SA-NTA.d-10%Cu</b> c = 222µM; filtered 10µm	TRIS pH 8.0	Cu <sup>2+</sup>	1,4	0,56	40
<b>PB<sub>60</sub>PEO<sub>34</sub>-SA-NTA.d-10%Cu</b> c = 222µM; extruded 0.2µm	TRIS pH 8.0	Cu <sup>2+</sup>	1,4	0,41	30
<b>PB<sub>60</sub>PEO<sub>34</sub>-SA-NTA.d-3%Ni</b> c = 2mM; extruded 0.2µm	TRIS pH 8.0	Ni <sup>2+</sup>	3,5	0,16	5
<b>PB<sub>60</sub>PEO<sub>34</sub>-SA-NTA.d-3%Ni</b> c = 2mM; extruded 0.2µm	PBS pH 7.4	Ni <sup>2+</sup>	3,5	0,21	6

The copper doped fraction was 40 % when the vesicles solution was filtered (1×) through a 10 µm cut off PC membrane and 30 % when the vesicles solution was extruded

---

(11×) through a 0.2 μm cut off PC membrane. All fractions were in TRIS buffer pH 8.0. The nickel doped fraction was 5 % when the vesicles solution was extruded (11×) through a 0.2 μm cut off PC membrane, both in PBS pH 7.4 and TRIS pH 8.0. However, in all cases a certain amount of polymer and polymer functionalized with nickel and copper were lost due to the extrusion process. After the extrusion, polymer was found remaining in the PC membranes indicating that the rehydration, especially at higher polymer concentrations ( $c \geq 100 \mu\text{M}$ ), is not a quantitative process and produces, beside the vesicles, more than 50% of aggregates.

### 3.2.4 Vesicle Adsorption on Surfaces

Quartz Crystal Microbalance (QCM): The zeta-potential of the polymer aggregates determined the strategy for surface immobilization. Thus, electrostatic forces between the negatively charged polymer structures and a positively charged surface were used. Atomic force microscopy was used to morphologically characterize the adsorbed vesicles on polyelectrolyte coated substrates.

#### 3.2.4.1 QCM: graphs

In order to check if vesicles were adsorbed on polyelectrolyte substrates, preliminary QCM studies with 10% Ni-NTA-polymer were performed. Vesicles ( $\text{PB}_{39}\text{-PEO}_{36}\text{-SA-TrisNTA.d-Ni}^{2+}$ ) were extruded using different cut-off filters and at different concentrations. Figure 58 shows the variation of the vibration frequency (5<sup>th</sup> overtone) and dissipation of a bare and a PEI-coated  $\text{SiO}_2$ -quartz sensor with time as both sensors were flushed with a 100 μM polymer dispersion filtered through 5μm cut-off membranes.

On the bare sensor (dash line), no noticeable adsorption took place; however a significant variation in both frequency and dissipation was detected on the PEI-coated sensor (continuous line). This reveals that adsorption occurred mainly via electrostatic forces induced between the negatively charged polymer structures (vesicles) and the positively charged substrate. This adsorption is irreversible, since no desorption (i.e., an increase of frequency) was detected upon rinsing.

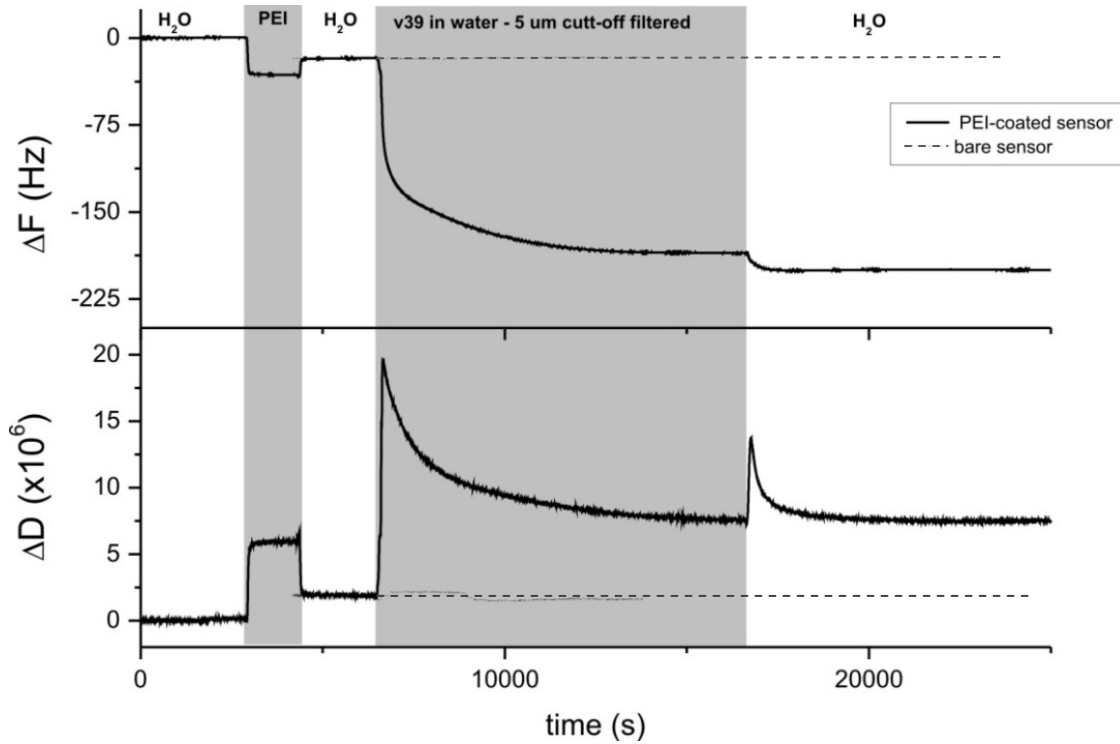


**Figure 58:** QCM-D. Real time changes in frequency and in dissipation (5th overtone) upon adsorption of a polymer dispersion ( $\text{PB}_{39}\text{-PEO}_{36}\text{-SA-TrisNTA.d-Ni}^{2+}$ , 100  $\mu\text{M}$ , 5 $\mu\text{m}$  cut-off filtered) on vibrating  $\text{SiO}_2$ -coated quartz sensors in water. The dashed line represents the time evolution of a bare sensor upon which no adsorption occurs when placed in the polymer dispersion. The continuous line shows the time evolution of a sensor first in PEI-containing solution and secondly in the polymer dispersion once it was rinsed with water.

Table 6 shows the frequency changes induced by the polymer vesicles ( $\text{PB}_{39}\text{-PEO}_{36}\text{-SA-TrisNTA.d-Ni}^{2+}$ ) in dependence on their concentrations and pore sizes. The vesicles solutions were filtered through (PC membranes, pore sizes: 0.05  $\mu\text{m}$  to 5  $\mu\text{m}$  in diameter). The overall frequency change ( $\Delta F$ , Table 6) detected, is indicative of the extent of adsorption.<sup>138</sup> In particular, the mass of adsorbed vesicles per unit area,  $\sigma_m$ , can be estimated from  $\Delta F$  using the Sauerbrey equation,<sup>120</sup> providing the overall change in dissipation ( $\Delta D$ ) is negligible compared to  $\Delta F$  ( $\Delta D/\Delta F < 0.2 \cdot 10^{-6} \text{ Hz}^{-1}$ )<sup>139</sup>:

$$\Delta\sigma_m = \frac{\Delta m}{a} = -\frac{C}{n} \Delta f \quad (\text{eq. 19})$$

where  $a$  is the sensor area,  $C = 17.7 \text{ ng/cm}^2\text{Hz}$  for a 5 MHz resonating quartz sensor and  $n$  is the overtone number. The data fulfilled the condition to apply Sauerbrey equation ( $\Delta D/\Delta F = 0.03\text{-}0.001 \cdot 10^{-6} \text{ Hz}^{-1}$ ) and we correspondingly calculated the adsorbed mass per unit area, which is shown in Table 6 for different cut-offs and concentrations. The results show that the amount of mass adsorbed per unit area increased slightly with increasing the concentrations, whereas the increase of mass for the last two protein solutions (100  $\mu\text{M}$  →

400  $\mu\text{M}$ ) was much lower than for the first two solutions (50  $\mu\text{M}$   $\rightarrow$  100  $\mu\text{M}$ ), which means that maximum adsorption was attained.

**Table 6:** Frequency changes ( $\Delta F$ ) for the different concentrations and cut-offs of vesicles (PB<sub>39</sub>-PEO<sub>36</sub>-SA-TrisNTA.d-Ni<sup>2+</sup>) used in this study.  $\Delta F$  was obtained by subtracting the QCM-D frequency signal before and after the vesicle injection.  $\Delta\sigma_m$  is calculated from  $\Delta F$  using the Sauerbrey equation.

Cut-off [c]	5 $\mu\text{m}$		2 $\mu\text{m}$		0.05 $\mu\text{m}$	
	$\Delta F$ (Hz)	$\Delta\sigma_m$ (ng/cm <sup>2</sup> )	$\Delta F$ (Hz)	$\Delta\sigma_m$ (ng/cm <sup>2</sup> )	$\Delta F$ (Hz)	$\Delta\sigma_m$ (ng/cm <sup>2</sup> )
50 $\mu\text{M}$	142 $\pm$ 5	2513 $\pm$ 89	103 $\pm$ 4	1823 $\pm$ 71	103 $\pm$ 4	1823 $\pm$ 71
100 $\mu\text{M}$	188 $\pm$ 7	3328 $\pm$ 124	124 $\pm$ 4	2195 $\pm$ 71	107 $\pm$ 6	1894 $\pm$ 106
400 $\mu\text{M}$	196 $\pm$ 5	3469 $\pm$ 89	110 $\pm$ 4	1947 $\pm$ 71	122 $\pm$ 11	2159 $\pm$ 195

The adsorption of mass per unit area is for the 5  $\mu\text{m}$  pore size fraction bigger than for the nearly identical mass adsorptions for the 2  $\mu\text{m}$  and 0.05  $\mu\text{m}$  pore size fractions.

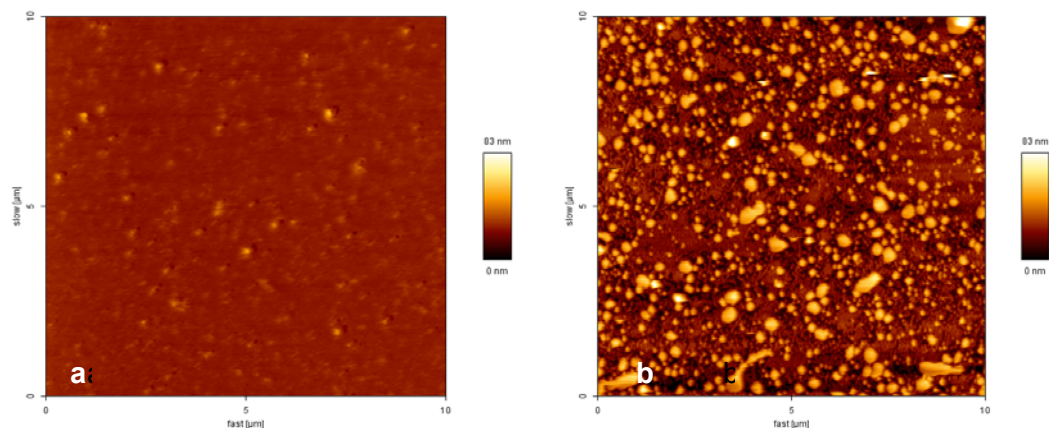
Assuming that a vesicle fraction is homogeneous (e.g. 5  $\mu\text{m}$ ) and that all vesicles have the density of water (1g/cm<sup>3</sup>), the number of vesicles per area unit ( $N_{cm^2}$ ) was calculated. Additionally, the number of polymer molecules per vesicle ( $N_v$ ) was calculated by the assumption that a vesicle with a diameter of 0.2  $\mu\text{m}$  consists of 5000 molecules (see SLS data) and that an increase or decrease of the surface is proportional to  $d^2$ . The increasing number of molecules per vesicle is directly proportional to the increase of the vesicle surface. With these two data ( $N_{cm^2}$  and  $N_v$ ) the number of moles per area unit ( $n/\text{cm}^2$ ) was calculated. The data are presented in Table 7.

**Table 7:** The vesicles per area unit ( $N_{cm^2}$ ) and the number of macromolecules per vesicle ( $N_v$ ) dependent on the diameter  $d$  of the vesicles. The number of moles was calculated as follows:  $n/\text{cm}^2 = (N_v/N_A) \cdot N_{cm^2}$

	5 $\mu\text{m}$	2 $\mu\text{m}$	0.2 $\mu\text{m}$	0.05 $\mu\text{m}$
$N_{cm^2}$	52000	493000	-	32 $\cdot$ 10 <sup>9</sup>
$N_v$	3.13 $\cdot$ 10 <sup>6</sup>	500000	5000	313
$n/\text{cm}^2$ in mol/cm <sup>2</sup>	2.7 $\cdot$ 10 <sup>-13</sup>	4.1 $\cdot$ 10 <sup>-13</sup>	-	1,7 $\cdot$ 10 <sup>-11</sup>

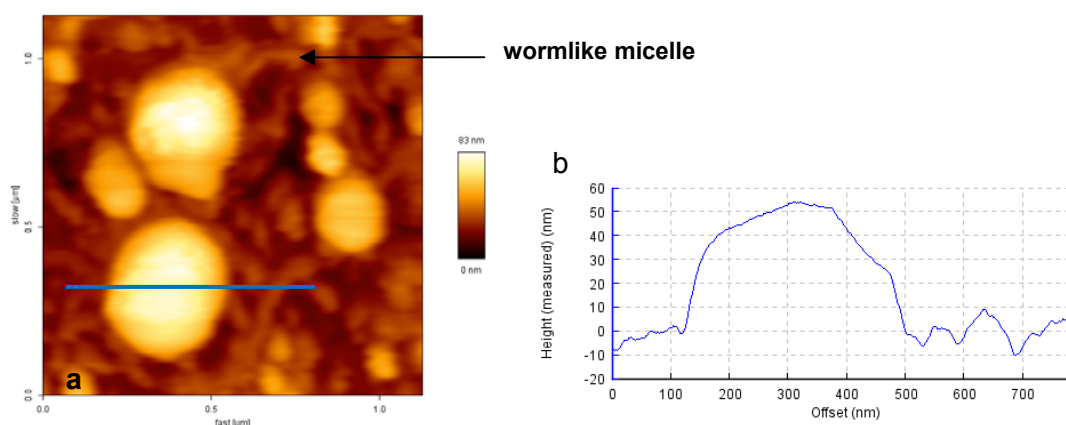
### 3.2.4.2 AFM imaging

Figure 59 shows the time-dependent adsorption of a vesicle solution ( $\text{PB}_{39}\text{-PEO}_{36}\text{-SA-0.1TrisNTA.d-Ni}^{2+}$ ) onto a PEI coated glass coverslip. Figure 59a shows the pure PEI coated coverslip and Figure 59b shows the coverslip covered with vesicles 90 min after injection.



**Figure 59:** AFM a) PEI coated coverslip; b) vesicle solution ( $\text{PB}_{39}\text{-PEO}_{36}\text{-SA-TrisNTA.d-Ni}^{2+}$ , 10:1,  $c = 100 \mu\text{M}$ ,  $2\mu\text{m}$  cut off) on PEI coated coverslip in water (90 min after injection).

Figure 60 shows the adsorption of the vesicles ( $\text{PB}_{39}\text{-PEO}_{36}\text{-SA-OH/0.1PB}_{39}\text{-PEO}_{36}\text{-SA-TrisNTA.d-Ni}^{2+}$ ) on a PEI coated coverslip 2 hours after injection of the vesicle solution. The vesicles can be observed very clearly distributed within smaller aggregates being most likely wormlike micelles.



**Figure 60:** AFM: a) Zoom in: Vesicles solution ( $\text{PB}_{39}\text{-PEO}_{36}\text{-SA-TrisNTA.d-Ni}^{2+}$ , 10:1,  $c = 100 \mu\text{M}$ ,  $2\mu\text{m}$  cut off) on PEI coated coverslip in water; b) Vesicle height profile.

Figure 61 shows a topography image of  $\text{PB}_{60}\text{-PEO}_{34}\text{-SA-0.1NTA-Ni}^{2+}$  vesicles in phosphate buffer pH 7.4. Spherical like objects could be seen all over the imaged region. From height profiles, both the object height and diameter at half height can be determined, leading ultimately to height and diameter histograms (Figure 61b and Figure 61c

respectively) and to correspondingly average morphological parameters. From these histograms a mean diameter of  $401 \pm 53$  nm and a mean height of  $130 \pm 25$  nm were obtained from single-Gaussian fittings. For perfect spheres, the height to diameter ratio should be 1, however in this case it is 0.3, an indication of vesicle flattening. If as a consequence from the adsorption, deformation of the spherical vesicles took place without volume loss, the vesicles dispersed in solution would have an equivalent diameter of  $280 \pm 62$  nm (histogram of  $D_{\text{calc}}$  in Figure 61d). This is in agreement with the sizes measured for the free vesicles in solution by DLS with a diameter of  $224 \text{ nm} \pm 12 \text{ nm}$ .

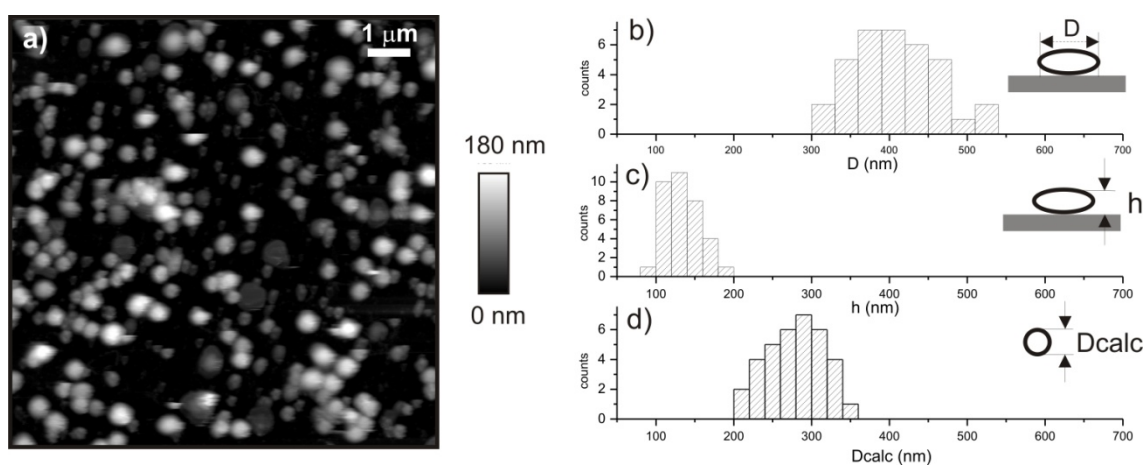


**Figure 61:** a) AFM height image obtained in intermittent contact mode of  $\text{PB}_{60}\text{-PEO}_{34}\text{-SA-0.1NTA-Ni}^{2+}$  vesicles of  $100 \mu\text{M}$  on PEI coated coverslips. From height profiles, heights and diameters of the adsorbed round objects were measured and plotted as histograms of diameter,  $D$  b) and height,  $h$  c). A histogram of the equivalent diameter is shown d) if deformation of the spherical vesicles took place without loss of volume.

### 3.2.5 Protein binding to functionalized vesicles

In order to test the functionality of  $\text{NTA-Ni}^{2+}$  and  $\text{NTA-Cu}^{2+}$  containing vesicles, the vesicle solutions were mixed with the fluorescent proteins: a histidine tagged maltose binding protein with a fluorophore (His<sub>10</sub>-MBP-fluorophore), a His-tag enhanced green fluorescent protein (His<sub>6</sub>-EGFP) and a His-tag enhanced yellow fluorescent protein (His<sub>6</sub>-EYFP). The attached histidines are reported to bind selectively to the  $\text{NTA-Ni}^{2+}$ - or  $\text{NTA-Cu}^{2+}$ -complexes.<sup>14</sup> These proteins are quite robust in different media and environment. Moreover, their fluorescence allows the functionalized vesicles to be observed *in situ*.

#### 3.2.5.1 Confocal Fluorescence Microscopy: “rings” in solution

In order to visualize the protein-vesicle conjugates, a solution of GUVs ( $\text{PB}_{60}\text{-PEO}_{34}\text{-SA-OH / PB}_{60}\text{-PEO}_{34}\text{-SA-NTA.d-Ni}^{2+}$  10:1,  $c = 200 \mu\text{M}$ ,  $V = 1 \text{ mL}$ , in PBS buffer pH 7.4,

---

diameter of 1 - 5  $\mu\text{m}$ ) formed by the rehydration method was mixed with one drop of His<sub>6</sub>-EYFP solution ( $c = \text{ca. } 1.5\text{mg/mL}$ , in MilliQ-water). After 1 h of slightly stirring at room temperature, the sample was observed with the confocal fluorescent microscope. The images present GUVs with a yellow corona, thus indicating that His<sub>6</sub>-EYFP is bound to the metal-groups at the vesicles surface (Figure 62).

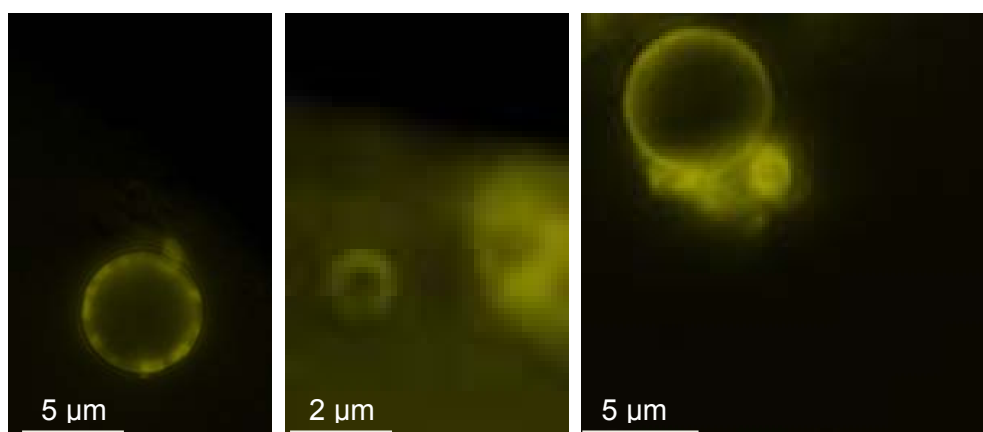


**Figure 62:** Vesicle (PB<sub>60</sub>-PEO<sub>34</sub>-SA-0.1NTA.d-Ni<sup>2+</sup>) solution,  $c = 200 \mu\text{M}$ , PBS pH 7.4 + His<sub>6</sub>-EYFP (1.5 mg/mL).

In the same manner a drop of His<sub>6</sub>-EGFP solution ( $c = 1.2 \text{ mg/mL}$ , in MilliQ-water) was added to a vesicles solution of PB<sub>60</sub>-PEO<sub>34</sub>-SA-OH/0.1PB<sub>60</sub>-PEO<sub>34</sub>-SA-NTA.d-Ni<sup>2+</sup> ( $c = 200 \mu\text{M}$ ,  $V = 1 \text{ mL}$ , in PBS buffer pH 7.4). After 1 h of slightly stirring at room temperature, one drop of the vesicle solution with protein + one drop of 1mM NiSO<sub>4</sub> solution were mixed and observed with the fluorescent microscope. The images present GUVs with a green corona, thus indicating that His<sub>6</sub>-EGFP is bound to the metal-groups at the vesicles surface (Figure 63) in good agreement with the FCS results.

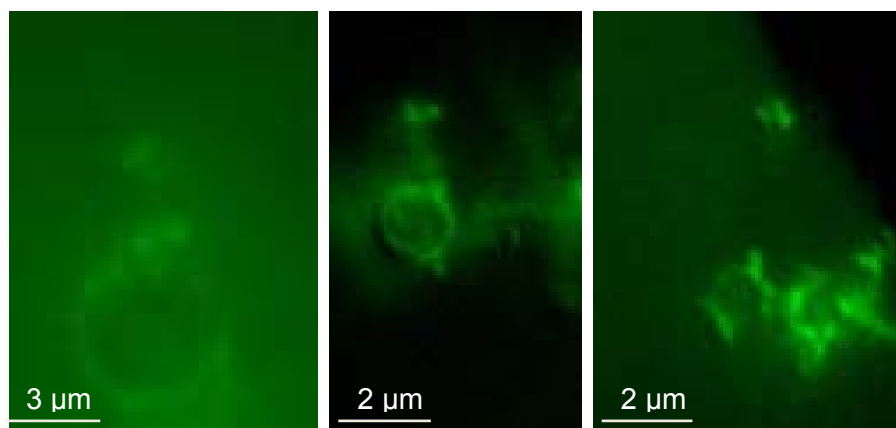


**Figure 63:** Vesicle (PB<sub>60</sub>-PEO<sub>34</sub>-SA-0.1NTA.d-Ni<sup>2+</sup>) solution,  $c = 200 \mu\text{M}$ , PBS pH 7.4 + His<sub>6</sub>-EGFP (1.2 mg/mL) + NiSO<sub>4</sub> (1 mM in Milli-Qwater).

---

Using the His<sub>6</sub>-EGFP protein, it was necessary to add Ni<sup>2+</sup>-ions to obtain visible fluorescent GUVs under the microscope. Obviously His<sub>6</sub>-EGFP needed a higher concentration of the Nickel salt to bind numerous to the Ni<sup>2+</sup>-NTA-groups of the outer vesicles surfaces. This may be due to the impurities (imidazol) of the protein solution. The increase of salt concentration in the vesicles solution led to the destruction of the vesicles due to the change of the osmotic pressure. Since the collapsing of the vesicles lasted, some remaining vesicles could be observed binding to his tagged proteins as shown in Figure 63.

### **3.2.5.2 Fluorescence Correlation Spectroscopy (FCS): His-tag protein binding to the surface of the copolymer vesicles**

To test the binding of His-tagged proteins to the surface of the metal-NTA functionalized vesicles we used a maltose binding protein labeled with fluorescein (His<sub>10</sub>-MBP-FITC) and a His-tagged enhanced green fluorescent protein (His<sub>6</sub>-EGFP) as model systems. The binding affinity was quantified by fluorescence correlation spectroscopy (FCS). In the experiment the size difference between the free protein (His<sub>10</sub>-MBP-FITC or His<sub>6</sub>-EGFP) and the protein-bound to the surface of a metal-doped vesicle with dimensions >100 nm should allow us to differentiate between these two states.<sup>14</sup> Figure 64 presents the results of His<sub>10</sub>-MBP-FITC added to a solution of PB<sub>60</sub>-PEO<sub>34</sub>-SA-OH/ PB<sub>60</sub>-PEO<sub>34</sub>-SA-NTA-Ni<sup>II</sup> (10:1) vesicles, with a concentration of Ni<sup>2+</sup> 2 μM; the autocorrelation amplitudes were normalized to 2 to compare the curve's shapes and thus diffusion times. Multiphasic curve's shapes suggest the presence of more than one diffusing species in a sample for diffusion coefficients being sufficiently different.<sup>140</sup> The free protein diffusion time of His<sub>10</sub>-MBP-FITC is  $\tau_d = 64 \mu s$  (Figure 64, curve a), which corresponds to a hydrodynamic radius of 2.1 nm. This is in good agreement with the calculated radius of 2.4 nm, on the basis of the molecular mass of labeled-MBP (43.6 kDa). When His<sub>10</sub>-MBP-FITC (30 nM) was added to a solution of PB<sub>60</sub>-PEO<sub>34</sub>-SA-OH/0.1PB<sub>60</sub>-PEO<sub>34</sub>-SA-NTA-Ni<sup>2+</sup> vesicles, with a Ni<sup>2+</sup> concentration of 2 μM, a different autocorrelation function was obtained (Figure 64, curve b).

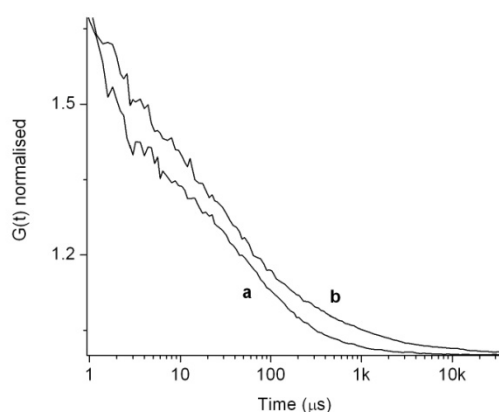


**Figure 64:** Fluorescence autocorrelation function  $G(t)$  of: a) free His<sub>10</sub>-MBP-FITC protein (30 nM), and b) when His<sub>10</sub>-MBP-FITC is added to a solution of PB<sub>39</sub>-PEO<sub>36</sub>-SA-OH/0.1PB<sub>39</sub>-PEO<sub>36</sub>-SA-TrisNTA-Ni<sup>2+</sup> vesicles (2µM of Ni<sup>2+</sup>).

The best fit of the time-dependent fluorescence signal shown in Figure 64 is obtained from a two-component model by taking into account the differences in the fluorescence quantum yield of bound and free protein.<sup>14</sup> The fit of the autocorrelation function indicates the presence of the free protein, as the major component, together with a second particle population (around 15%) with a considerably longer diffusion time ( $\tau_d = 5.5 \pm 0.5$  ms). The second population represents the fraction of His<sub>10</sub>-MBP-FITC bounded to the Ni-doped vesicles surface, as the hydrodynamic radius calculated using the diffusion time  $\tau_d$  is similar to that determined by DLS experiment. In addition, the diffusion time is similar to the values obtained for other block copolymer vesicles.<sup>89</sup> When His<sub>6</sub>-EGFP was used together with Ni(II)- or Cu(II)-NTA-vesicles, the autocorrelation function fit indicated that the second particle population has a similar value with a diffusion time of  $\tau_d = 4.8 \pm 0.5$  ms.

To determine the dissociation constant  $K_D$  of the His-tag/Ni<sup>2+</sup>NTA interaction at the vesicle surface, we titrated His<sub>10</sub>-MBP-FITC and His<sub>6</sub>-EGFP with increasing concentrations of Ni<sup>2+</sup>-doped-vesicles (PB<sub>39</sub>-PEO<sub>36</sub>-SA-OH/PB<sub>39</sub>-PEO<sub>36</sub>-SA-TrisNTA-Ni<sup>2+</sup> (10:1) vesicles). The content of Ni<sup>2+</sup> varied from 0.5 to 16 µM. To avoid errors due to the loss of the modified polymers during the preparation procedure (e.g. adsorption to the filter in the extrusion step), we determined the concentration of the Ni<sup>2+</sup>-NTA groups in the vesicle dispersions by inductive coupled plasma (ICP) atom emission spectroscopy. Due to the statistical character of the self-assembly process of vesicles formation, we assumed for our calculations that 50 % of the overall Ni<sup>2+</sup>-NTA groups are exposed on the outer surface of the vesicles and, hence, accessible to the His-tagged proteins. The fluorescence autocorrelation functions were normalized to an equal number of molecules in the confocal volume. For each metal concentration, the fraction of the vesicle surface bound protein was

calculated by a two-component fit of the autocorrelation function of the time-dependent fluorescence signal,  $G(t)$ , indicating that there are two populations of molecules: the free protein, and a second population, with a big diffusion time, representative of the protein-vesicle population (see Figure 64, for the case when the content of Ni(II) at the outer vesicles surface is  $2\mu\text{M}$ ). The fraction of protein-bound vesicles requires corrections as fluorescence quantum yield of bound and free protein are different, simply using eq. 20<sup>14</sup>:

$$c = \frac{F}{F + \alpha^2 - F\alpha^2} \quad (\text{eq. 20})$$

where  $c$  corresponds to the corrected fraction of vesicle-bound protein,  $F$  stands for the measured fraction of vesicle-bound protein, and  $\alpha$  is the ratio of counts per molecules (cpm) in the free and bound state, respectively (in this experiment the calculated  $\alpha$  is 0.64 for Ni(II) doped vesicles, and 0.68 for Cu doped-vesicles, respectively).

The fraction of the protein-bound vesicles was plotted against the metal content (Figure 65), and the data were fitted by a Langmuir isotherm model, as previously performed for  $\text{Ni}^{2+}$ -NTA functionalised liposomes<sup>14</sup>.

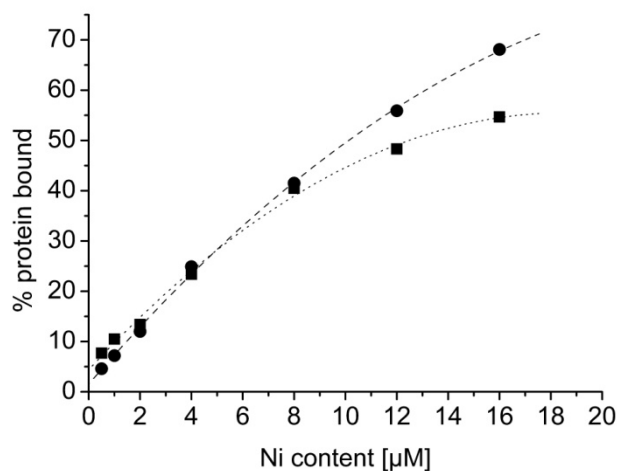


**Figure 65:** Fraction of bound protein versus the Ni(II) content at the outer vesicles surface (PB<sub>39</sub>-PEO<sub>36</sub>-SA-OH/0.1PB<sub>39</sub>-PEO<sub>36</sub>-SA-NTA-Ni<sup>2+</sup> vesicles). Black squares: His<sub>10</sub>-MBP-FITC (30 nM) in PBS, black circles: His<sub>6</sub>-EGFP (20 nM), in PBS.

For His<sub>10</sub>-MBP-FITC we determined the dissociation constant  $K_D$  to be  $K_D = 7.0 \pm 1.2 \mu\text{M}$ , while for His<sub>6</sub>-EGFP we obtained  $K_D = 12.3 \pm 1.2 \mu\text{M}$ . These values have the same order of magnitude as obtained with Ni<sup>2+</sup>-NTA functionalized liposomes ( $K_D = 4.3 \mu\text{M}$ )<sup>14</sup>. The slightly higher dissociation constants of the block copolymer vesicles are presumably a result of steric hindrance due to the PEO brushes at the vesicle surface that surround the individual binding sites. This will be investigated in future experiments by mixing the Ni<sup>2+</sup>-

---

NTA modified polymers with non-functionalized PB-PEO block copolymers having different PEO chain lengths. It should be noted that control measurements with vesicles without NTA-Ni<sup>2+</sup> groups showed less than 3% of protein binding. This clearly shows that under the experimental conditions non-specific protein adsorption to the PEO brushes at the vesicle surface is negligible.<sup>54</sup>

Different buffers composition effects on the protein binding efficiency were determined by comparing the fraction of protein-vesicle conjugates in PBS and TRIS buffers. For both metal-doped polymer vesicles (PB<sub>60</sub>-PEO<sub>34</sub>-SA-0.1NTA-Ni<sup>2+</sup> & PB<sub>39</sub>-PEO<sub>36</sub>-SA-0.1TrisNTA.d-Ni<sup>2+</sup>), the fraction of protein-vesicle conjugates was significantly higher in PBS buffer compared to the TRIS buffer. Even if this effect was more pronounced for copper-doped vesicles than for the nickel-doped ones, in a given buffer both types of metal-functionalized vesicle protein conjugates were comparable in their binding affinity. We assume that in the case of TRIS (Tris(Hydroxymethyl) aminomethane) buffer there is a competition between the protein and the buffer molecules to access the metal site. In contrast, PBS buffer does not have this effect.

### **3.2.5.3 Quartz Crystal Microbalance (QCM): Protein binding to the vesicles**

Quartz crystal microbalance was used to demonstrate the potential of the polymer vesicles to bind to oligohistidines. Thus, we performed three consecutive experiments where vesicle adsorption was followed by incubation with NiCl<sub>2</sub> and ultimately by incubation with His-Tag-EGFP.

Figure 66 a shows the control experiment where polymer vesicles containing no NTA groups were adsorbed on PEI coated sensors and subsequently incubated with protein. No protein adsorption was detected. As proteins adsorb immediately on poly(ethylene imine), a positively charged macromolecule, and no adsorption was detected, we conclude that the non functionalized vesicles formed a dense layer on the PEI covered surface impeding the proteins to adsorb on the vesicles' surfaces.

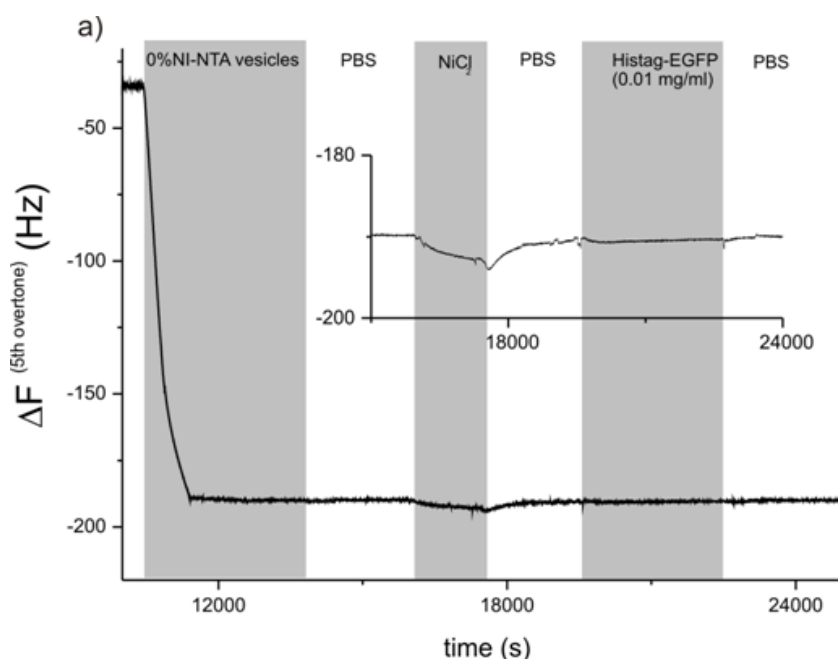


**Figure 66: a)** Polymer vesicles of  $PB_{60}$ - $PEO_{34}$ -SA-OH with no NTA groups were incubated in His<sub>6</sub>-EGFP. No adsorption was detected (control experiment).

However, the same experiment with 10%  $Ni^{2+}$ -NTA functionalized vesicles showed changes of 3 Hz and 7 Hz in the frequency upon injection of protein containing solution of concentrations of 0.01 mg/mL and 0.03 mg/mL, respectively, shown in Figure 67. These changes are indicative for material incorporation on the vesicles, and together with the fact that they scaled with the protein concentration, point out towards protein adsorption. After signal stabilization, the surfaces were rinsed with phosphate buffer; the frequency signal did not alter, meaning that the protein was not desorbed after washing.

Although the changes in the frequency upon injection may be described as subtle, they are evident and quantitative as the frequency change for the less concentrated protein solution (0.01mg/mL) was determined to be 3 Hz and for the more concentrated protein solution (0.03 mg/mL) to be 7 Hz. These results indicate clearly that protein adsorption on  $Ni^{2+}$ -NTA functionalized vesicles occurred.

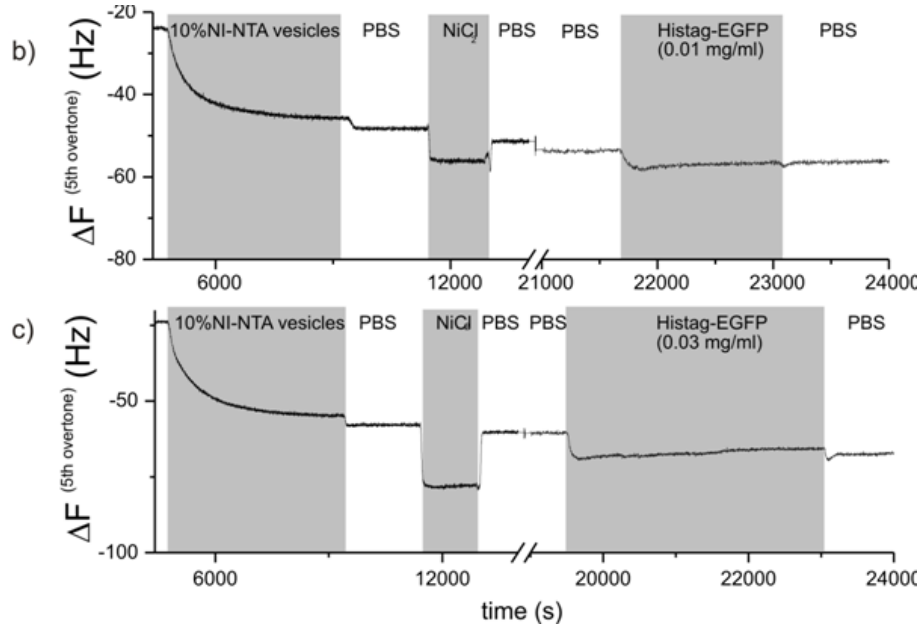


**Figure 67:** When vesicles ( $\text{PB}_{60}\text{-PEO}_{34}\text{-SA-0.1NTA.d-Ni}^{2+}$ ) with 10%  $\text{Ni}^{2+}$ -NTA groups were incubated in  $\text{His}_6\text{-EGFP}$  at 0.01 mg/mL (b) and 0.03 mg/mL (c), frequency changes were detected, indicative of protein adsorption. In all cases surfaces were treated with  $\text{NiCl}_2$  (3 mM) to ensure that all available NTA groups of the outer vesicle membrane formed nickel complexes.

The mass of adsorbed protein per unit area,  $\Delta\sigma_m$ , was estimated again from  $\Delta F$  using the Sauerbrey equation where  $a$  is the sensor area,  $C = 17.7 \text{ ng/cm}^2\text{Hz}$  for a 5 MHz resonating quartz sensor and  $n = 5$  is the overtone number. The adsorbed masses and their corresponding numbers of moles are given in Table 8.

**Table 8:** The mass of adsorbed protein per unit area and its corresponding number of moles in dependence of the protein concentration (and therefore  $\Delta F$ ). For comparison the number of moles of adsorbed vesicles with a diameter of  $d = 0.05 \mu\text{m}$  (from table 7) is shown in the last row.

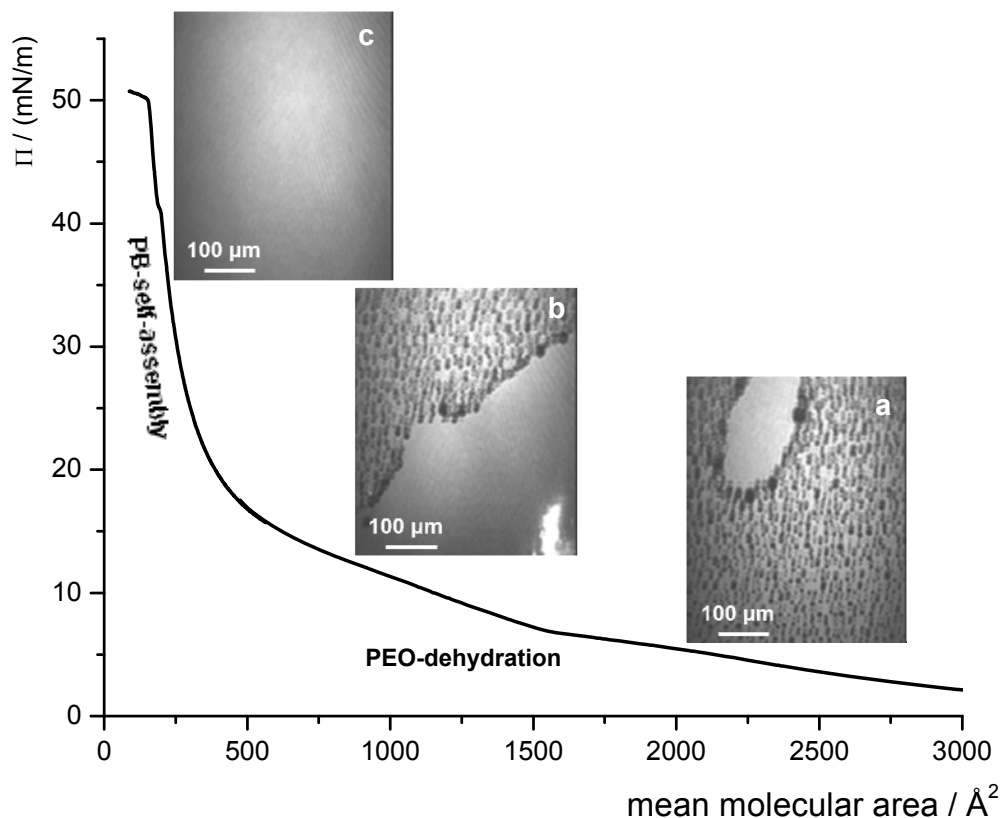
	3Hz ( $c_{\text{prot.}} = 0.01 \text{ mg/mL}$ )	7Hz ( $c_{\text{prot.}} = 0.03 \text{ mg/mL}$ )
$\Delta\sigma_m/(\mu\text{g/cm}^2)$	0.053	0.124
$\Delta n/\text{mol/cm}^2$	$1.7 \cdot 10^{-12}$	$4.1 \cdot 10^{-12}$
$n_{0.05}/\text{mol/cm}^2$	$1.7 \cdot 10^{-11}$	$1.7 \cdot 10^{-11}$

The values indicate that adsorption of the proteins occur in the same order of magnitude as the adsorption of the polymer molecules. As the vesicles are functionalized with 10%  $\text{Ni}^{2+}$ -NTA, the protein adsorption on the vesicles should be of the ratio of 1:10 (in moles), which is the case for the  $0.05 \mu\text{m}$  vesicle system. Vesicles with bigger diameters adsorb less relative to the proteins, but still in the same order of magnitude. A reason for the deviation is an incorrect assumption of a homogeneous GUV (e.g.  $5 \mu\text{m}$ ) solution.

### 3.3 Monolayers

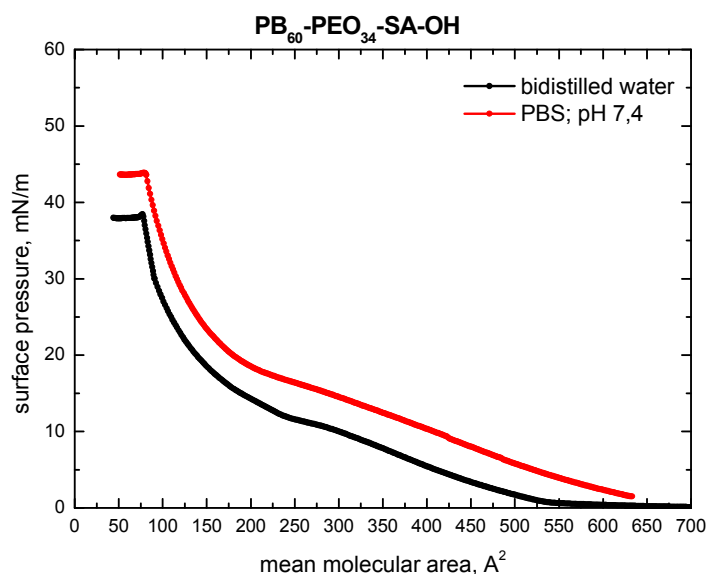
#### 3.3.1 Langmuir compression: isotherms; Brewster Angle Microscopy: images

Figure 68 shows the Langmuir compression isotherm of the PB<sub>84</sub>-PEO<sub>68</sub>-OH amphiphilic diblock copolymer. Superposed to the isotherm, the BAM images show the film forming state. In Figure 68 a and b the film size increase is visible while in Figure 68 c the homogeneous film covers the whole surface.



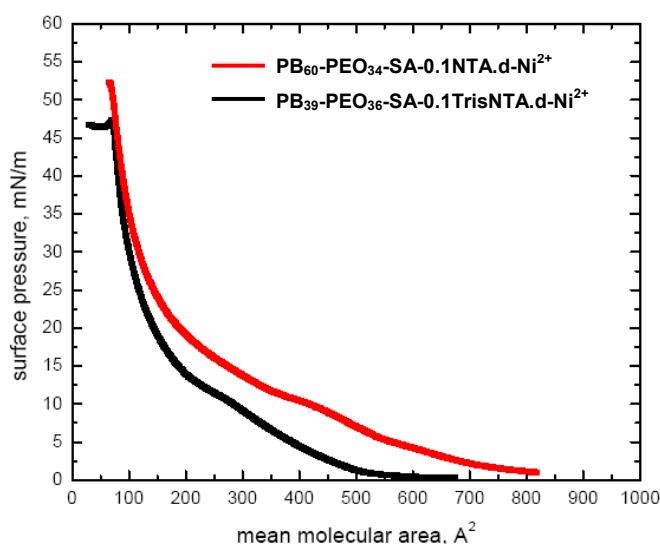
**Figure 68:** Langmuir compression: isotherm of the diblock copolymer PB<sub>84</sub>-PEO<sub>68</sub>-OH with its corresponding BAM-images. The film was made on bidistilled water.

Figure 69 shows the Langmuir compression isotherms of PB<sub>60</sub>-PEO<sub>34</sub>-SA-OH on two different media: bidistilled water and PBS buffer pH 7.4. The curves evolutions are nearly identical. The polymer film is more stable on PBS buffer (red isotherm) as the ions of the buffer stabilize the hydrophilic part (PEO) of the amphiphilic diblock copolymer. Salt ions as tiny charged molecules most likely penetrate the PEO-strand layers, break their individual hydrate shells and enable the whole system to stabilize via hydrogen bonds.



**Figure 69:** Langmuir compression: isotherm of the diblock copolymer PB<sub>60</sub>-PEO<sub>34</sub>-SA-OH on bidistilled water and PBS buffer, pH 7.4.

Figure 70 shows the Langmuir compression isotherms of PB<sub>60</sub>-PEO<sub>34</sub>-SA-0.1NTA.d-Ni<sup>2+</sup> and PB<sub>39</sub>-PEO<sub>36</sub>-SA-0.1TrisNTA.d-Ni<sup>2+</sup> on bidistilled water. The shapes of the curves are again nearly identical. The more hydrophobic amphiphilic diblock copolymer PB<sub>60</sub>-PEO<sub>34</sub>-SA-0.1NTA.d-Ni<sup>2+</sup> forms a more stable film due to the higher ratio of hydrophobicity which allows the polymer to create a more stable layer on the water.



**Figure 70:** Langmuir compression: isotherm of the diblock copolymers PB<sub>60</sub>-PEO<sub>34</sub>-SA-NTA.d-Ni<sup>2+</sup> and PB<sub>39</sub>-PEO<sub>36</sub>-SA-TrisNTA.d-Ni<sup>2+</sup> on bidistilled water.

### 3.3.2 AFM of monolayer on highly oriented pyrolytic graphite (HOPG)

Atomic force microscopy (AFM) of the transferred film of the polymer PB<sub>60</sub>-PEO<sub>34</sub>-SA-0.1NTA.d-Ni<sup>2+</sup> showed homogeneous coating in an area of few micrometers with a typical root mean square roughness ( $R_{rms}$ ) of 0.6 nm, see Figure 71. The polymer film was transferred onto the HOPG surface via Langmuir-Schaeffer.

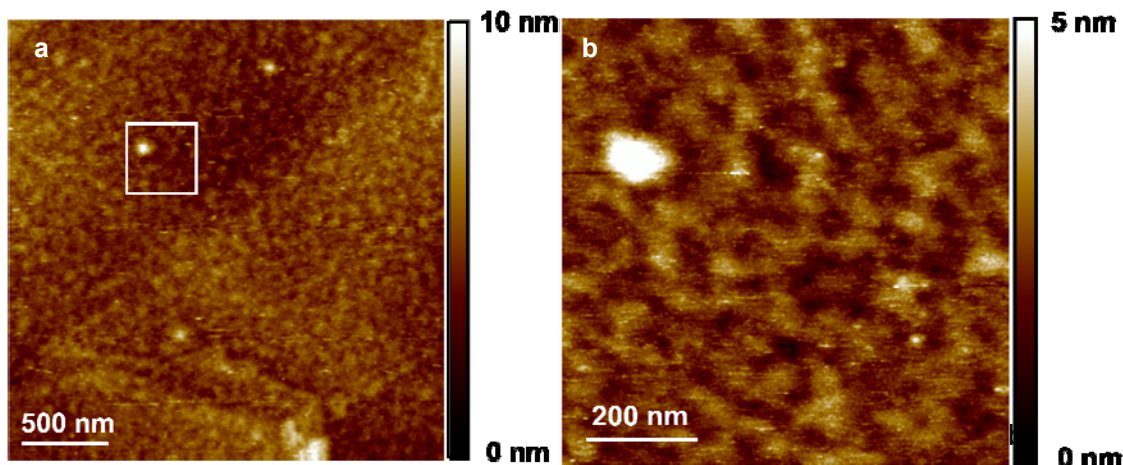


**Figure 71:** Film transfer: **a)** from bidistilled water onto HOPG via Langmuir Schaeffer film method PB<sub>60</sub>-PEO<sub>34</sub>-SA-0.1NTA.d-Ni<sup>2+</sup> on HOPG. **b)** is a Zoom in of a).

Polymer deposition was checked by scratching the sample surface with the AFM tip and subsequent material depletion in the scratched area, see Figure 72.

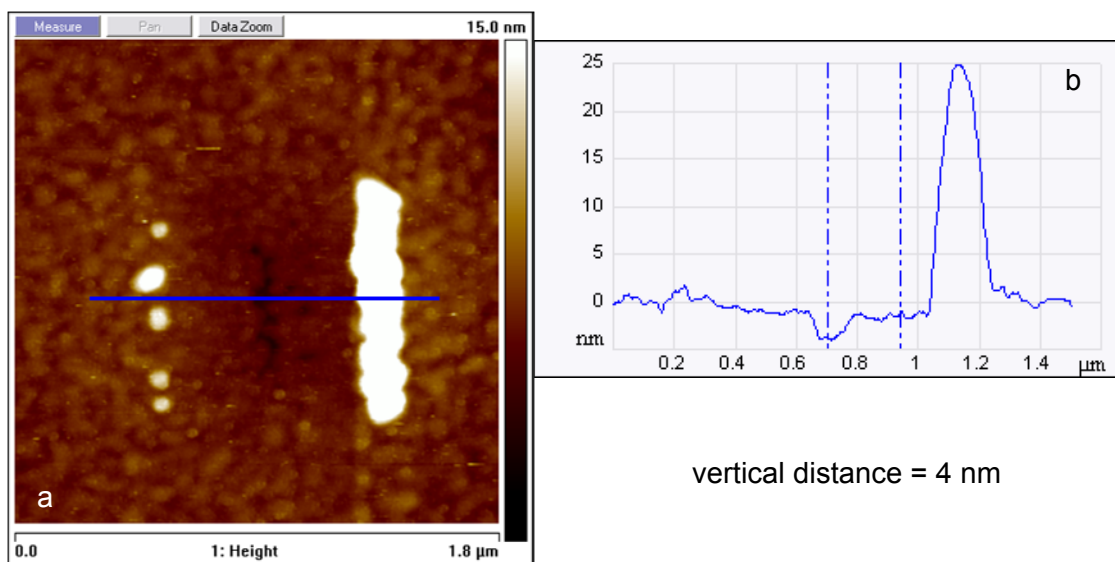


**Figure 72:** **a)** Film of PB<sub>60</sub>-PEO<sub>34</sub>-SA-NTA.d-Ni<sup>2+</sup> on HOPG (a drop of PBS pH 7.4 was spread on the polymer film), scratching at 2 V. **b)** depth histogram

The vertical distance of 4 nm in Figure 72 b determines the average thickness of the polymer film on the HOPG substrate. As the maximum chain length of the polymer PB<sub>60</sub>-

---

PEO<sub>34</sub>-0.1NTA.d-Ni<sup>2+</sup> was calculated to be 29 nm, the vertical distance of 4 nm indicates that the hydrophobic block was completely, and directly adsorbed on the surface. A part of the hydrophilic block (PEO with a maximum chain length of 12 nm) was also located on the surface, but ¼ of the chain showed towards the buffer and the proteins.

Figure 73 shows two randomly selected positions of the HOPG covered with amphiphilic diblock copolymer in PBS pH 7.4 before incubation with a protein solution. In the images a homogeneous polymer film with slight irregularities in thickness of ± 0.6 nm is presented.

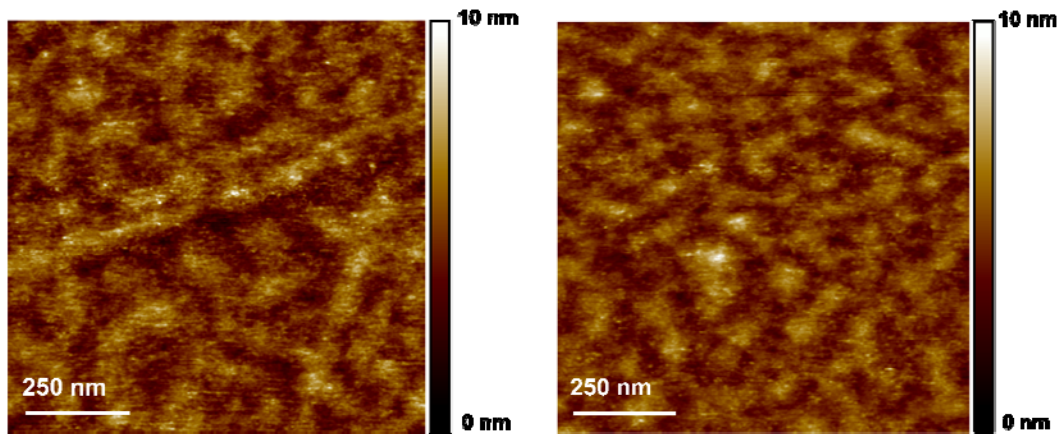


**Figure 73:** Langmuir Schaeffer film of PB<sub>60</sub>-PEO<sub>34</sub>-SA-NTA.d-Ni on HOPG (PBS pH 7.4 was spread on the polymer film) before protein incubation (**two positions**).

---

### 3.3.3 AFM: proof of the functionality of the monolayer by protein binding

We used a histidine 6 times tagged-enhanced green fluorescent protein (His<sub>6</sub>-EGFP) to test its binding activity. The EGFP is a 4 nm height and 2 nm wide cylindrically shaped, low-molecular weight protein (29 kDa), with a well-known cylindrical structure made of  $\beta$ -sheets<sup>141</sup>. The fluorophore is located in the  $\beta$ -sheet barrel. After protein incubation high resolution atomic force microscopy of the copolymer film showed, that the surface was completely covered with cylindrical structures with a size in the range of the protein, see Figure 74.

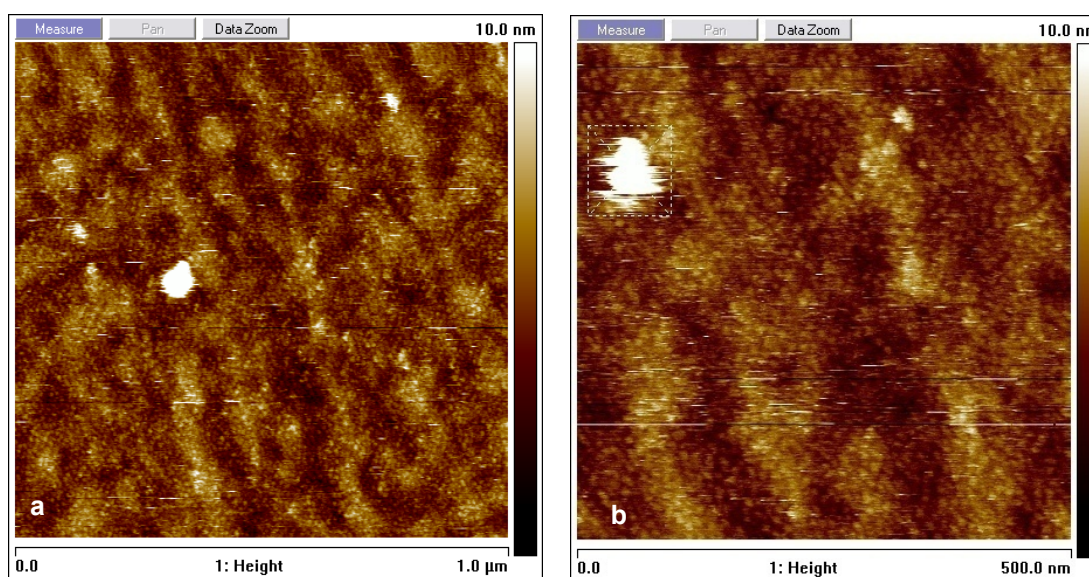


**Figure 74:** **a)** LS film of PB<sub>60</sub>-PEO<sub>34</sub>-SA-NTA.d-Ni on HOPG + His<sub>6</sub>-EGFP (with PBS pH7.4). Images were taken after protein incubation for 1.5 h (10  $\mu$ l in 100  $\mu$ l PBS buffer), **b)** Zoom in

Figure 75 shows an image of the PB<sub>60</sub>-PEO<sub>34</sub>-SA-NTA.d-Ni film on HOPG + His<sub>6</sub>-EGFP. The red bars (in the red circle) indicate the dimensions of the single proteins (His<sub>6</sub>-EGFP). The dimensions of the protein are 4 nm in length and 2 nm in diameter (cylindrical structure). The lengths of the red bars in Figure 75 are in the range of 4.5 nm to 8 nm which indicate bigger proteins as expected (2 – 4 nm). However, the AFM images of the proteins are in the same size of magnitude as the real size of the proteins. Most likely, the increase in size in the AFM images is due to the “low” resolution of the AFM tip. As the AFM tip consists of an area of square nanometers (and not square Ångstroms) it cannot resolve precisely the size of a few nanometer long protein. However, in spite of the the small size of the protein, the AFM images indicate very clearly the positions of the single proteins on the polymer layer.

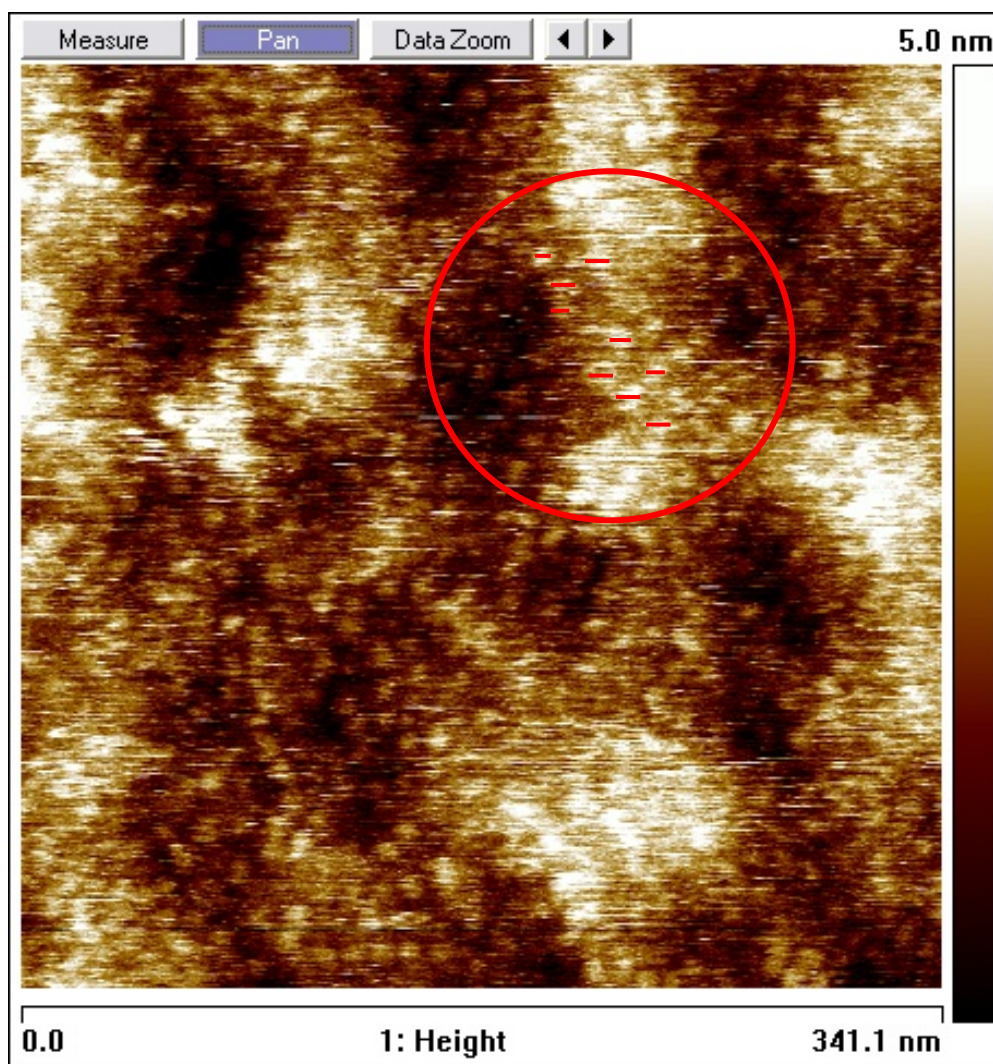


**Figure 75:** Zoom in: LS film of PB<sub>60</sub>-PEO<sub>34</sub>-SA-NTA.d-Ni on HOPG + His<sub>6</sub>-EGFP (with PBS pH7.4). Images were taken after protein incubation for 1.5 h (10  $\mu$ l in 100  $\mu$ l PBS buffer). The length of a red bar is in average 6 nm.

A quantitatively Ni<sup>2+</sup>-NTA functionalized diblock copolymer (100% Ni-NTA) was used to build the polymer film. As shown in Figure 76 the surface of the polymer film is completely covered with cylindrical objects with a size in the range of the proteins. In fact the AFM images show structures which differ in length and width, as the EGFP is 4 nm in length and 2 nm in width.

Furthermore the surface shows a regularly dense structure in which highly ordered areas (red lines in Figure 76) occur. Green fluorescent protein crystallizes in hexagonal and monoclinic structures and diffraction patterns were reported 1988.<sup>142</sup> The structure of GFP was solved in 1996 by Ormö et al.<sup>143</sup>

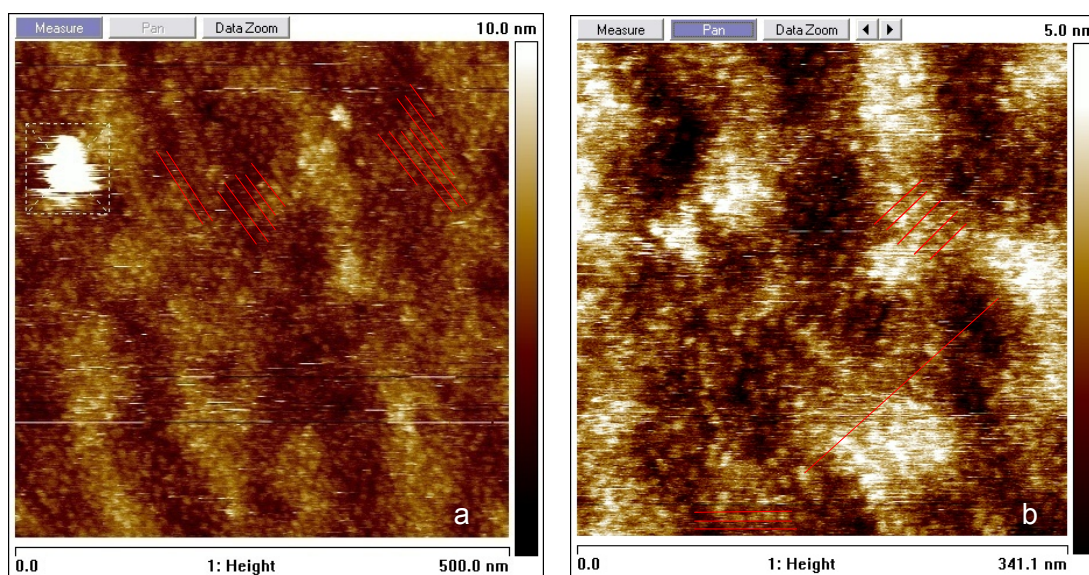


**Figure 76:** Zoom in images. The red lines show areas of highly ordered proteins.

As mentioned above GFP is an 11 stranded  $\beta$ -barrel threaded by  $\alpha$ -helix which follows the axis of a cylinder. The chromophore of the protein is attached to the  $\alpha$ -helix and is buried inside the cylinder.<sup>141</sup> Altogether, GFP is a protein with a dense structure and crystallizes three dimensional.<sup>141</sup>

The above mentioned facts and the highly ordered areas, marked by the red lines in Figure 76, let us assume that a 2D-crystallization proceeded partially.

---

## 4. Conclusions and Outlook

In this thesis, the synthesis and the characterization of poly(butadiene)-*block*-poly(ethylene oxide) copolymers with terminal Me<sup>2+</sup>-NTA groups (copper or nickel) is described for the first time. A convenient “one-pot” procedure that allows control over the individual block lengths of the copolymer and the end-group functionalization was successfully established.

The formation of the metal-polymer complex has been confirmed by EPR and UV/VIS spectroscopy. Mixing of the Ni<sup>2+</sup>-NTA polymers with the corresponding non functionalized block copolymers at a concentration of 10 mol% does not affect the self-assembly behavior of the mixtures, i.e., in dilute aqueous solutions the polymer mixtures aggregate to vesicular structures (metal-doped vesicles) with identical size distribution as the non functionalized block copolymer vesicles. Vesicles were characterized by dynamic light scattering, static light scattering, small angle X-ray scattering and zeta potential. All measurements led to the conclusion that hollow spheres, i.e. vesicles, with a narrow size distribution and a negative surface potential were generated. Moreover different vesicle shapes as “necklace pearls”, “wormlike micelles” and “spermasomes” can be attributed to different salt solutions or buffers of defined concentrations which suggests a control of morphology.

The accessibility of the metal sites at the surface of such vesicles has been tested using fluorescence correlation spectroscopy. The model proteins His<sub>10</sub>-MBP-FITC and His<sub>6</sub>-EGFP bind selectively to the Me<sup>2+</sup>-NTA groups exposed at the surface of the vesicles. While the choice of the buffer significantly influenced the fractions of protein-vesicle conjugates, the interactions of Cu<sup>2+</sup>- and Ni<sup>2+</sup>-NTA groups with both His-tagged proteins showed similar values. It should be noted that the experimentally determined dissociation constants of the Me<sup>2+</sup>-His-Tag complexes were found to be in good agreement with literature data on Ni-NTA functionalized liposomes<sup>14</sup>, indicating that the polymer brushes at the polymer vesicle surface only slightly interfere with the binding of the proteins.

Fluorescence Microscopy was used to visualize the binding of the fluorescent proteins to the functionalized vesicles and images of vesicles with a fluorescent corona were taken.

Additionally, atomic force microscopy clearly demonstrated that the polymer adsorbs in an oriented manner on highly oriented pyrolytic graphite surfaces and is able to induce a 2D protein crystallization when Ni-NTA functionalized polymer was used.

We believe that these metal-functionalized polymeric membranes have a large potential for the selective immobilization and alignment of proteins at vesicle/planar membrane surfaces. In particular, the high flexibility and compressibility of block copolymer membranes

---

and monolayers could open new possibilities for inducing a 2D protein crystallization. The high cohesion and robustness of block copolymer membranes make them rather insensitive toward mechanical shear or the presence of detergents, increasing their potential utility. In this context, it should also be noted that the pendant double bonds of the poly(butadiene) blocks can be covalently cross-linked, thus freezing the self-assembled structures and providing additional stabilization.

---

## 5. References

1. Maton, A.; Hopkins, J.; McLaughlin, W.; Johnson, S.; Warner, M. Q.; LaHart, D.; Wright, J. D., *Biology and Health. Englewood Cliffs, New Jersey, USA: Prentice Hall* **1993**.
2. von Laue, M.; von Mises, R.; Editors, *Stereoskopbilder von Kristallgittern*. 1912.
3. Seaton, B. A.; Roberts, M. F., Peripheral membrane proteins. In *Biological Membranes (Eds. K. Mertz and B. Roux)*, Birkhauser Boston **1996**, pp. 355-403.
4. Sumner, J. B., The isolation and crystallization of the enzyme urease. Preliminary paper. *Journal of Biological Chemistry* **2002**, *277*, (35), e1-e2.
5. Jones, D. T., Do transmembrane protein superfolds exist? *FEBS letters* **1998**, *423*, (3), 281-5.
6. Verkman, A. S., Aquaporin water channels and endothelial cell function. *Journal of Anatomy* **2002**, *200*, (6), 617-627.
7. Borgnia, M. J.; Agre, P., Reconstitution and functional comparison of purified GlpF and AqpZ, the glycerol and water channels from Escherichia coli. *Proceedings of the National Academy of Sciences of the United States of America* **2001**, *98*, (5), 2888-2893.
8. Levy, D.; Chami, M.; Rigaud, J. L., Two-dimensional crystallization of membrane proteins: the lipid layer strategy. *FEBS Letters* **2001**, *504*, (3), 187-193.
9. Gershon, P. D.; Khilko, S., Stable chelating linkage for reversible immobilization of oligohistidine tagged proteins in the BIAcore surface plasmon resonance detector. *Journal of Immunological Methods* **1995**, *183*, (1), 65-76.
10. Ahlers, M.; Mueller, W.; Reichert, A.; Ringsdorf, H.; Venzmer, J., Specific interactions of proteins with functional lipid monolayers. Ways of stimulating biomembrane processes. *Angewandte Chemie* **1990**, *102*, (11), 1310-27 (See also *Angew Chem , Int Ed Engl* , 1990, 29(11), 1269-85).
11. Madoz, J.; Kuznetzov, B. A.; Medrano, F. J.; Garcia, J. L.; Fernandez, V. M., Functionalization of Gold Surfaces for Specific and Reversible Attachment of a Fused b-Galactosidase and Choline-Receptor Protein. *Journal of the American Chemical Society* **1997**, *119*, (5), 1043-1051.
12. Hochuli, E.; Bannwarth, W.; Doebeli, H.; Gentz, R.; Stueber, D., Genetic approach to facilitate purification of recombinant proteins with a novel metal chelate adsorbent. *Bio/Technology* **1988**, *6*, (11), 1321-5.
13. Porath, J.; Carlsson, J.; Olsson, I.; Belfrage, G., Metal chelate affinity chromatography, a new approach to protein fractionation. *Nature (London, United Kingdom)* **1975**, *258*, (5536), 598-9.
14. Dorn, I. T.; Neumaier, K. R.; Tampe, R., Molecular Recognition of Histidine-Tagged Molecules by Metal-Chelating Lipids Monitored by Fluorescence Energy Transfer and Correlation Spectroscopy. *Journal of the American Chemical Society* **1998**, *120*, (12), 2753-2763.
15. Tanford, C., The hydrophobic effect and the organization of living matter. *Science (Washington, DC, United States)* **1978**, *200*, (4345), 1012-18.
16. Sackmann, E., Supported membranes: scientific and practical applications. *Science FIELD Full Journal Title: Science (New York, N.Y.)* **1996**, *271*, (5245), 43-8.
17. Tampe, R.; Dietrich, C.; Gritsch, S.; Elender, G.; Schmitt, L., Biofunctionalized membranes on solid surfaces. *Nanofabrication and Biosystems* **1996**, 201-221.
18. Brian, A. A.; McConnell, H. M., Allogeneic stimulation of cytotoxic T cells by supported planar membranes. *Proceedings of the National Academy of Sciences of the United States of America* **1984**, *81*, (19), 6159-63.
19. Chan, P. Y.; Lawrence, M. B.; Dustin, M. L.; Ferguson, L. M.; Golan, D. E.; Springer, T. A., Influence of receptor lateral mobility on adhesion strengthening between membranes containing LFA-3 and CD2. *J Cell Biol FIELD Full Journal Title: The Journal of cell biology* **1991**, *115*, (1), 245-55.

- 
20. Salafsky, J.; Groves, J. T.; Boxer, S. G., Architecture and Function of Membrane Proteins in Planar-Supported Bilayers: A Study with Photosynthetic Reaction Centers. *Biochemistry* **1996**, 35, (47), 14773-14781.
  21. McConnell, H. M., Structures and transitions in lipid monolayers at the air-water interface. *Annual Review of Physical Chemistry* **1991**, 42, 171-95.
  22. Dietrich, C.; Tampe, R., Charge determination of membrane molecules in polymer-supported lipid layers. *Biochim Biophys Acta FIELD Full Journal Title:Biochimica et biophysica acta* **1995**, 1238, (2), 183-91.
  23. Groves, J. T.; Ulman, N.; Boxer, S. G., Micropatterning fluid lipid bilayers on solid supports. *Science (Washington, D. C.)* **1997**, 275, (5300), 651-653.
  24. Sampson, N. S.; Mrksich, M.; Bertozzi, C. R., Surface molecular recognition. *Proc Natl Acad Sci U S A FIELD Full Journal Title:Proceedings of the National Academy of Sciences of the United States of America* **2001**, 98, (23), 12870-1.
  25. Goddard, J. M.; Hotchkiss, J. H., Polymer surface modification for the attachment of bioactive compounds. *Progress in Polymer Science* **2007**, 32, (7), 698-725.
  26. Hatakeyama, H.; Kikuchi, A.; Yamato, M.; Okano, T., Patterned biofunctional designs of thermoresponsive surfaces for spatiotemporally controlled cell adhesion, growth, and thermally induced detachment. *Biomaterials* **2007**, 28, (25), 3632-3643.
  27. Kruppa, M.; Mandl, C.; Miltschitzky, S.; Konig, B., A luminescent receptor with affinity for N-terminal histidine in peptides in aqueous solution. *Journal of the American Chemical Society* **2005**, 127, (10), 3362-5.
  28. Thompson, D. H.; Zhou, M.; Grey, J.; Kim, H.-k., Design, synthesis, and performance of NTA-modified lipids as templates for histidine-tagged protein crystallization. *Chemistry Letters* **2007**, 36, (8), 956.
  29. Valiokas, R.; Klenkar, G.; Tinazli, A.; Reichel, A.; Tampe, R.; Piehler, J.; Liedberg, B., Self-assembled monolayers containing terminal mono-, bis-, and tris-nitrilotriacetic acid groups: characterization and application. *Langmuir FIELD Full Journal Title:Langmuir : the ACS journal of surfaces and colloids* **2008**, 24, (9), 4959-67.
  30. Barklis, E.; McDermott, J.; Wilkens, S.; Schabtach, E.; Schmid, M. F.; Fuller, S.; Karanjia, S.; Love, Z.; Jones, R.; Rui, Y.; Zhao, X.; Thompson, D., Structural analysis of membrane-bound retrovirus capsid proteins. *The EMBO journal* **1997**, 16, (6), 1199-213.
  31. Bischler, N.; Balavoine, F.; Milkereit, P.; Tschochner, H.; Mioskowski, C.; Schultz, P., Specific interaction and two-dimensional crystallization of histidine tagged yeast RNA polymerase I on nickel-chelating lipids. *Biophysical Journal* **1998**, 74, (3), 1522-1532.
  32. Courty, S.; Lebeau, L.; Martel, L.; Lenne, P.-F.; Balavoine, F.; Dischert, W.; Konovalov, O.; Mioskowski, C.; Legrand, J.-F.; Vénien-Bryan, C., Two-Dimensional Crystallization of a Histidine-Tagged Protein on Monolayers of Fluidity-Enhanced Ni<sup>2+</sup>-Chelating Lipids. *Langmuir* **2002**, 18, (24), 9502-9512.
  33. Kubalek, E. W.; Le Grice, S. F. J.; Brown, P. O., Two-dimensional crystallization of histidine-tagged, HIV-1 reverse transcriptase promoted by a novel nickel-chelating lipid. *Journal of Structural Biology* **1994**, 113, (2), 117-23.
  34. Lebeau, L.; Lach, F.; Venien-Bryan, C.; Renault, A.; Dietrich, J.; Jahn, T.; Palmgren, M. G.; Kuhlbrandt, W.; Mioskowski, C., Two-dimensional crystallization of a membrane protein on a detergent-resistant lipid monolayer. *Journal of molecular biology* **2001**, 308, (4), 639-47.
  35. Levy, D.; Mosser, G.; Lambert, O.; Moeck, G. S.; Bald, D.; Rigaud, J.-L., Two-Dimensional Crystallization on Lipid Layer: A Successful Approach for Membrane Proteins. *Journal of Structural Biology* **1999**, 127, (1), 44-52.
  36. Thess, A.; Hutschenreiter, S.; Hofmann, M.; Tampe, R.; Baumeister, W.; Guckenberger, R., Specific orientation and two-dimensional crystallization of the proteasome at metal-chelating lipid interfaces. *Journal of Biological Chemistry* **2002**, 277, (39), 36321-36328.
-

- 
37. Vénien-Bryan, C.; Schertler, G. F.; Thouvenin, E.; Courty, S., Projection structure of a transcriptional regulator, HupR, determined by electron cryo-microscopy. *Journal of molecular biology* **2000**, 296, (3), 863-71.
38. Vénien-Bryan, C.; Balavoine, F.; Toussaint, B.; Mioskowski, C.; Hewat, E. A.; Helme, B.; Vignais, P. M., Structural study of the response regulator HupR from *Rhodobacter capsulatus*. Electron microscopy of two-dimensional crystals on a nickel-chelating lipid. *Journal of molecular biology* **1997**, 274, (5), 687-92.
39. Radler, U.; Mack, J.; Persike, N.; Jung, G.; Tampé, R., Design of supported membranes tethered via metal-affinity ligand-receptor pairs. *Biophysical journal* **2000**, 79, (6), 3144-52.
40. Nielsen Ulrik, B.; Kirpotin Dmitri, B.; Pickering Edward, M.; Drummond Daryl, C.; Marks James, D., A novel assay for monitoring internalization of nanocarrier coupled antibodies. *BMC immunology* **2006**, 7, 24.
41. Waters, E. K.; Morrissey, J. H., Restoring Full Biological Activity to the Isolated Ectodomain of an Integral Membrane Protein. *Biochemistry* **2006**, 45, (11), 3769-3774.
42. Chikh, G. G.; Li, W. M.; Schutze-Redelmeier, M.-P.; Meunier, J.-C.; Bally, M. B., Attaching histidine-tagged peptides and proteins to lipid-based carriers through use of metal-ion-chelating lipids. *Biochimica et Biophysica Acta, Biomembranes* **2002**, 1567, (1-2), 204-212.
43. Schmitt, L.; Dietrich, C.; Tampé, R., Synthesis and Characterization of Chelator-Lipids for Reversible Immobilization of Engineered Proteins at Self-Assembled Lipid Interfaces. *Journal of the American Chemical Society* **1994**, 116, (19), 8485-91.
44. Jap, B. K.; Zulauf, M.; Scheybani, T.; Hefti, A.; Baumeister, W.; Aebi, U.; Engel, A., 2D crystallization: from art to science. *Ultramicroscopy* **1992**, 46, (1-4), 45-84.
45. Rigaud, J.; Chami, M.; Lambert, O.; Levy, D.; Ranck, J., Use of detergents in two-dimensional crystallization of membrane proteins. *Biochim Biophys Acta FIELD Full Journal Title:Biochimica et biophysica acta* **2000**, 1508, (1-2), 112-28.
46. Stahlberg, H.; Fotiadis, D.; Scheuring, S.; Remigy, H.; Braun, T.; Mitsuoka, K.; Fujiyoshi, Y.; Engel, A., Two-dimensional crystals: a powerful approach to assess structure, function and dynamics of membrane proteins. *FEBS Letters* **2001**, 504, (3), 166-172.
47. Walz, T.; Grigorieff, N., Electron crystallography of two-dimensional crystals of membrane proteins. *Journal of Structural Biology* **1998**, 121, (2), 142-161.
48. Werten, P. J. L.; Remigy, H. W.; de Groot, B. L.; Fotiadis, D.; Philippsen, A.; Stahlberg, H.; Grubmuller, H.; Engel, A., Progress in the analysis of membrane protein structure and function. *FEBS Letters* **2002**, 529, (1), 65-72.
49. Shnek, D. R.; Pack, D. W.; Sasaki, D. Y.; Arnold, F. H., Specific Protein Attachment to Artificial Membranes via Coordination to Lipid-Bound Copper(II). *Langmuir* **1994**, 10, (7), 2382-8.
50. Heath, T. D., Covalent attachment of proteins to liposomes. *Methods Enzymol FIELD Full Journal Title:Methods in enzymology* **1987**, 149, 111-9.
51. Lebeau, L.; Nuss, S.; Schultz, P.; Oudet, P.; Mioskowski, C., Self-assembly of soluble proteins on functionalized lipid layers: a tentative correlation between the fluidity properties of the lipid film and protein ordering. *Chemistry and Physics of Lipids* **1999**, 103, (1-2), 37-46.
52. Nardin, C.; Winterhalter, M.; Meier, W., Giant Free-Standing ABA Triblock Copolymer Membranes. *Langmuir* **2000**, 16, (20), 7708-7712.
53. Harris, J. M.; Chess, R. B., Effect of PEGylation on pharmaceuticals. *Nature Reviews Drug Discovery* **2003**, 2, (3), 214-221.
54. Veronese, F. M.; Harris, J. M., Introduction and overview of peptide and protein pegylation. *Advanced Drug Delivery Reviews* **2002**, 54, (4), 453-456.
55. Foerster, S.; Kraemer, E., Synthesis of PB-PEO and PI-PEO Block Copolymers with Alkylolithium Initiators and the Phosphazene Base t-BuP4. *Macromolecules* **1999**, 32, (8), 2783-2785.
-

- 
56. Zalipsky, S., Functionalized Poly(ethylene glycols) for Preparation of Biologically Relevant Conjugates. *Bioconjugate Chemistry* **1995**, 6, (2), 150-65.
57. Meier, W., Polymer nanocapsules. *Chemical Society Reviews* **2000**, 29, (5), 295-303.
58. Antonietti, M.; Foerster, S., Vesicles and liposomes: A self-assembly principle beyond lipids. *Advanced Materials (Weinheim, Germany)* **2003**, 15, (16), 1323-1333.
59. Israelachvili, J. N., *Intermolecular and Surface Forces*. 1991; p 291 pp.
60. Janiak, M. J.; Small, D. M.; Shipley, G. G., Temperature and compositional dependence of the structure of hydrated dimyristoyl lecithin. *Journal of Biological Chemistry* **1979**, 254, (13), 6068-78.
61. Huang, L.; Yuan, H.; Zhang, D.; Zhang, Z.; Guo, J.; Ma, J., Controlled microphase separated morphology of block polymer thin film and an approach to prepare inorganic nanoparticles. *Applied Surface Science* **2004**, 225, (1-4), 39-46.
62. Jenekhe, S. A.; Chen, X. L., Self-assembled organic semiconductor quantum boxes and wires from block copolymers. *Book of Abstracts, 213th ACS National Meeting, San Francisco, April 13-17 1997*, POLY-556.
63. Kawakatsu, T.; Kawasaki, K.; Andelman, D., Two topics on phase separation phenomena of amphiphilic systems. *KEK Proceedings 1993*, 93-3, (Proceedings of the Workshop on Polymer Science Studied By Neutron Scattering, 1991), 3-5.
64. Di Marzio, E. A., The ten classes of polymeric phase transitions: their use as models for self-assembly. *Progress in Polymer Science* **1999**, 24, (3), 329-377.
65. Kita-Tokarczyk, K.; Grumelard, J.; Haefele, T.; Meier, W., Block copolymer vesicles—using concepts from polymer chemistry to mimic biomembranes. *Polymer* **2005**, 46, (11), 3540-3563.
66. Klok, H.-A.; Lecommandoux, S., Supramolecular materials via block copolymer self-assembly. *Advanced Materials (Weinheim, Germany)* **2001**, 13, (16), 1217-1229.
67. Wang, Z. G., *Macromolecules* **1992**, 25, 3702-5.
68. Luo, L.; Eisenberg, A., Thermodynamic Size Control of Block Copolymer Vesicles in Solution. *Langmuir* **2001**, 17, (22), 6804-6811.
69. Lasic, D. D.; Joannic, R.; Keller, B. C.; Frederik, P. M.; Auvray, L., Spontaneous vesiculation. *Adv Colloid Interface Sci FIELD Full Journal Title:Advances in colloid and interface science* **2001**, 89-90, 337-49.
70. Hyde, S. T., Curvature and the global structure of interfaces in surfactant-water systems. *Colloque de Physique 1990*, (C7, Int. Workshop Geom. Interfaces, 1990), C7-209-C7-228.
71. Israelachvili, J. N.; Mitchell, D. J.; Ninham, B. W., Theory of self-assembly of hydrocarbon amphiphiles into micelles and bilayers. *Journal of the Chemical Society, Faraday Transactions 2: Molecular and Chemical Physics* **1976**, 72, (9), 1525-68.
72. Zhang, L.; Eisenberg, A., Multiple Morphologies and Characteristics of "Crew-Cut" Micelle-like Aggregates of Polystyrene-b-poly(acrylic acid) Diblock Copolymers in Aqueous Solutions. *Journal of the American Chemical Society* **1996**, 118, (13), 3168-81.
73. Discher, B. M.; Won, Y.-Y.; Ege, D. S.; Lee, J. C. M.; Bates, F. S.; Discher, D. E.; Hammer, D. A., Polymersomes: Tough vesicles made from diblock copolymers. *Science (Washington, D. C.)* **1999**, 284, (5417), 1143-1146.
74. Hajduk, D. A.; Kossuth, M. B.; Hillmyer, M. A.; Bates, F. S., Complex Phase Behavior in Aqueous Solutions of Poly(ethylene oxide)-Poly(ethylene) Block Copolymers. *Journal of Physical Chemistry B* **1998**, 102, (22), 4269-4276.
75. Discher, D. E.; Ahmed, F., Polymersomes. *Annual Review of Biomedical Engineering* **2006**, 8, 323-341.
76. Shen, H.; Eisenberg, A., Morphological Phase Diagram for a Ternary System of Block Copolymer PS310-b-PAA52/Dioxane/H<sub>2</sub>O. *Journal of Physical Chemistry B* **1999**, 103, (44), 9473-9487.
77. Foerster, S.; Antonietti, M., Amphiphilic block copolymers in structure-controlled nanomaterial hybrids. *Advanced Materials (Weinheim, Germany)* **1998**, 10, (3), 195-217.
-

- 
78. Thordarson, P.; Droumaguet, B.; Velonia, K., Well-defined protein-polymer conjugates-synthesis and potential applications. *Applied Microbiology and Biotechnology* **2006**, 73, (2), 243-254.
79. Maeda, H., SMANCS and polymer-conjugated macromolecular drugs: advantages in cancer chemotherapy. *Advanced Drug Delivery Reviews* **2001**, 46, (1-3), 169-185.
80. Maeda, H., The enhanced permeability and retention (EPR) effect in tumor vasculature: the key role of tumor-selective macromolecular drug targeting. *Adv Enzyme Regul FIELD Full Journal Title:Advances in enzyme regulation* **2001**, 41, 189-207.
81. Ulbrich, K.; Strohalm, J.; Subr, V.; Plocova, D.; Duncan, R.; Rihova, B., Polymeric conjugates of drugs and antibodies for site-specific drug delivery. *Macromolecular Symposia* **1996**, 103, (Polymers and Medicine), 177-92.
82. Caliceti, P.; Veronese, F. M., Pharmacokinetic and biodistribution properties of poly(ethylene glycol)-protein conjugates. *Advanced Drug Delivery Reviews* **2003**, 55, (10), 1261-1277.
83. Niemeyer, C. M., Nanoparticles, proteins, and nucleic acids: biotechnology meets materials science. *Angewandte Chemie, International Edition* **2001**, 40, (22), 4128-4158.
84. Pennadam, S. S.; Firman, K.; Alexander, C.; Gorecki, D. C., Protein-polymer nanomachines. Towards synthetic control of biological processes. *Journal of Nanobiotechnology* **2004**, 2, No pp given.
85. Shimoboji, T.; Ding, Z.; Stayton, P. S.; Hoffman, A. S., Mechanistic Investigation of Smart Polymer-Protein Conjugates. *Bioconjugate Chemistry* **2001**, 12, (2), 314-319.
86. van Hest, J. C. M.; Tirrell, D. A., Protein-based materials, toward a new level of structural control. *Chemical Communications (Cambridge, United Kingdom)* **2001**, (19), 1897-1904.
87. Broz, P.; Benito, S. M.; Saw, C.; Burger, P.; Heider, H.; Pfisterer, M.; Marsch, S.; Meier, W.; Hunziker, P., Cell targeting by a generic receptor-targeted polymer nanocontainer platform. *Journal of Controlled Release* **2005**, 102, (2), 475-488.
88. Klok, H.-A., Biological-synthetic hybrid block copolymers: Combining the best from two worlds. *Journal of Polymer Science, Part A: Polymer Chemistry* **2005**, 43, (1), 1-17.
89. Rigler, P.; Meier, W., Encapsulation of fluorescent molecules by functionalized polymeric nanocontainers: investigation by confocal fluorescence imaging and fluorescence correlation spectroscopy. *Journal of the American Chemical Society* **2006**, 128, (1), 367-373.
90. Lin, J. J.; Silas, J. A.; Bermudez, H.; Milam, V. T.; Bates, F. S.; Hammer, D. A., The Effect of Polymer Chain Length and Surface Density on the Adhesiveness of Functionalized Polymersomes. *Langmuir* **2004**, 20, (13), 5493-5500.
91. Graff, A.; Sauer, M.; Van Gelder, P.; Meier, W., Virus-assisted loading of polymer nanocontainer. *Proceedings of the National Academy of Sciences of the United States of America* **2002**, 99, (8), 5064-5068.
92. Taubert, A.; Napoli, A.; Meier, W., Self-assembly of reactive amphiphilic block copolymers as mimetics for biological membranes. *Current Opinion in Chemical Biology* **2004**, 8, (6), 598-603.
93. Nardin, C.; Meier, W., Hybrid materials from amphiphilic block copolymers and membrane proteins. *Reviews in Molecular Biotechnology* **2002**, 90, (1), 17-26.
94. Mecke, A.; Dittrich, C.; Meier, W., Biomimetic membranes designed from amphiphilic block copolymers. *Soft Matter* **2006**, 2, (9), 751-759.
95. Discher, B. M.; Bermudez, H.; Hammer, D. A.; Discher, D. E.; Won, Y.-Y.; Bates, F. S., Cross-linked Polymersome Membranes: Vesicles with Broadly Adjustable Properties. *Journal of Physical Chemistry B* **2002**, 106, (11), 2848-2854.
96. Nehring, R.; Palivan, C. G.; Casse, O.; Tanner, P.; Tuxen, J.; Meier, W., Amphiphilic Diblock Copolymers for Molecular Recognition: Metal-Nitrilotriacetic Acid Functionalized Vesicles. *Langmuir* **2008**, ACS ASAP.
97. Gao, W.-P.; Bai, Y.; Chen, E.-Q.; Li, Z.-C.; Han, B.-Y.; Yang, W.-T.; Zhou, Q.-F., Controlling Vesicle Formation via Interpolymer Hydrogen-Bonding Complexation between
-

- 
- Poly(ethylene oxide)-block-polybutadiene and Poly(acrylic acid) in Solution. *Macromolecules* **2006**, 39, (14), 4894-4898.
98. Geng, Y.; Discher, D. E.; Justynska, J.; Schlaad, H., Grafting short peptides onto polybutadiene-block-poly(ethylene oxide): a platform for self-assembling hybrid amphiphiles. *Angewandte Chemie, International Edition* **2006**, 45, (45), 7578-7581.
99. Jain, S.; Bates, F. S., On the Origins of Morphological Complexity in Block Copolymer Surfactants. *Science (Washington, DC, United States)* **2003**, 300, (5618), 460-464.
100. Schwartz, A., Glass transition temperatures of polymer materials, measured by thermomechanical analysis. Influence of rates of heating and cooling. *Journal of Thermal Analysis* **1978**, 13, (3), 489-97.
101. Elias, H. G., *Macromolecules*, 6th edition, Wiley-WCH, Weinheim, 2002.
102. Domininghaus, H., *Die Kunststoffe und ihre Eigenschaften*, 6th edition, Springer, Berlin, 2005.
103. Anon, *Indirect Food Additives and Polymers: Migration and Toxicology*. By Victor O. Sheffel (Ministry of Health, State of Israel, Jerusalem). Lewis Publishers: Boca Raton, FL. 2000. xvi + 1304 pp. \$129.95. ISBN 1-56670-499-5. 2000; Vol. 122, p 10742.
104. Esswein, B.; Moeller, M., Polymerization of ethylene oxide with alkyl lithium compounds and the phosphazene base  $\text{tBu-P4}$ . *Angewandte Chemie, International Edition in English* **1996**, 35, (6), 623-5.
105. Hadjichristidis, N.; Iatrou, H.; Pispas, S.; Pitsikalis, M., Anionic polymerization: high vacuum techniques. *Journal of Polymer Science, Part A: Polymer Chemistry* **2000**, 38, (18), 3211-3234.
106. Hathaway, B. J., *Comprehensive Coordination Chemistry*. *Comprehensive Coordination Chemistry*, G. Wilkinson (Ed.), Pergamon Press **1987**, 5, 134-145.
107. Menger, F. M.; Angelova, M. I., Giant Vesicles: Imitating the Cytological Processes of Cell Membranes. *Accounts of Chemical Research* **1998**, 31, (12), 789-797.
108. Angelova, M.; Dimitrov, D., Liposome electroformation. *Faraday Discussions of the Chemical Society* **1986**, 81, (1), 303-11.
109. Debye, P., Light scattering in solutions. *Journal of Applied Physics* **1944**, 15, 338-42.
110. Einstein, A., Opalescence theory of homogeneous liquids and liquid mixtures in the vicinity of the critical state. *Annalen der Physik (Weinheim, Germany)* **1910**, 33, 1275-1298.
111. Raman, C. V., Relation of Tyndall effect to osmotic pressure in colloidal solutions. *Indian Journal of Physics* **1927**, 2, 1-6.
112. Zimm, B. H., Molecular theory of the scattering of light in fluids. *Journal of Chemical Physics* **1945**, 13, 141-5.
113. Zimm, B. H., The scattering of light and the radial distribution function of high-polymer solutions. *Journal of Chemical Physics* **1948**, 16, 1093-9.
114. Schmitz, K. S., An Introduction to Dynamic Light Scattering by Macromolecules. *An Introduction to Dynamic Light Scattering by Macromolecules*, Academic Press Inc. **1990**.
115. Burchard, W., Static and dynamic light scattering from branched polymers and biopolymers. *Advances in Polymer Science* **1983**, 48, (Light Scattering Polym.), 1-124.
116. Glatter, O.; Kratky, O.; Editors, *Small Angle X-ray Scattering*. 1982; p 515 pp.
117. Schmuck, C.; Rehm, T.; Klein, K.; Grohn, F., Formation of vesicular structures through the self-assembly of a flexible bis-zwitterion in dimethyl sulfoxide. *Angew Chem Int Ed Engl FIELD Full Journal Title:Angewandte Chemie (International ed. in English)* **2007**, 46, (10), 1693-7.
118. Kucerka, N.; Pencser, J.; Sachs Jonathan, N.; Nagle John, F.; Katsaras, J., Curvature effect on the structure of phospholipid bilayers. *Langmuir FIELD Full Journal Title:Langmuir : the ACS journal of surfaces and colloids* **2007**, 23, (3), 1292-9.
119. Montaser, A.; Golightly, D. W., VCH Publishers, Inc., New York: 1992.
120. Sauerbrey, G., The use of quartz oscillators for weighing thin layers and for microweighing. *Zeitschrift fuer Physik* **1959**, 155, 206-22.
-

- 
121. Eigen, M.; Rigler, R., Sorting single molecules: application to diagnostics and evolutionary biotechnology. *Proceedings of the National Academy of Sciences of the United States of America* **1994**, 91, (13), 5740-7.
122. Triest, M.; Bussiere, G.; Belisle, H.; Reber, C., Why does the middle band in the absorption spectrum of Ni(H<sub>2</sub>O)<sub>6</sub><sup>2+</sup> have two maxima? *Journal of Chemical Education* **2000**, 77, (5), 670.
123. Medici, L.; Prins, R., Structure of oxidic NiMo/SiO<sub>2</sub> hydrotreating catalyst precursors. *Journal of Catalysis* **1996**, 163, (1), 28-37.
124. Dembowski, J. S.; Kurtz, D. C.; Nakon, R., Aminoacidate dechelation upon hydroxo complex formation in mixed ligand metal chelates. *Inorganica Chimica Acta* **1988**, 152, (4), 209-10.
125. Palivan, C. G.; Goodman, B. A., Determination of the copper coordination environment in superoxide dismutases (SODs) and complexes with SOD activity using molecular mechanics force field calculations and electron paramagnetic resonance spectroscopy. *Recent Research Developments in Inorganic & Organometallic Chemistry* **2001**, 1, 141-159.
126. Palivan, C. G.; Palivan, H. M. N.; Goodman, B. A.; Cristescu, C., ESR study of some asymmetric-triazine copper(II) complexes having high antiviral activity. *Applied Magnetic Resonance* **1998**, 15, (3-4), 477-488.
127. Bermudez, H.; Brannan, A. K.; Hammer, D. A.; Bates, F. S.; Discher, D. E., Molecular Weight Dependence of Polymersome Membrane Structure, Elasticity, and Stability. *Macromolecules* **2002**, 35, (21), 8203-8208.
128. Angelova, M.; Dimitrov, D., A mechanism of liposome electroformation. *Progress in Colloid & Polymer Science* **1988**, 76, (Trends Colloid Interface Sci., 2), 59-67.
129. Dimitrov, D.; Angelova, M., Lipid swelling and liposome formation on solid surfaces in external electric fields. *Progress in Colloid & Polymer Science* **1987**, 73, (New Trends Colloid Sci.), 48-56.
130. Finsy, R., Particle sizing by quasi-elastic light scattering. *Advances in Colloid and Interface Science* **1994**, 52, 79-143.
131. Lee, J. C. M.; Bermudez, H.; Discher, B. M.; Sheehan, M. A.; Won, Y.-Y.; Bates, F. S.; Discher, D. E., Preparation, stability, and in vitro performance of vesicles made with diblock copolymers. *Biotechnology and Bioengineering* **2001**, 73, (2), 135-145.
132. Kucerka, N.; Pencer, J.; Sachs, J. N.; Nagle, J. F.; Katsaras, J., Curvature effect on the structure of phospholipid bilayers. *Langmuir* **2007**, 23, (3), 1292-1299.
133. Frielinghaus, H., Small-angle scattering model for multilamellar vesicles. *Phys Rev E Stat Nonlin Soft Matter Phys FIELD Full Journal Title:Physical review. E, Statistical, nonlinear, and soft matter physics* **2007**, 76, (5 Pt 1), 051603.
134. Bartlett, P.; Ottewill, R. H., A neutron-scattering study of the structure of a bimodal colloidal crystal. *Journal of Chemical Physics* **1992**, 96, (4), 3306-18.
135. Glatter, O.; Kratky, O., *Small Angle X-ray Scattering*. Academic Press: London, 1982.
136. Van Krevlen, D. W., *Properties of Polymers, Chapter 4: Volumetric Properties*. Elsevier: Amsterdam. 1990.
137. <http://www.zirchrom.com/organic.htm>. <http://www.zirchrom.com/organic.htm>
138. Marx, K. A., Quartz crystal microbalance: a useful tool for studying thin polymer films and complex biomolecular systems at the solution-surface interface. *Biomacromolecules* **2003**, 4, (5), 1099-1120.
139. Glasmaestar, K.; Larsson, C.; Hooeok, F.; Kasemo, B., Protein Adsorption on Supported Phospholipid Bilayers. *Journal of Colloid and Interface Science* **2002**, 246, (1), 40-47.
140. Korlach, J.; Schwille, P.; Webb, W. W.; Feigenson, G. W., Characterization of lipid bilayer phases by confocal microscopy and fluorescence correlation spectroscopy. *Proceedings of the National Academy of Sciences of the United States of America* **1999**, 96, (15), 8461-8466.
-

- 
141. Tsien, R. Y., The green fluorescent protein. *Annual Review of Biochemistry* **1998**, 67, 509-544.
142. Perozzo, M. A.; Ward, K. B.; Thompson, R. B.; Ward, W. W., X-ray diffraction and time-resolved fluorescence analyses of Aequorea green fluorescent protein crystals. *Journal of Biological Chemistry* **1988**, 263, (16), 7713-16.
143. Ormo, M.; Cubitt, A. B.; Kallio, K.; Gross, L. A.; Tsien, R. Y.; Remington, S. J., Crystal structure of the Aequorea victoria green fluorescent protein. *Science FIELD Full Journal Title:Science (New York, N.Y.)* **1996**, 273, (5280), 1392-5.

---

## Curriculum Vitae

### Personal data

---

Name	Rainer Nehring
Address	Ryffstr. 42 CH - 4056 Basel, Switzerland <a href="mailto:rainer.nehring@unibas.ch">rainer.nehring@unibas.ch</a>
Phone	+41 (0)61 321 7992
Nationality	German
Place of birth	Marl, NRW, Germany
Date of birth	10.09.1967
Marital status	divorced, one child

### Education

---

Since 09/ 2005	PhD thesis with Prof. Wolfgang Meier, Department of Chemistry, University of Basel: <i>Amphiphilic diblock copolymers for molecular recognition</i>
01/2005 – 08/2005	Master with Prof. Wolfgang Meier Department of Chemistry, University of Basel: <i>Ring opening metathesis polymerization (ROMP) of functionalized amphiphilic triblock copolymers</i>
11/2003 – 06/2004	Diploma with Prof. Dr.-Ing. H.-D. Steppke, University of Applied Sciences Berlin; Dr. habil. Andreas Thünemann, Bundesanstalt für Materialforschung u. -prüfung (BAM), Berlin and Dr. Jean-Francois Lutz, Fraunhofer Institute for Applied Polymer Research, Potsdam-Golm: <i>Controlled radical polymerization of nucleic acids bearing monomers</i>
10/1999 – 10/2003	Studies in Pharmaceutical and Chemical Engineering at the University of Applied Sciences Berlin
02/1996 – 01/1999	Professional Training as Technical Assistant in Chemistry and Biology (CTA/BTA) at Lette foundation, Berlin; (diploma in 1999)
1993 – 1995	Studies in Food chemistry at Technische Universität Berlin
1988 – 1992	Studies in Chemistry at Freie Universität Berlin
1987	High school diploma (Abitur) at the Albert-Schweitzer-Gymnasium Marl

---

## Professional experience

---

- Since 09/ 2005      PhD research, group Prof. Wolfgang Meier, Institut Physikalische Chemie
- Polymer Synthesis via Anionic Polymerization and characterization;  
Preparation of vesicles via rehydration & electroformation and analysis of the polymer self-assemblies in aqueous solutions;  
Preparation of the polymer biomimetic membranes on gold and HOPG surfaces and investigation of thin polymer films and surface functionalization with the help of His tagged proteins
- 07/2004 – 12/2004      Research assistant, group Dr. Jean-Francois Lutz, Fraunhofer Institute for Applied Polymer Research, Golm-Potsdam, Germany
- Synthesis and characterization of synthetic macromolecules bearing nucleic acid bases side groups using either conventional radical polymerization or controlled radical polymerization. Study of the self-assembly of the macromolecules bearing complementary nucleic acid bases side groups.
- 06/1999 – 09/1999      Technical Assistant at BioTez Berlin-Buch GmbH, Berlin, Germany
- Development of enzyme immunoassays for cytokines, endotoxines and clenbuterol; ELISA development
- 03/1999      Academic Module in the International English Language Testing System at the British Council, Berlin, Germany
- 01/1999      Basic course radiation protection for the technical qualification grade 2.2 in Germany, Berlin, Germany
- 1989 – 1994      Work experience in the chemical industry as craftsman at Hüls AG, Marl, Germany
- 02/1988 – 03/1988      Practical training in metal processing at Hüls AG, Marl, Germany
- Basic training in metal working and machine tools; forging, gas fusion welding and arc welding

---

## Experimental skills

---

<i>Synthesis and Characterization</i>	<b>Chemistry.</b> Synthetic organic and polymer chemistry (ATRP, RAFT, ROMP, anionic polymerization, conventional radical polymerization), analytical chemistry, self-assembly techniques (GUVs, SUVs), surface functionalization  <b>Methods.</b> NMR, SEC, IR, UV-VIS, ICP, AAS, AES; <i>light scattering techniques:</i> DLS, SLS, SAXS; <i>microscopy:</i> optical microscope, TEM, Cryo-TEM, FCS, fluorescence microscopy, FCS; <i>surface techniques:</i> Langmuir, AFM, QCM
<i>Languages</i>	English (fluent) German (native)
<i>PC user</i>	MS Windows 2000XP/ Vista, MS Office, Origin, Excel, Adobe software, Chem Draw, MestRec, AFM image processing; search and world wide web.

---

## Awards

---

1985	Honorary citizen of Elkhorn, Walworth county, Wisconsin, USA
2005	Mary Curie fellowship (ESR BioPolySurf)

---

## Personal profile

---

	Motivated personality with pedagogic skills who enjoys learning new techniques abroad
<i>Languages</i>	English (fluent) German (native)
<i>Hobbies</i>	Art, Kieser training, Swimming, walking in the mountains

---

## References

---

Prof. Dr. Wolfgang P. Meier  
Department of Chemistry, University of Basel  
Klingelbergstrasse 80, CH-4056 Basel  
Tel.: +41 (0)61 267 3802  
E-mail: [wolfgang.meier@unibas.ch](mailto:wolfgang.meier@unibas.ch)

Prof. Dr. José Luis Toca-Herrera  
Group leader – biosurfaces  
CIC biomaGUNE  
Paseo de Miramon 182, E – 20009 San Sebastian  
Tel.: +34 943 00 53 00 / +34 943 00 53 01  
E-mail: [jltocaherrera@cicbiomagune.es](mailto:jltocaherrera@cicbiomagune.es)

Dr. habil. Andreas F. Thünemann  
Direktor und Professor  
Bundesanstalt für Materialforschung u. -prüfung (BAM)  
(Federal Institute for Materials Research and Testing)  
Richard-Willstaetter-Str. 11, D-12489 Berlin  
Tel.: +49 (0)30 8104 1139 (Sabine Tietz, Secretary)  
Tel.: +49 (0)30 8104 1130 (direct)  
E-Mail: [andreas.thuenemann@bam.de](mailto:andreas.thuenemann@bam.de)

Dr. Jean-Francois Lutz  
Group-leader Nanotechnology for Life science  
Fraunhofer Institute for Applied Polymer Research  
Geiselbergstrasse 69, D – 14476 Golm  
Tel.: +49 (0) 331 568 1127  
E-mail: [lutz@iap.fhg.de](mailto:lutz@iap.fhg.de)

Dr. Cornelia Palivan  
Department of Chemistry, University of Basel  
Klingelbergstrasse 80, CH-4056 Basel  
Tel.: +41 (0)61 267 3839  
E-mail: [cornelia.palivanr@unibas.ch](mailto:cornelia.palivanr@unibas.ch)

---

## Publications

---

Nehring, Rainer; Palivan, Cornelia G.; Casse, Oliver; Tanner, Pascal; Tuxen, Jens; Meier, Wolfgang. ***Amphiphilic Diblock Copolymers for Molecular Recognition: Metal-Nitrilotriacetic Acid Functionalized Vesicles.*** *Langmuir* (2009), 25(2), 1122-1130. CODEN: LANGD5 ISSN:0743-7463. AN 2008:1530841 CAPLUS

Lutz, Jean-Francois; Nehring, Rainer; Pfeifer, Sebastian. ***Novel organo-soluble or water-soluble copolymers containing DNA nucleobases.*** *ACS Symposium Series* (2006), 944(Controlled/Living Radical Polymerization), 185-197. CODEN: ACSMC8 ISSN:0097-6156. CAN 149:402705 AN 2007:1005510 CAPLUS

Lutz, Jean-Francois; Thuenemann, Andreas F.; Nehring, Rainer. ***Preparation by controlled radical polymerization and self-assembly via base-recognition of synthetic polymers bearing complementary nucleobases.*** *Journal of Polymer Science, Part A: Polymer Chemistry* (2005), 43(20), 4805-4818. CODEN: JPACEC ISSN:0887-624X. CAN 144:23180 AN 2005:1083271 CAPLUS

Lutz, Jean-Francois; Nehring, Rainer; Thuenemann, Andreas F. ***Solution self-assembly of synthetic copolymers bearing complementary nucleic acid functionalities.*** Abstracts of Papers, 230th ACS National Meeting, Washington, DC, United States, Aug. 28-Sept. 1, 2005 (2005), POLY-661. CODEN: 69HFCL AN 2005:742603 CAPLUS

Lutz, Jean-Francois; Nehring, Rainer; Thuenemann, Andreas F. ***Solution self-assembly of synthetic copolymers bearing complementary nucleic acid functionalities.*** *Polymer Preprints (American Chemical Society, Division of Polymer Chemistry)* (2005), 46(2), 397-398. CODEN: ACPPAY ISSN:0032-3934. CAN 144:312460 AN 2005:727417 CAPLUS

---

## Erklärung

Ich erkläre, dass ich die Dissertation ***Amphiphilic Diblock Copolymers for Molecular Recognition*** nur mit der darin angegebenen Hilfe verfasst und bei keiner anderen Universität und keiner anderen Fakultät der Universität Basel eingereicht habe.

Basel, den 03.02.2009

Rainer Nehring

---